Methods for Functional Brain Imaging

by

Thomas Witzel

B.S. Computer Science
Northeastern University (2002)

Submitted to the Harvard-MIT Division of Health Sciences and Technology
in partial fulfillment of the requirements for the degree of

DOCTOR OF PHILOSOPHY
IN HEALTH SCIENCES AND TECHNOLOGY

at the

MASSACHUSETTS INSTITUTE OF TECHNOLOGY

SEPTEMBER 2011

ARCHIVES
MASSACHUSETTS INSTITUTE OF TECHNOLOGY
SEP 2 1 2011
LIBRARIES

© Massachusetts Institute of Technology 2011. All rights reserved.

Author ....
Harvard-MIT Division of Health Sciences and Technology
Aug 3, 2011

Certified by ....
Lawrence L. Wald, Ph.D.
Associate Professor of Radiology, Harvard Medical School
Thesis Supervisor

Accepted by ....
Ram Sasisekharan, Ph.D.
Director, Harvard-MIT Division of Health Sciences and Technology
Edward Hood Taplin Professor of Health Sciences and Technology
and Biological Engineering.

Methods for Functional Brain Imaging

by

Thomas Witzel

Submitted to the Harvard-MIT Division of Health Sciences and Technology
on Aug 3, 2011, in partial fulfillment of the
requirements for the degree of
DOCTOR OF PHILOSOPHY
IN HEALTH SCIENCES AND TECHNOLOGY

Abstract

Magnetic resonance imaging (MRI) has demonstrated the potential for non-invasive mapping of structure and function (fMRI) in the human brain. In this thesis, we propose a series of methodological developments towards improved fMRI of auditory processes. First, the inefficiency of standard fMRI that acquires brain volumes one slice at a time is addressed. The proposed single-shot method is capable, for the first time, of imaging the entire brain in a single-acquisition while still maintaining adequate spatial resolution for fMRI. This method dramatically increases the temporal resolution of fMRI (20 fold) and improves sampling efficiency as well as the ability to discriminate against detrimental physiological noise. To accomplish this it exploits highly accelerated parallel imaging techniques and MRI signal detection with a large number of coil elements.

We then address a major problem in the application of fMRI to auditory studies. In standard fMRI, loud acoustic noise is generated by the rapid switching of the gradient magnetic fields required for image encoding, which interferes with auditory stimuli and enforces inefficient and slow sampling strategies. We demonstrate a fMRI method that uses parallel imaging and redesigned gradient waveforms to both minimize and slow down the gradient switching to substantially reduce acoustic noise while still enabling rapid acquisitions for fMRI.

Conventional fMRI is based on a hemodynamic response that is secondary to the underlying neuronal activation. In the final contribution of this thesis, a novel image contrast is introduced that is aimed at the *direct* observation of neuronal magnetic fields associated with functional activation. Early feasibility studies indicate that the imaging is sensitive to oscillating magnetic fields at amplitudes similar to those observed by magnetoencephalography.

Thesis Supervisor: Lawrence L. Wald, Ph.D.
Title: Associate Professor of Radiology, Harvard Medical School

Acknowledgments

I would like to thank the people who have made the path to this thesis possible for me. Most importantly I like to thank my mother for all of her support over all these years. I would also like to thank my thesis advisor Prof. Lawrence L. Wald for giving me the opportunity to do research in his research group. In the years that I spent in the Wald group I was able to participate in a number of research projects and received invaluable training in virtually all aspects of MRI. I furthermore like to express gratitude to my thesis committee members Prof. Elfar Adalsteinsson and Prof. Jennifer R. Melcher for supporting me and helping me to bring my life as graduate student to an end. I would not be on this path without Anders M. Dale who opened the world of neuroimaging to me by bringing me to Boston and my dear friend Fa-Hsuan Lin who helped me in all aspects of my life while I was a graduate student. I admire the patience of my office mate and friend Jonathan R. Polimeni who also helped guide much of my work in the past years. Finally, I also thank my colleagues in the Wald group as well as the entire Martinos center which provided me with access to equipment and incredible resources that can probably not be found in any other place in the world.

Contents

1 Introduction 17

2 Single-Shot Echo Volume Imaging 21

2.1 Introduction 21
  2.1.1 Challenges for single-shot EVI 21
  2.1.2 Parallel Imaging in single-shot EVI 23
2.2 Methods 24
  2.2.1 Acquisition 24
  2.2.2 Image reconstruction 27
  2.2.3 GRAPPA "g-factor" 29
  2.2.4 fMRI 29
  2.2.5 Physiological Noise 30
2.3 Results 31
  2.3.1 Images 31
  2.3.2 GRAPPA "g-factor" 33
  2.3.3 tSNR 35
  2.3.4 fMRI 42
  2.3.5 physiological noise 44
2.4 Discussion 50

3 Quiet Echo Planar Imaging 57

3.1 Introduction 57
3.2 Methods 61

3.2.1 Acoustic Measurements 61
3.2.2 Quiet EPI acquisition 63
3.2.3 Quiet EPI image reconstruction 64
3.3 Results 65
3.3.1 Acoustic Measurements 65
3.3.2 Images obtained with GRAPPA/Fourier transform 66
3.4 Discussion 68

4 Stimulus Induced Rotary Saturation **73**
4.1 Introduction 73
4.2 Methods 78
4.2.1 Bloch Equation simulation 80
4.2.2 Rotary saturation spectra 82
4.2.3 Block design experiment 82
4.3 Results 83
4.3.1 Magnetic field calculation 83
4.3.2 Bloch simulation 83
4.3.3 Rotary saturation spectra 85
4.3.4 Block detection experiment 86
4.4 Discussion 88
4.5 Conclusion 93

5 Summary **99**

List of Figures

2-1 Schematic of the EVI pulse sequence diagram showing the first few partitions. The readout waveform is alternating direction identically to that of conventional EPI. The phase-encoding blips (PE^1) are interleaved between the readout ADC windows. Note the phase-encoding rewinder between the partitions. Blips in the partition-encoding direction (PE^2) advance k-space in k_z direction analogously to the phase-encoding blips along k_y. 24

2-2 Diagram of k-space traversal in the single-shot EVI sequence. Here an example trajectory for $\mathrm{R} = 3 \times 4$ is shown, with the the phase-encoding direction undersampled by a factor of 4 and the partition encoding direction undersampled by a factor of 3. Furthermore the asterisk denotes the area of k-space omitted from sampling due to the partial Fourier acquisition. Also note the rewinders that rewind k_y during the travel to the next k_z. 25

2-3 Reconstruction of 16-shot auto-calibration scan in original slab orientation. 32

2-4 Reconstruction of 16-shot auto-calibration acquisition shown axially. Only the superior 32 slices are shown. 33

2-5 GRAPPA reconstruction of fully relaxed single-shot scan shown axially. Average of 10 time points. Only the superior 32 slices are shown. . . 34

2-6 GRAPPA reconstruction of TR=120 ms single-shot scan shown axially. Average of 10 time points. Only the superior 32 slices are shown. . . 35

2-7 GRAPPA g-factors simulated based on a phantom scan using a sagittal slab analogously to the human protocol. Slices shown axially with superior slice on the top-left. 36

2-8 GRAPPA g-factors simulated based on a phantom scan using an axial slab. 37

2-9 GRAPPA g-factors simulated based on a human scan using a sagittal slab. 12 selected slices shown axially with superior slice on the top-left. 38

2-10 Plot of the SNR relative to a fully relaxed 90 degree excitation, for steady-state signal at given TR and Ernst angle (black curve) and averages of the steady state signal at TR=120 ms and 21 degrees flip (red stars). White noise is assumed for the averaged short-TR acquisition. It can be seen, that starting with a TR of 1500 ms the averages of the TR=120 ms acquisitions have better thermal SNR than an acquisition performed at a TR of 1500 ms. The presence of temporal autocorrelation in human data will prevent this from being a realistic scenario. . 39

2-11 Temporal SNR of the single shot EVI acquisition of the agarose phantom. Axial cuts, 12 slices out of 64 shown in superior to inferior order. 41

2-12 Temporal SNR of the 16-shot EVI acquisition of the agarose phantom. Axial cuts, 12 slices out of 64 shown in superior to inferior order. . . 41

2-13 Plot of average auto-correlation functions for the groups of voxel, which have poor tSNR gain (gain < 2) in temporal averaging over 16 timepoints (shown in blue), and those that have high tSNR gain (gain > 3), close to the ideal $\sqrt{N}$, shown in red. 42

2-14 Plot of the noise spectra for the group of voxels with poor tSNR again, the voxels with high SNR gain and the agarose phantom. The human data shows distinct spectral peaks for respiration at 0.3 Hz, cardiac at 0.8 Hz as well as higher harmonics of the cardiac. A distinctive peak visible at 0.02 Hz appears to be due to a global signal, which can be removed. While the high-SNR gain voxels still feature cardio-respiratory noise components, the noise spectrum is flatter than than in the other group and thus explains the higher tSNR gains after averaging time points. The prominent peaks in the phantom data seem to stem mainly from voxels on the phantom border and are likely artifactual. 43

2-15 Temporal SNR of the 16-shot EVI acquisition of human brain. Axial cuts, 12 slices out of 64 shown in superior to inferior order. 44

2-16 Temporal SNR of the single shot EVI acquisition of human brain. Axial cuts, 12 slices out of 64 shown in superior to inferior order. 45

2-17 Ratio of temporal SNRs between the single-shot EVI acquisition and the 16-shot EVI acquisition of human brain. Axial cuts, 12 slices out of 64 shown in superior to inferior order. The single-shot data appears to have higher tSNR in the cortical areas, and less tSNR than the multi-shot acquisition in the center and inferior areas of the brain, where the g-factor losses dominate. 46

2-18 Ratio of tSNR between the series of averages of 16 time-points and the individual volume time series. Axial cuts, 12 slices out of 64 shown in superior to inferior order. It appears that there is high SNR gain by temporal averaging in the central areas that have high g-factors as well as some white matter structures, while there is very little tSNR gain in the cortical areas. If the noise were temporally white, a tSNR gain of 4 would be expected. 47

2-19 Temporal SNR of the single shot EVI acquisition of human brain, low-pass filtered at 0.5 Hz. Axial cuts, 12 slices out of 64 shown in superior to inferior order. 48

2-20 Result of the basic GLM analysis of the visual hemifield task. All 8 runs were combined using a simple fixed-effects model. Overlay thresholded at a t-score of 10. The activity nicely localizes to the contra-lateral hemisphere of the stimulated visual hemifield as would be anticipated. 48

2-21 Power spectrum for the voxels that were activated in either condition during the fMRI task. Furthermore the power spectrum is plotted for the same voxels, but using time-series data from the rest runs. In both the stimulated runs, as well as the rest runs peaks can be seen for the cardiac frequency (1.3 Hz) and its harmonic, as well as the respiration frequency (0.3 Hz). By power, the respiration has the biggest influence on the signal, although its about an order of magnitude below the activated voxel signal. There is significant fluctuation in the low-frequency band, even during the rest run. 49

2-22 Spatial map of the power at the cardiac frequency of 1.3 Hz. The map has been thresholded at a level of 3dB above the DC-power of each voxel. The map shows clearly highly localized distribution at this frequency, which appear to be co-located to major arteries. 50

2-23 Spatial map of the power at the respiratory frequency of 0.3 Hz. The map has been thresholded at a level of 3dB above the DC-power of each voxel. The map shows most of the power to be at the tissue-CSF interface, dominantly along the partition-encoding direction. 50

2-24 Spatial map of the coefficient of regression for the pulse-oxymeter regressor in the GLM. Again, similary to the cardiac frequency map, highly correlated voxels appear to be highly localized and appear to be co-located with major arteries. 51

3-1 Schematic of k-space trajectories resulting from constant phase-encoding EPI. On the left, unaccelerated EPI forms a zig-zag trajectory, where only the samples at $k_x = 0$ are sampled uniformly along k_y, and the trajectory is undersampled at the extreme values of k_x. On the right, a 4-fold accelerated trajectory is shown with the solid line showing the acquired data and the stippled line showing the GRAPPA reconstructed data. The trajectory is uniformly sampled along k_y at $k_x = 0$, and undersampled not only at the corners, but also at the trajectory intersection points. 62

3-2 Schematic of the quiet EPI sequence. The general layout follows a regular EPI sequence, but the readout gradient waveform is sinusoidal and the phase encoding is constant, as opposed to blipped. The slice select gradient is rounded as well. Note, that the gap between the three phase-correction lines and the image lines in the readout is filled with another half-cycle to improve continuity. 63

3-3 Plot of the acoustic noise level measurements taken with the standard MGH EPI sequence (black diamonds), the quiet EPI sequence (red pentagrams) and the quiet EPI sequence without the fat suppression pulses (green circles). The acoustic echo-spacing is the half-period of the fundamental frequency of the readout waveform. If acceleration is used, the effective echo-spacing will be the acoustic echo-spacing divided by the acceleration factor R. The pink band between 0.6 and 0.7 ms echo-spacing denotes a forbidden range of echo-spacings due to an acoustic resonance mode of the gradient coil in that range. Also note the increase in noise level towards the band from both sides. . . 65

3-4 Images acquired with an acceleration factor of R=2 and reconstructed with GRAPPA and Fourier transform. The Fourier reconstruction causes aliasing artifacts due to the zig-zag trajectory. 66

3-5 Images acquired with an acceleration factor of R=4 and reconstructed with GRAPPA and Fourier transform. This simplified reconstructed causes blurring noticable in the images, as well as aliasing type artifacts in denoted by the red arrows in the images. 67

4-1 Circuit diagram of the apparatus for applying oscillating currents to the dipole phantom during the spin-locking. The function generator is gated by a logic pulse generated by the pulse sequence so that its output is non-zero only during TSL. The output of the function generator then goes through an isolation transformer to eliminate DC and common-mode currents and drives the dipole phantom through a series resistor (10 kΩ) and series RF chokes to block RF pickup on the lines. The current in the phantom is measured by monitoring the voltage drop across the 10 kΩ series resistor using an optically isolated operational amplifier with a gain of 10 and 500 kΩ input impedance. The RMS amplitude of the output of the operational amplifier is measured with a digital oscilloscope. 79

4-2 Pulse sequence diagram for the spin-lock prepared EPI sequence. After an initial 90 ° excitation, the magnetization is spin-locked along the y-axis by a continuous wave RF pulse applied for a time TSL. Immediately following the spin-lock period, TSL, the magnetization is rotated back to the z-axis by the 90°_{-x} pulse. The the traditional EPI sequence images the magnetization which experienced the spin-lock state. $T_{1\rho}$ relaxation processes during TSL are therefore expected to diminish the signal intensity in the EPI image. The sinusoidal current input to the phantom is applied during the spin-lock period and is shown schematically in the bottom trace. 81

4-3 Representative spin-lock prepared images from the sequence of Fig. (A) phantom image spin-locked with γB_{1lock} =40 Hz shown with the location of the current dipole overlaid in yellow. (B) Time-series standard deviation of a time-series of 420 of the spin-lock prepared images. (C) Brain image obtained with the spin-lock prepared sequence with γB_{1lock} =40 Hz and (D) γB_{1lock} =10 Hz. 84

4-4 Magnitude if the z-component if the magnetic field associated with the current dipole phantom. Left, axial image of the z-component of the field for a $5.6\,\mu A$ current in the dipole (56 nAm dipole moment) based on the distributed dipole model. A field of 1 nT is estimated for a distance of 1.5 mm from the wire. Right, plot along the y-axis showing both the field values derived from the distributed dipole model and the Biot-Savart law for a long thin wire. 85

4-5 Simulation of the rotary saturation effect based on the Bloch equations in the rotating frame. The simulations show the fraction of the spin-locked magnetization as a function of the frequency applied $B_{rotarysat}$ field. When the frequency of $B_{rotarysat}$ reaches the resonance condition in the rotating frame (equal to γB_{1lock}) the spin-locked magnetization is rotated away from the spin-lock field B_{1lock}. In the spin-lock prepared experiment, only the spin-locked magnetization is returned to the longtudinal axis for subsequent imaging. Simulations were performed for human gray matter at 1.5 T (T_1 = 1100 ms, T_2 = 950 ms, T_2^* = 100 ms). The effect is shown for rotary saturation at $\omega_{rotarysat}$ of 10 Hz,20 Hz and 40 Hz (black, blue and red curves respectively) using $B_{rotarysat}$ of 1 nT (solid line) and 5 nT (dashed line). 86

4-6 Simulation of the rotary saturation effect based on the Bloch equations in the rotating frame. The simulations show the fraction of the spin-locked magnetization as a function of the frequency applied $\mathrm{B_{rotarysat}}$ field. When the frequency of $\mathrm{B_{rotarysat}}$ reaches the resonance condition in the rotating frame (equal to $\gamma \mathrm{B_{1lock}}$) the spin-locked magnetization is rotated away from the spin-lock field $\mathrm{B_{1lock}}$. In the spin-lock prepared experiment, only the spin-locked magnetization is returned to the longtudinal axis for subsequent imaging. Simulations were performed for human gray matter at 1.5 T ($\mathrm{T_1} = 1100\,\mathrm{ms}$, $\mathrm{T_2} = 950\,\mathrm{ms}$, $\mathrm{T_2^*} = 100\,\mathrm{ms}$). The effect is shown for rotary saturation at $\omega_{\mathrm{rotarysat}}$ of 10 Hz,20 Hz and 40 Hz (black, blue and red curves respectively) using $\mathrm{B_{rotarysat}}$ of 1 nT (solid line) and 5 nT (dashed line). 87

4-7 Two-sided t-test results (not Bonferroni corrected) from the block-design paradigm shown with a lower threshold of $p < 10^{-3}$ and a color scale saturation level of $p < 10^{-8}$. All block designs were 20 s per period, and $\gamma \mathrm{B_{1lock}} = 40\,\mathrm{Hz}$. T-test results are overlaid on a high-resolution Turbo Spin Echo (TSE,RARE) image which allows visualization of the current dipole's wires. A) $118\,\mu A$ applied current, B) $11.5\,\mu A$ applied current C) $5.6\,\mu A$ applied current. 88

Chapter 1

Introduction

Functional Magnetic Resonance Imaging (fMRI) has become a widely applied method to non-invasively study how the human brain functions. Commonly the Blood Oxygen Level Dependent (BOLD) contrast is used, which produces image intensity changes that track the concentration of deoxyhemoglobin molecules present in vascular structures inside of a voxel. It is known that the metabolism involved in neuronal activity causes a local vascular response, that can then be detected with fMRI, which in turn enables the localization of increased neuronal activity in the brain. While this technique is being used successfully and routinely, there are limitations to fMRI that affect its usability in certain neuroscience applications. In this thesis, I address three of these limitations and demonstrate work towards improving the applicability of fMRI in areas where it could not be used before. Specifically I adress the contamination of the BOLD response with respiratory and cardiac noise due to the slow sampling rate commonly used in fMRI, the acoustic noise generated by fMRI data acquisition, and demonstrate work toward directly detecting electrical neuronal activity with MRI is shown, removing the interpretational confounds that neuro-vascular coupling imposes on fMRI.

Most fMRI acquisitions are performed using single-shot echo-planar imaging (EPI), which allows the very rapid acquisition of an entire 2D image following a single excitation. Since whole-brain coverage is often desired, the temporal resolution of EPI acquisition is however still limited, and repetition times are often 2 s or longer, depending on the voxel size. The BOLD signal is vulnerable to contamination by physiological noise such as respiratory signals and cardiac pulsation. Both of these phenomena are not Nyquist-sampled at repetition rates of 2 s or slower, and are therefore difficult to removed from the acquired data. In chapter 2 this issue is addressed by implementing, for the first time, a single-shot echo-volume imaging (EVI) method that provides whole-head coverage and spatial resolution close to that often used in EPI. This is accomplished using highly accelerated parallel imaging. Since EVI acquires entire volumes following a single excitation, it allows temporal resolutions that are an order of magnitude higher than those used in EPI. When EVI data are aquired with repetition times of 0.2 s or less, both respiratory effects and cardiac pulsation effects are Nyquist-sampled and can be identified and removed if needed, which allows the study of the influence of these physiological noise sources on the BOLD signal, as well as the study of brain activations without confounds from these physiological noise sources.

The rapid gradient switching involved in EPI causes a significant amount of acoustic noise, sometimes exceeding 100 dB SPL. While this can be managed from a safety perspective using ear protection such as ear plugs, it however imposes severe limitations on the research that requires quiet environments, for example research of the auditory system and research of sleep. In addition it adds to discomfort and anxiety of patient populations already uncomfortable with MRI, such as elderly and pediatric patients. In chapter 3 an implementation of an acoustically quiet EPI pulse sequence is demonstrated, which is not only substantially quieter, but maintains the performance needed to acquire images with the same speed and quality the standard EPI method does. This is accomplished by using a parallel imaging technique that could be used to either speed up EPI or increase its spatial resolution, but here it is instead used to maintain temporal and spatial resolution of the data while reducing the number of gradient pulses and their switching speed.

A limitation of the use of the BOLD contrast is that the mechanisms which couple the vascular response to the underlying neuronal activity are not yet well understood. It is known that the neuro-vascular coupling is in part mediated by astrocytes and interneurons, but the details are yet to be discovered. It has also been shown in simultaneous electrophysiological and BOLD recordings that the relationship between the neuronal responses and the BOLD response is non-linear. This limits the use of BOLD fMRI in neuroscience applications where a more direct measurement of the neuronal activity would be required. A new contrast mechanism is demonstrated, that sensitizes MRI to oscillating magnetic fields in the magnitude and frequency range that is observed for neuromagnetic responses in human brain. Since these neuromagnetic fields are generated by the post-synaptic currents in the dendrites of large pyramidal cells that are present in the cortex, these would reflect a more direct measurement of neuronal activity compared to BOLD fMRI. The same neuromagnetic fields can also be observed by magnetoencephalography (MEG), however the detection of these fields outside the head with the MEG device severely limits the ability to spatially localize their origin. The Stimulus Induced Rotary Saturation (SIRS) method proposed in this thesis does not have a localization problem and in theory may be able to localize the generators of neuromagnetic fields on a millimeter scale.

Chapter 2

Single-Shot Echo Volume Imaging

2.1 Introduction

Echo Volume Imaging (EVI) was conceived by Peter Mansfield as a method for three-dimensional "snapshot" imaging, building on his previous two-dimensional Echo Planar Imaging (EPI) technique, in fact both methods were suggested initially in the same article by Mansfield [2], but the 2D variant was developed practically first. The rationale behind the single-shot three-dimensional technique was that objects moving in three dimensions ought to be captured with a single-shot three-dimensional imaging sequence, in order to avoid each slice capturing a different position of the object. Analogously to EPI, where an entire 2D k-space is sampled following a single excitation, in EVI an entire 3D k-space is sampled following a single excitation. In this thesis the application of EVI is to capture three-dimensional images of the brain with T2* contrast with a very high sampling rate, while at the same time maintaining acceptable spatial resolution for the use in fMRI.

2.1.1 Challenges for single-shot EVI

In single-shot EVI the entire k-space of a 3D volume has to be acquired following a single excitation. Since the signal T2* decays during the readout, the entire acquisition of the volume has to be accomplished in a time on the order of T2*. At 3 T this means the readout train should not exceed 50 ms substantially, when blurring is to be avoided. Using a body gradient coil and at a typical spatial resolution of 3 mm, the echo-spacing, which is also the time it takes to acquire a single k-space line, cannot be shorter than 0.46 ms[1], due to the electrical stimulation of the subjects peripheral nerves at faster switching rates. Using a head-only gradient coil, which does not induce that large electric fields in the subjects trunk, the echo-spacing can be lowered to about 0.26 ms[2].

These constraints on the minimum echo spacing translate into serious limitations on the number of k-space lines that can be encoded for a 3D volume, so that all early work was either acquired in multiple shots and or at low spatial resolution. The first human EVI images were presented by Mansfield et.al. [4] and Song et.al. [10] in 1994, where the Mansfield approach was two-shot $16 \times 16 \times 16$ and the Song method was $32 \times 32 \times 7$ matrix size on the human brain. The Song et.al. method was single-shot but had a readout duration of 128 ms, causing substantial blurring as result. Only a year later, Mansfield delivered a single-shot EVI method for the human brain [3] that made use of a custom built head-gradient set. With a single-shot matrix size of $64 \times 64 \times 8$ and a nominal spatial resolution of $3.0 \times 3.0 \times 2.5\,\mathrm{mm}^3$ it remains the best acquisition by gradient performance alone to this day.

To overcome the low spatial resolution imposed by the limited readout duration, EVI was used in combination with localized acquisition of only a part of the brain, where the combination of the small matrix size and the small field of view lead to an acceptable spatial resolution. Notable examples are the single-shot EVI by Yang et.al.[14], where a box covering a third of the width of the brain was acquired in a single shot, and the work by van der Zwaag et.al.[13], where one hemisphere of the brain was acquired in two shots.

A second challenge arising from finite gradient switching speed is that an EVI trajectory has echo-spacing in two directions, the phase-encoding direction and the partition-encoding direction. Since the image distortion in the phase-encoding directions is proportional to the echo-spacing in those directions, the echo-spacings have to be kept short. In a trajectory, such as the one shown in figure 2-2, the echo-spacing in the phase-encoding direction can be kept short just like in an EPI sequence, the echo-spacing in the partition-encoding direction will however be substantially longer (the number of acquired phase-encoding lines times the echo-spacing in the phase encoding direction plus the time required for rewinding the phase-encoding direction), leading to much larger image distortion in the partition-encoding direction in locations where susceptibility gradients are present.

---

[1] This is the limit imposed by the SAFE model on a Siemens TIM Trio with the AS92 gradients and TQ-engine amplifiers. It can be assumed that these are not much different for other makes and models with comparable gradients.

[2] This is the limit imposed by the SAFE model on a Siemens TIM Trio with the AC88 head-gradient insert and TQ-engine amplifiers. It is also consistent with the echo-spacing reported by Mansfield et.al. in 1995 using home-built head gradients[3].

2.1.2 Parallel Imaging in single-shot EVI

Parallel imaging techniques allow for the replacement of gradient encoding with coil encoding, leading to the so called accelerated imaging, where the number of acquired k-space lines is reduced by the acceleration factor R. It is obvious that accelerated imaging lends itself to application in EVI in order to increase the volume that can be encoded in T2* time. For low R the improvement is not substantial enough to reach reasonable spatial resolution for the whole brain in a single-shot, however it can be combined with localized acquisition as shown by Rabrait et.al.[7]. Rabrait employed $R = 2 \times 2$ acceleration and SENSE[6] reconstruction on a small VOI covering part of the prefrontal lobe of the brain surrouding Broca's area, which enabled the authors to perform a high temporal resolution (TR=200 ms) fMRI experiment on language processing.

We propose the use of parallel imaging to reduce the total readout duration substantially, by using acceleration factors as high as required to acquire a whole brain at acceptable spatial resolution in a single-shot. Head receive array-coils with 32 channels are now commercially available and can be used for high acceleration in 2 directions of up to $R = 4 \times 4$. Common applications of the 32-channel array usually use acceleration factors of $R = 2$, and in EPI acceleration factors of $R = 3$ are sometimes used. Higher acceleration factors are usually avoided in order to not encounter artifacts and significant SNR losses stemming from the image reconstruction techniques associated with the reconstruction of accelerated data. We will push the acceleration factor to the limit and will provide some characterization of the consequences of doing so.

Using a very high acceleration factor of 16, we are going to demonstrate the acquisition of a $64 \times 64 \times 56$ volume in a single-shot with a total readout time of 82 ms, which brings the readout time of EVI within a factor of 2 of the desired readout time for non-blurry images. In addition we characterize the SNR characteristics of data acquired in human and phantoms and provide an initial demonstration of fMRI using this method.

2.2 Methods

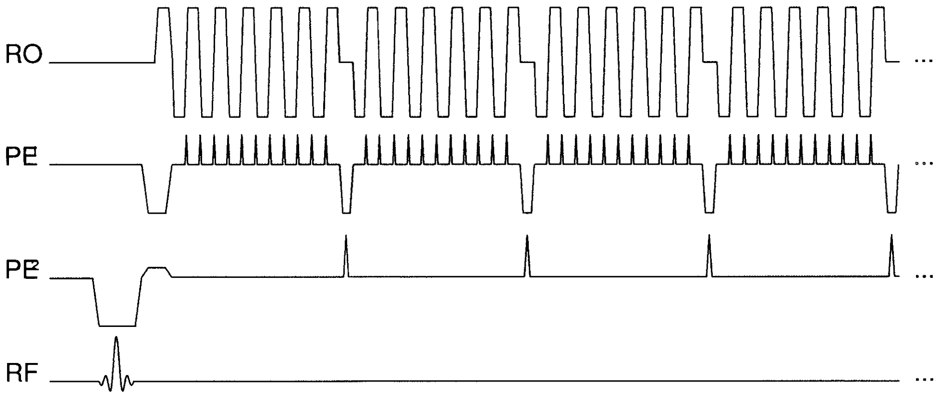

Figure 2-1: Schematic of the EVI pulse sequence diagram showing the first few partitions. The readout waveform is alternating direction identically to that of conventional EPI. The phase-encoding blips (PE^1) are interleaved between the readout ADC windows. Note the phase-encoding rewinder between the partitions. Blips in the partition-encoding direction (PE^2) advance k-space in k_z direction analogously to the phase-encoding blips along k_y.

2.2.1 Acquisition

All data were collected using a Siemens TIM Trio (3 T) scanner using the Siemens 32 channel head coil. The scanner was equipped with the Siemens AS92 gradients, with 40 mT/m maximum gradient strength and 175 mT/m/ms maximum slew rate.

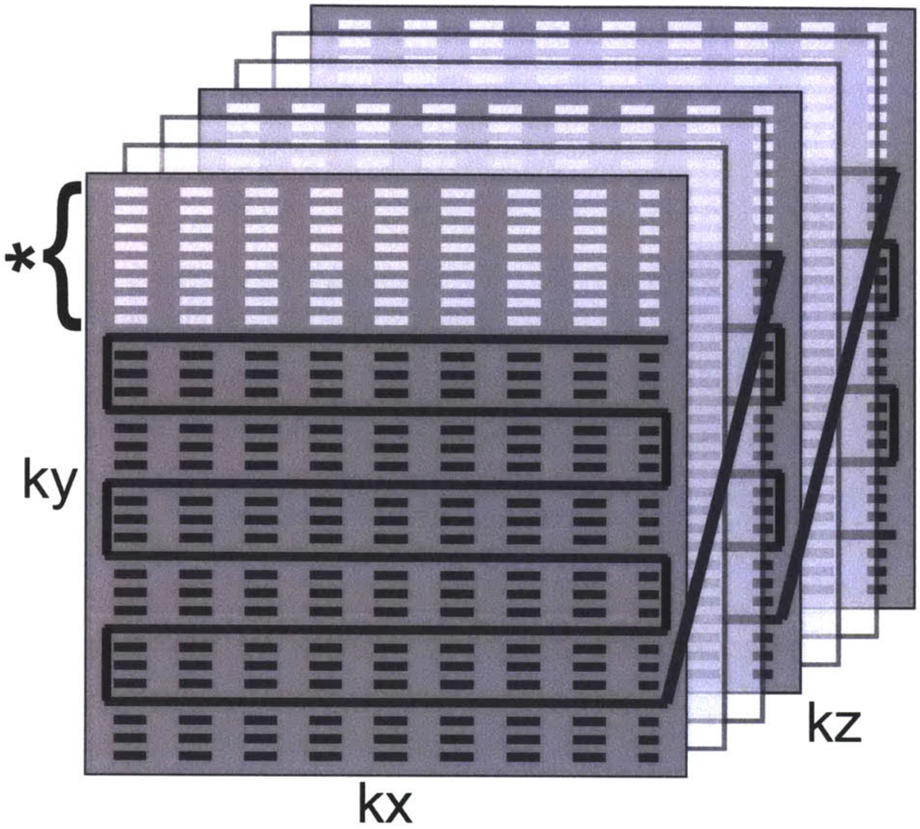

Figure 2-2: Diagram of k-space traversal in the single-shot EVI sequence. Here an example trajectory for R = 3 × 4 is shown, with the the phase-encoding direction undersampled by a factor of 4 and the partition encoding direction undersampled by a factor of 3. Furthermore the asterisk denotes the area of k-space omitted from sampling due to the partial Fourier acquisition. Also note the rewinders that rewind k_y during the travel to the next k_z.

For human subject scans the matrix size was set to $64 \times 64 \times 56$ with a nominal spatial resolution of $3.4 \times 3.4 \times 3.0\,\mathrm{mm}^3$. Phantom scans were performed with a nominal spatial resolution of $3.4 \times 3.4 \times 3.4\,\mathrm{mm}^3$, in order to accomodate the spherical agarose phantom in the FOV. All other sequence parameters were identical for both human and phantom scans.

The sequence used is depicted in a small sketch shown in figure 2-1 and is based on the sequence used by van der Zwaag et.al.[13]. An important feature is the phase-encoding rewinders used during each partition-encoding blip, which allow the k-space trajectory seen in figure2-2 to traverse the phase-encoding direction in only one direction sense, rather than reversing phase-encoding direction in every other partition.

This is done to avoid N/2 ghosting from phase encoding gradient imperfections, which would be very difficult to correct. The readout gradient waveform is designed to always use the maximum possible slew rate on the ramps. The flat-top of the readout waveform is restricted to have an duration of at least 15% of the total duration of one lobe, and is maximized for each protocol.

The TE was 41 ms and the TR was 120 ms and the flip-angle was set to the Ernst-angle of 21 degrees, assuming a T1 value for brain gray matter at 3T of T1=1470 ms. Strong gradient spoiling in readout- and slab-direction was used. Due to the poor tissue contrast at TR=120 ms, a small time series of 10 volumes with TR=5000 ms and a flip-angle of 90 degrees was collected to generate a reference volume with some tissue contrast, which could also aid coregistration to an anatomical scan of the subject.

Since EVI is very sensitive to off-resonances, all subjects are shimmed using multiple iterations of 3D-fieldmap-based 1st and 2nd order shimming. Empirically, the automatic shim software provided with the scanner does not provide good enough shims to yield good image results, so the shim is repeated manually until the fieldmap shows minimal wrapping. Second order shims are recommended for single-shot EVI as decribed here to work at 3 T at the same level of distortion.

The slab was oriented sagittally with the readout direction along the head-foot direction, the phase-encoding direction along the anterior-posterior direction and the partition-encoding direction along the right-left direction. The trajectory was undersampled 4-fold in both phase-encoding directions, leading to a 16-fold undersampling to be reconstructed by GRAPPA[1]. Furthermore 6/8 partial Fourier encoding was used in the primary phase-encoding direction to further reduce the echo-spacing in the partition-encoding direction.

Four fully-sampled auto-calibration volumes were acquired in an interleaved fashion using 16-shots each. The acquisition of multiple auto-calibration volumes serves two purposes. Firstly, it allows the rejection of a volume in case the subject moves between shots and secondly, the quality of the GRAPPA kernel can be improved by training it on more samples, which is what multiple volumes provide.

Combining the 16-fold acceleration and the partial-Fourier acquisition, means that only 168 k-space lines of the 3584 k-space lines to be reconstructed are acquired, which corresponds to an effective undersampling factor of 21!

The echo-spacings are 0.46 ms in the primary phase-encoding direction and 5.86 ms in the partition-encoding direction, leading to effective echo-spacings of 0.12 ms in the primary phase-encoding direction and 1.47 ms in the partition-encoding direction, given the acceleration and partial Fourier scheme as described above. The echo-spacing in the partition-encoding direction includes 0.34 ms for the rewinder gradient in the phase-encoding direction. The total readout duration is therefore 81.7 ms. The relatively long effective echo-spacing in the partition-encoding direction can lead to image distortion that is sometimes more than twice that observed in "conventional" EPI along the phase-encoding direction in areas with strong susceptibility gradients.

At the beginning of each measurement, 1000 k-space lines of noise are acquired, which were used to calculate channel noise covariances, which can be used by the image reconstruction for optimum SNR image reconstruction[9].

Simultaneously to the image acquisition, the subject's pulse was measured using a pulse oxymeter at the subjects left-hand index finger. Furthermore the subjects respiration was measured using a pneumatic belt. Both devices are the standard Siemens equipment delivered with the scanner. To aid the synchronization between the data recorded by the Siemens physiological monitoring unit (PMU) and the image data we also recorded the output of the OSC0 channel of the scanner on the EXT channel of the PMU. Since the PMU has a sampling rate of only 50 Hz, the OSC0 signal was stretched from 100 μs to 2 ms using a pulse stretcher. All human subject data were acquired under an MGH and MIT IRB approved protocol.

2.2.2 Image reconstruction

All images were reconstructed using custom software implemented in C++ specifically for this thesis project. The image data was reconstructed using the GRAPPA algorithm [1] using a $3 \times 3 \times 3$ 2D-GRAPPA kernel. The GRAPPA kernel was fit using four concatenated fully-sampled ACS volumes to improve robustness of the fit by virtue of adding more training data. The solution to the least-squares fitting problem was obtained by using the QR decomposition of the normal form of the problem rather than the SVD of the full problem in order to improve the computational performance. Despite the data being in single-precision, all GRAPPA related operations were performed in double precision, which reduces imperfections in the GRAPPA kernel that would be needlessly encountered due to numerical precision errors. While the software developed for this project has a variety of regularization options to further improve the GRAPPA kernel fit and allow the fit of larger kernels without numerical failure of the fitting problem, none of these were used for the data shown in this thesis, in order to reduce complexity of this document, as the outcome in terms of SNR of a GRAPPA reconstruction can strongly depend on both regularization parameters and kernel size in a non-intuitive way. Furthermore, over-regularization of the GRAPPA kernel fit will lead to changes in image properties such as the point-spread function of the voxels, an aspect of GRAPPA that has yet to be researched.

After the GRAPPA reconstruction of each channel, the partial-Fourier gap was zero-filled prior to the Fourier transform. Furthermore all volumes were apodized with a Tukey window along the phase-encoding and partition-encoding directions, in order to reduce Gibbs ringing, which results from the low number of k-space samples in the phase- and partition-encoding directions (truncation artifacts) as well as highly asymmetric echoes stemming from voxels with tissue susceptibility gradients in the same direction as the respective phase-encoding blip gradient polarity (i.e. the echo "walking" towards the phase-encoding due to susceptibility), leading to stronger truncation artifacts. For the data shown here the individual channel images were always combined using the sum-of-squares.

All images were then stored as single-precision float values in NIFTI file format for further analysis and processing. Correct scanner- and patient coordinate information was generated from the raw scanner data and incorporated in the NIFTI files to allow initial positioning and orientation of the EVI volumes relative to acquired structural images of the subject.

2.2.3 GRAPPA "g-factor"

The calculation of a quantitative measure of the noise amplification introduced by GRAPPA is important, especially since for high acceleration factors such as those used in this study the GRAPPA noise-amplification will be significant. Since for EVI there is no unaccelerated matched case to compare to, a Monte-Carlo simulation technique [8] has to be utilized to obtain the map. A "gold-standard" k-space is generated by averaging the first 20 TR from the GRAPPA reconstruction of the time series. Subsequently a time-series of 512 time-points of noise is synthesized, where the noise has the same channel-correlation as the actually acquired data[3]. The noise is added to the "gold-standard" and this sum is Fourier-transformed and zero-filled to form the synthetic unaccelerated data. In addition the "gold-standard" is under-sampled with the same pattern as the originally acquired data, added with the synthetic noise, and then passed through the GRAPPA reconstruction, Fourier-transform and zero-filling. The resulting image series is the synthetic accelerated data. The tSNR of both the synthetic unaccelerated data as well as the synthetic accelerated data is evaluated and their ratio calculated, from which it is straight-forward to measure the noise-amplification as function of space. For noisy data, in order to avoid the magnitude bias, it maybe necessary to scale down the added noise. In case of the present data, the noise amplitude was reduced by a factor of 100 to avoid magnitude bias[4].

2.2.4 fMRI

The intended application for the single-shot EVI method is functional MRI using the BOLD contrast. In order to test this method a small functional MRI study was performed. As part of this study, either the left or right visual hemifield was stimulated with flickering scaled noise. To ensure that only one visual hemifield was stimulated at a time, the subject was given a fixation task, where a small red dot presented in the center of the screen would change intensity slightly at random times and the subject was asked to press a button every single time the intensity of the dot changed. The dot intensity changes occured with a frequency of about once every 2 seconds. Furthmore, the task was adjusted in difficulty such that the subject would have about 80 % performance. Each run was about 2 minutes long (950 TR), starting with 10 seconds of rest, followed by 16 seconds of flickering noise in one of the hemifields, followed by 10 seconds of rest, repeated 4 times. The order in which left- or right visual hemifield were stimulated was selected randomly. 8 runs were acquired, for a total of 16 minutes of fMRI data. In addition 4 runs of 2 minute (950 TR) rest were also acquired with no stimulus or fixation task.

---

[3] This is achieved by pre-colouring simulated white noise with the noise covariance estimated from the noise data collected with each acquisition.

[4] Since the scaling of the noise in the implementation of the image reconstruction software used at the time was not normalized, the reduction factor of 100 used here is not relative to the actual SNR of the EVI data, but rather set empirically.

Before fMRI analysis the data of all runs was motion corrected using 3dvolreg of the AFNI package, and coregistered to the first fully relaxed (TR=5 s) volume acquired in the experiment. The motion-corrected data was then processed by the application of a general linear model (GLM) in MATLAB. The design matrix contained the experimental design convolved with a canonical hemodynamic response function generated from the SPM analysis package (sum of two gamma functions) using the default parameters[5].To allow for some temporal shift in the response, the first derivates of the HRF models were included in the subsequent columns. Furthermore columns modelling the DC-offset and linear trend were included in the design matrix as well as 6 regressors generated from the motion parameters that were output by the motion correction. The results of this GLM for each of the 8 runs were then combined using a fixed-effects model to generate a final activation map.

2.2.5 Physiological Noise

The physiological data acquired from the subject during the recording was analyzed in two ways. At first the physiological recordings were analyzed in respect to their spectral properties by calculating the power spectral density using the Welch method. Both the recording from the pulse oxymeter as well as the respiratory belt were analyzed separately. After visual inspection the frequencies of prominent peaks in the spectra were determined. In order to see what the influence of these physiological fluctuations on the recorded data was, power spectra were also calculated for the time course of each voxel in the EVI data. Maps corresponding to the frequencies that produced peaks in the spectra of the physiological recordings were generated from the EVI spectra and displayed for inspection.

---

[5] delay of response = 6 s, delay of undershoot = 16 s, dispersion of response = 1 s, dispersion of undershoot = 1 s, ratio of response to undershoot = 6, onset = 0 s, length of kernel = 32 s.

Furthermore it was attempted to use the pulse-oxymetry data directly in the fMRI analysis of the EVI data. For this purpose the pulse-oxymeter data weretemporally lined up with the EVI time series using the triggers in the EXT channel, and then resampled to the sampling rate of the EVI data. Since there is obviously a time-difference between the pulse oxymeter signal at the subjects finger and the pulse in the brain, that lag had to be determined. For each voxel in the EVI time-series, the cross-correlation between the resampled pulse-oxymeter signal and the voxel time-course was calculated and the lag corresponding to the maximum lag was selected. The pulse-oxymeter signal, shifted by this lag was then included in the GLM design matrix for the particular voxel. Since each voxel's optimum lag was calculated independently, each voxel then had its own design matrix for the GLM. After the application of the GLM, the coefficient of the regression corresponding to the pulse-oxymeter regressor was plotted as a 3D map.

2.3 Results

In the following preliminary results obtained in phantoms and 3 different subjects will be shown.

2.3.1 Images

In order to show some of the properties of the EVI images acquired in this study, example images are shown. In figure 2-3 the reconstruction of the 16-shot auto-calibration scan from the reference volume (TR=5 s) is shown in the original sagittal orientation that it is acquired in. A reformated version of the same volume to axial slices can be seen in figure 2-4. While the auto-calibration scan does not feature any GRAPPA related artifacts, it still has the same signal drop-outs and distortion as the accelerated images. The average of all 10 GRAPPA reconstructed volumes of the accelerated reference series (TR=5 s) can be seen in figure 2-5. The average was performed to offset the noise amplification imposed by GRAPPA. Finally the average of the first 10 GRAPPA reconstructed volumes of a resting fMRI acquisition (TR=120 ms) is shown in figure 2-6.

Due to the long echo-spacing in the partition-encoding direction, the images show pronounced distortion in the left right direction, which are particular severe in the vicinity of the paranasal sinuses and the middle ear. There is also areas with complete signal dropout, in especially in the orbito-frontal lobe, inferior-temporal lobe, the temporal poles as well as large parts of the cerebellum.

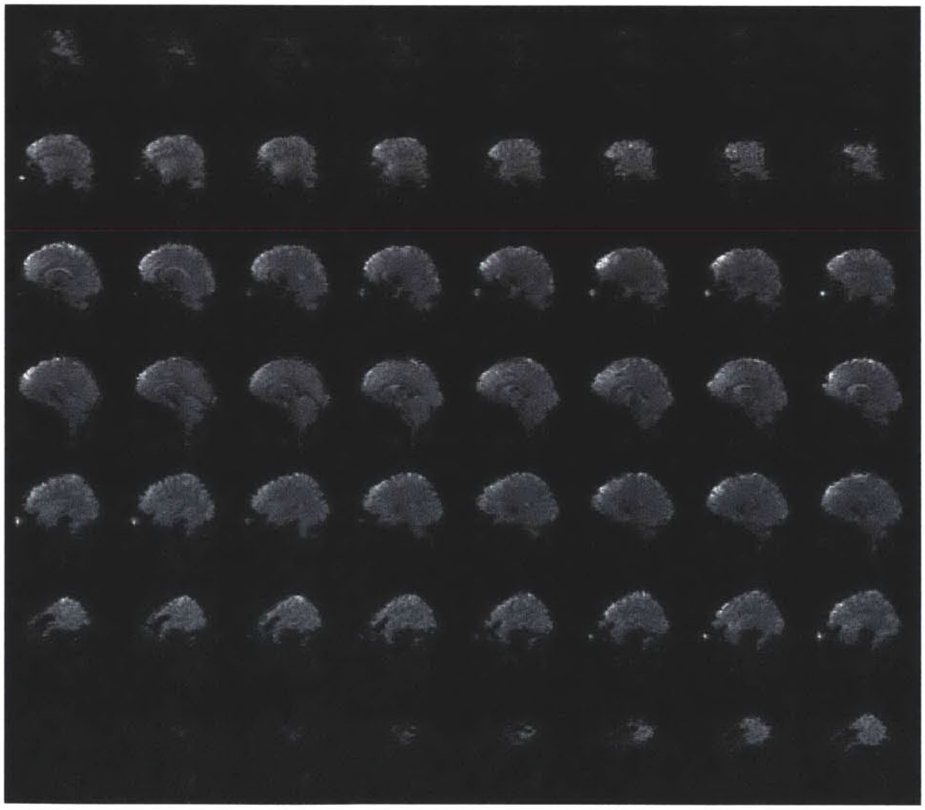

Figure 2-3: Reconstruction of 16-shot auto-calibration scan in original slab orientation.

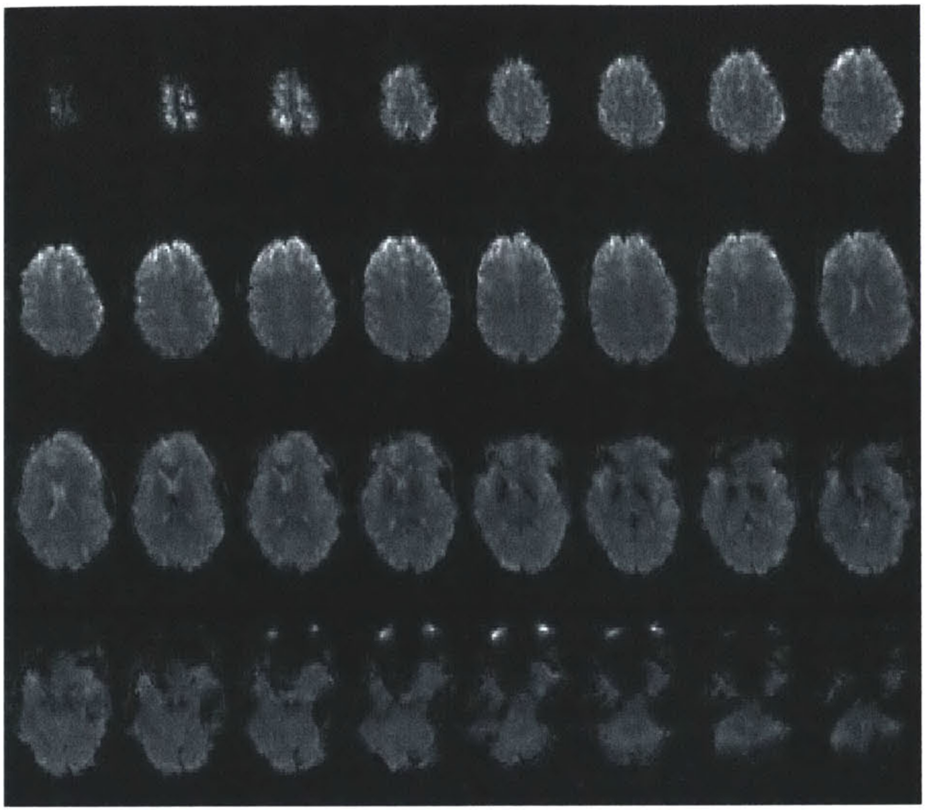

Figure 2-4: Reconstruction of 16-shot auto-calibration acquisition shown axially. Only the superior 32 slices are shown.

2.3.2 GRAPPA "g-factor"

The GRAPPA g-factor maps were generated for the phantom scan based on both a sagittal slab acquisition such as the one used by the human scans, as well as for an axial slab. All other parameters were kept constant. The g-factor maps for the sagittal slab can be seen in figure 2-7 and the maps for the axial slab can be seen in figure 2-8. It can be seen that the g-factors in sagittal slab are high in the center and inferior parts of the phantom, while they are moderate in the superior and peripheral parts of the phantom. In the axial acquisition the high g-factors are wider-spread and consume most of the center section of the phantom.

The difference between the two slab orientations can be explained with the 32 channel head coil having more encoding power in the axial plane than along the z-direction, so that the accelerated axes should be in the axial plane. Furthermore, the g-factor pattern in the axial slab is favorable for human brain imaging as much of

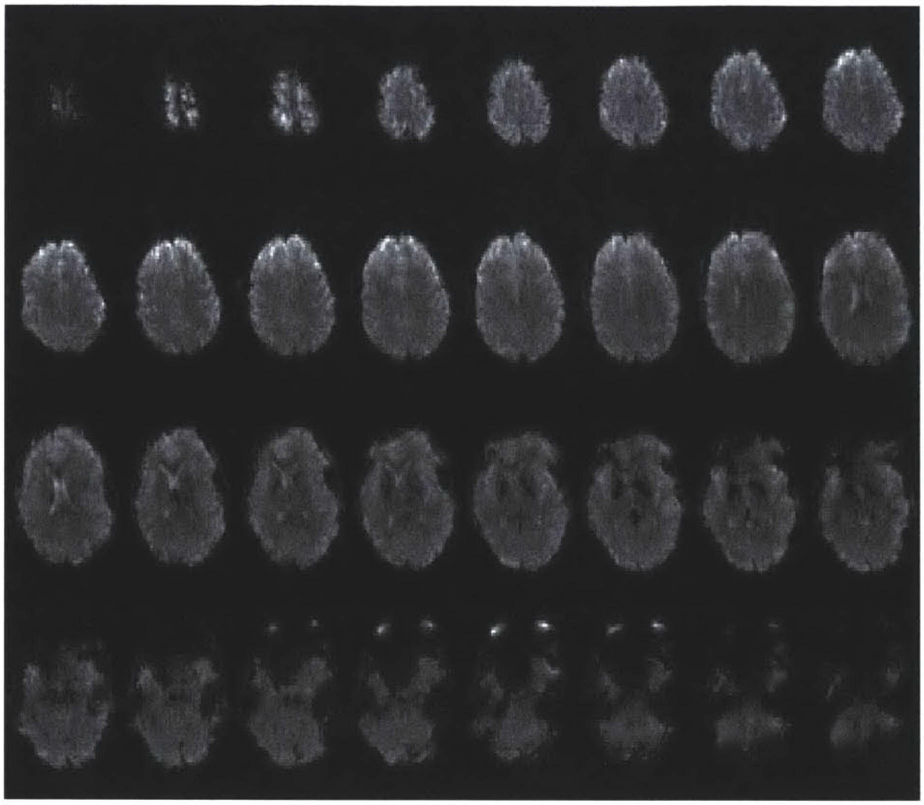

Figure 2-5: GRAPPA reconstruction of fully relaxed single-shot scan shown axially. Average of 10 time points. Only the superior 32 slices are shown.

the cortical gray matter would occupy the areas with the lower g-factors. A g-factor map generated based on a sagittal human scan can be seen in figure 2-9, confirming a similar distribution of g-factors in the human brain. Based on these maps one can expect a noise-amplification compared to a non-accelerated scan by a factor of 2 to 3 in the cortical areas and higher than 5 in the central and inferior areas of the brain, in addition to the SNR loss of $\sqrt{16} = 4$ to the reduced sampling, compared to a non-accelerated scan. Such a non-accelerated scan is however impossible to acquire.

The empirical observation of the orientation differences in g-factor maps as well as the possibility of using non-selective excitation influenced the decision to perform human experiments in sagittal slab orientation.

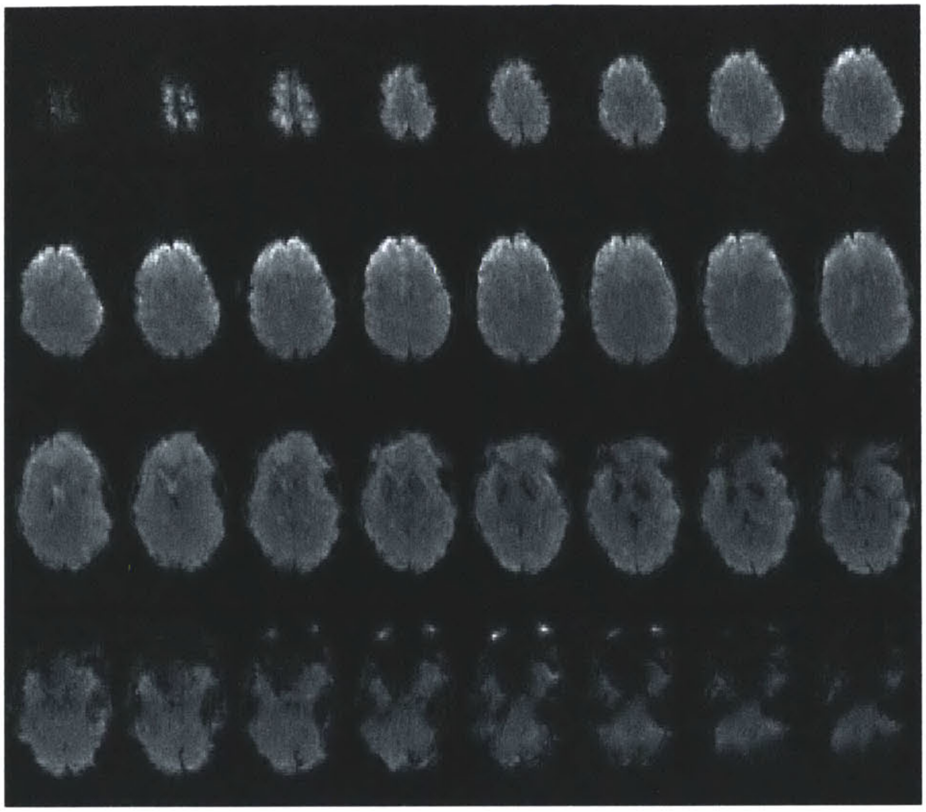

Figure 2-6: GRAPPA reconstruction of TR=120 ms single-shot scan shown axially. Average of 10 time points. Only the superior 32 slices are shown.

2.3.3 tSNR

Both thermal noise and physiological noise influence the temporal SNR, but in typical fMRI protocols the temporal SNR is usually limited by the physiological noise influence[11], rather than the thermal noise. Before looking at the physiological noise contributions some of the obvious thermal SNR issues stemming from the rapid sampling and the high acceleration factors should be mentioned in the following.

Reducing the TR to short times such as 120 ms will lead to a substantial loss of thermal SNR as the signal reaches a steady state at a much lower level then for longer TR, while the noise is not affected. One can maximize the thermal SNR in this scenario by using the Ernst angle or an empirically determined flip-angle that maximizes the signal. It has been suggested that one way to cope with the lower tSNR in fast imaging, is to average the images to a temporal resolution that matches a typical long TR acquisition. A simulation for this experiment is shown in figure 2-10,

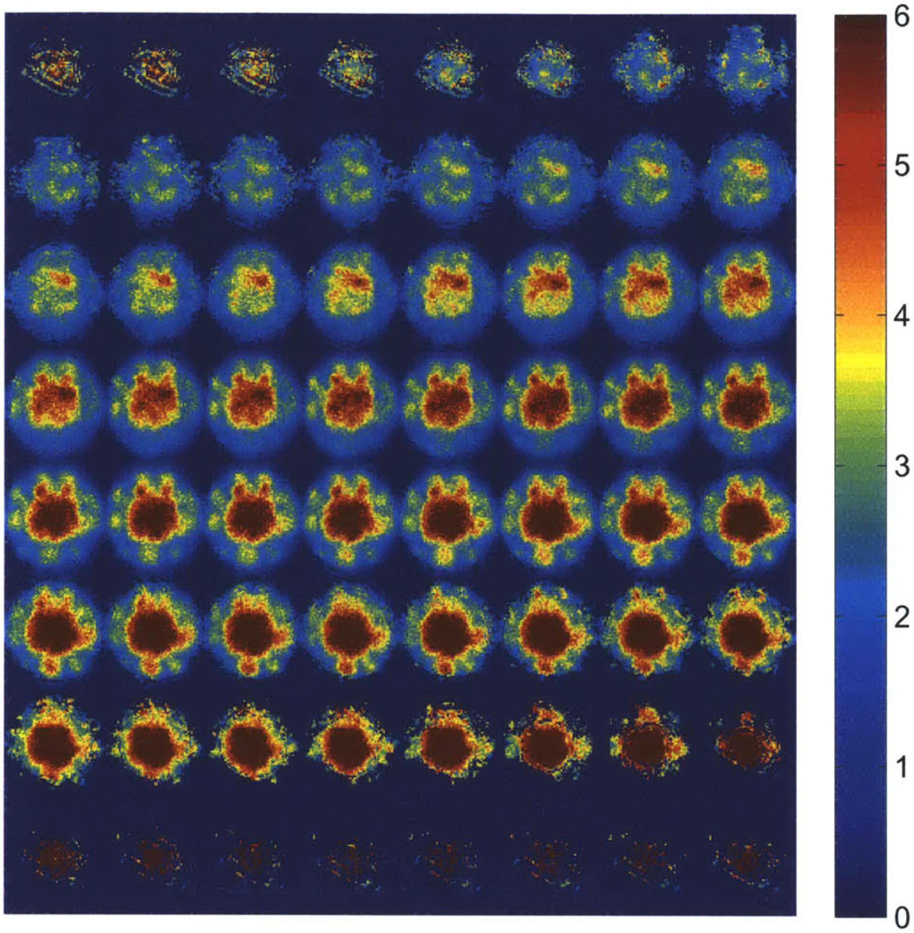

Figure 2-7: GRAPPA g-factors simulated based on a phantom scan using a sagittal slab analogously to the human protocol. Slices shown axially with superior slice on the top-left.

where a T1 value of 1200 ms for the imaged tissue is assumed, and the fast acquisition is based on a TR of 120 ms. The signal level is plotted relative to the signal after a 90 degree flip of fully recovered magnetization. The signal for the TR=120 ms is a factor of 4 lower than the signal that would be obtained at the very commonly used TR of 2 s. One can see from this simulation, that indeed the SNR loss due to shorter TR can be recovered by averaging across time, if the noise is white. As will be shown later, the physiological noise will violate that condition, so that it will be unlikely that the loss of SNR from the short TR can be recovered by averaging in human data.

Single-shot methods are favoured over multi-shot as they are supposed to reduce the influence of physiological noise, as a multi-shot method integrates the physiolog-

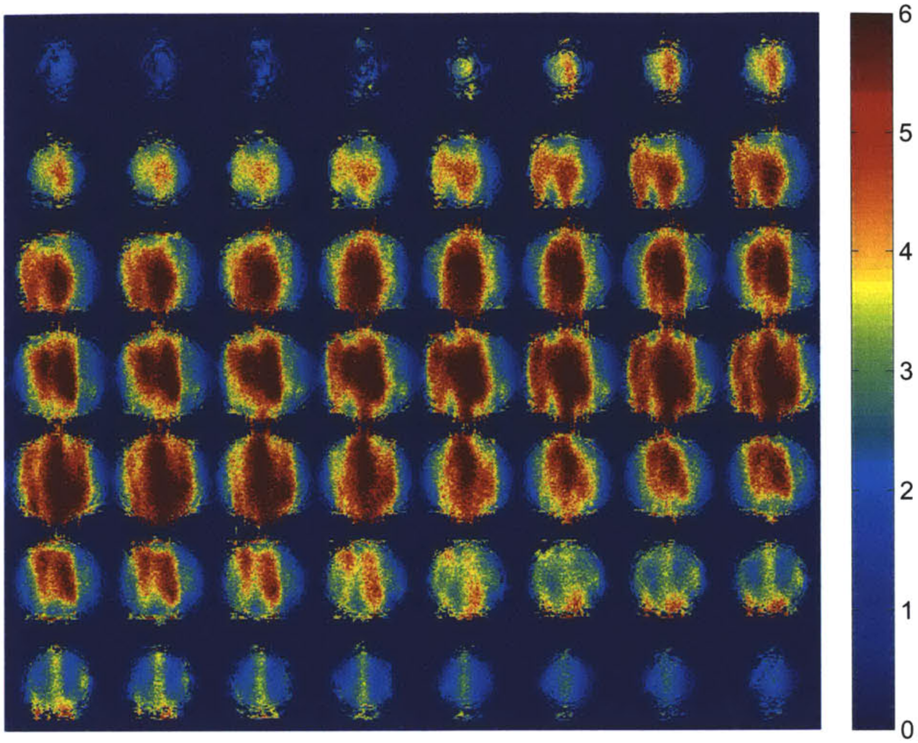

Figure 2-8: GRAPPA g-factors simulated based on a phantom scan using an axial slab.

ical noise over all shots and should therefore be noisier depending on the temporal correlation of the physiological noise. Here we are first comparing phantom data, without physiological noise, of a 16-shot interleaved multishot acquisition and and a GRAPPA reconstructed single shot acquisition. The tSNR map for the single-shot acquisition can be seen in figure 2-11 and the one for the multi-shot acquisition in figure 2-12. For the bulk of the phantom it can be seen that the 16-shot acquisition has substantially more SNR, which can be explained by both the $\sqrt{16}$ gain for the 16-shot, because it integrates 16 times more samples at the Fourier transform, as well as by GRAPPA g-factor losses in the single-shot reconstruction. The deviations from this observation on the left and right sides of the phantom might be related to a combination of several effects, with the B0-drift causing time-dependent shift along the partition-encoding direction and therefore increased artifact in the combination of the shots, which might reduce the SNR in the multi-shot acquisition. Furthermore increased distortion and susceptibility blurring might effectively increase the SNR in

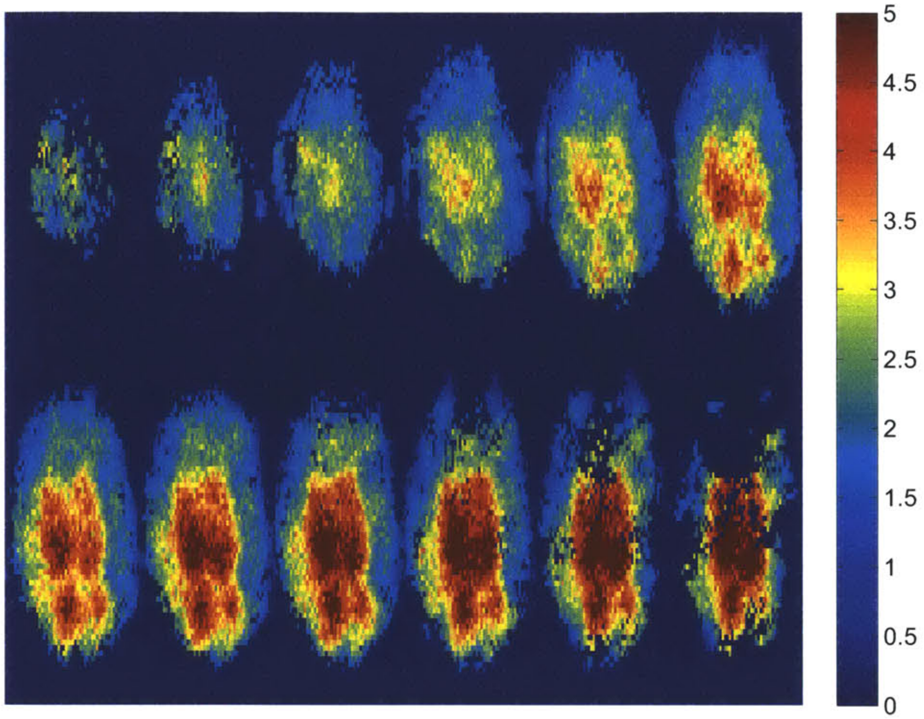

Figure 2-9: GRAPPA g-factors simulated based on a human scan using a sagittal slab. 12 selected slices shown axially with superior slice on the top-left.

these areas, which could explain the higher SNR seen in the single-shot acquisition. While the multi-shot acquisition would see both effects, the segment combination issue might be dominant enough to yield a net SNR loss.

In human EVI acquisition the situation is quite different. The tSNR map calculated from 128 volumes of 16-shot EVI can be seen in figure 2-15, for 128 volumes of the single-shot EVI in figure 2-16 and the ratio of single-shot tSNR to 16-shot tSNR in figure 2-17. It is apparent that the 16-shot combination does not have a tSNR advantage over the single-shot acquisition in large parts of the brain, despite the fact that it uses 16 times more samples and it doesn't suffer from GRAPPA noise amplification. There is several reasons for this. Most importantly that it is extremely difficult to combine the 16 interleaved segments robustly across time in the presence of subject motion, even if its very small, leading to ghost artifacts that are very unstable across time. A further consideration should be the presence of physiological noise, which diminishes the advantage of having 16 times more samples for

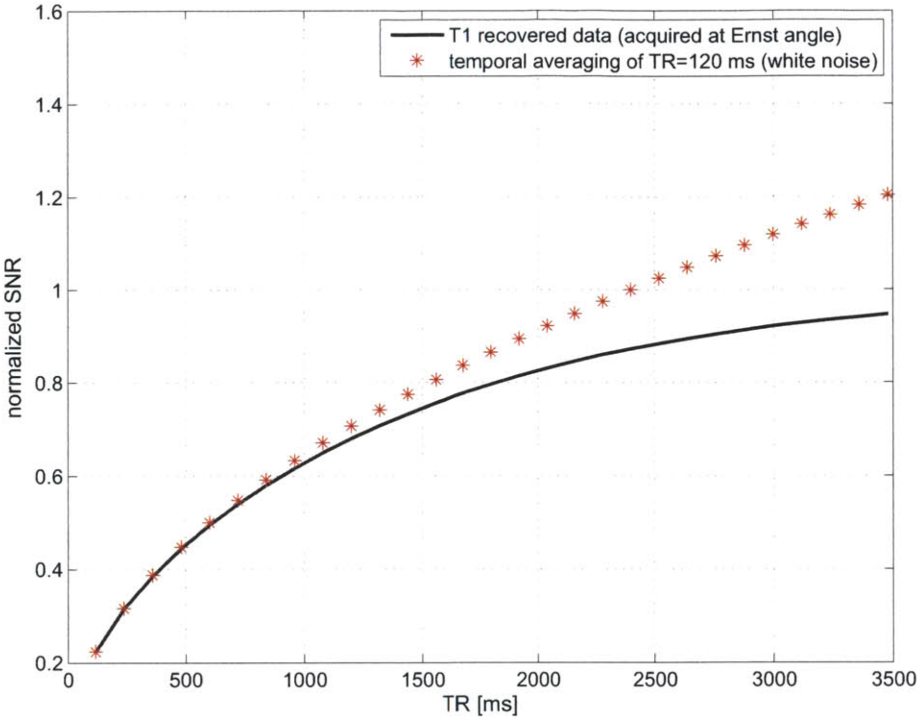

Figure 2-10: Plot of the SNR relative to a fully relaxed 90 degree excitation, for steady-state signal at given TR and Ernst angle (black curve) and averages of the steady state signal at TR=120 ms and 21 degrees flip (red stars). White noise is assumed for the averaged short-TR acquisition. It can be seen, that starting with a TR of 1500 ms the averages of the TR=120 ms acquisitions have better thermal SNR than an acquisition performed at a TR of 1500 ms. The presence of temporal autocorrelation in human data will prevent this from being a realistic scenario.

the multishot acquisition, for the noise in subsequently acquired segments is likely correlated. While the unstable segment combination in the 16-shot acquisition overshadows the tSNR measurement to the point that judgements regarding the influence of temporally correlated noise cannot be made, this is still not an unfair comparison, as motion is a form of physiological noise and the the temporal instability is caused by it. If one wanted to improve the tSNR of the multi-shot acquisition by means of corrections of the data, a segment-navigated image reconstruction could be devised, where each segment's data could be used as navigator. The individual segments could be reconstructed using a parallel imaging technique such as GRAPPA, followed by motion detection with conventional motion correction software. Then motion correction could be applied to each of the segments original data, before combining them.

While such a technique was not implemented here, it would likely improve the tSNR of the multi-shot time series substantially.

A different way of probing the influence of temporally correlated noise on the tSNR is to use temporal averages of the single-shot time series. Averages of 128 packs of 16 time-points were performed and the tSNR of the new time series was calculated. If the noise were white, a uniform gain in tSNR of a factor of $\sqrt{16} = 4$ compared to the single-shot time series would be expected. The actual map can be seen in figure 2-18, and it shows clearly that the SNR gain is substantially below 4 everywhere outside the center. To further demonstrate this effect two groups of voxels were extracted from the data, the "poor SNR gain" group including all voxels that had a tSNR gain of less than 2, and the "high SNR gain" group which had a tSNR gain of greater than 3. The mean auto-correlation functions for each group are plotted in figure 2-13 up to a lag of 20 seconds. From the plot of the auto-correlation of the "high SNR gain" group in the center of the brain it can be seen there there is little significant auto-correlation beyond the lag of one sample, besides some small periodic correlations stemming from cardiac and respiratory signals. On the other hand the "poor SNR gain" group shows significant auto-correlation for up to 20 seconds, indicating long lasting temporal correlations. A similar perspective on the same data is provided by the average frequency spectra shown in figure 2-14. Apart from the cardio-respiratory signals the "high SNR gain" group has a flat spectrum for frequencies higher than 0.1 Hz, while the "low SNR gain" group shows coloured noise for almost the entire frequency band resolved in the spectrum, explaing the poor SNR performance during averaging. Phantom data is plotted for reference as well.

The "high SNR gain" group of voxels seems to occupy roughly the same area as the high GRAPPA g-factors, which would suggest that the noise introduced by GRAPPA in those regions is essentially thermal noise. If that is the case, this could lead to the redeeming feature that temporal averages of highly accelerated single-shot EVI data would have more uniform tSNR as a result of the GRAPPA noise canceling over time faster than the rest of the voxels. A second hypothesis is, that the center parts of the brain are dominated by white matter, which might have different auto-correlation properties than the gray matter and therefore gain faster in tSNR, however the lack of spatial resolution in the data shown here does not allow for such a conclusion at this time.

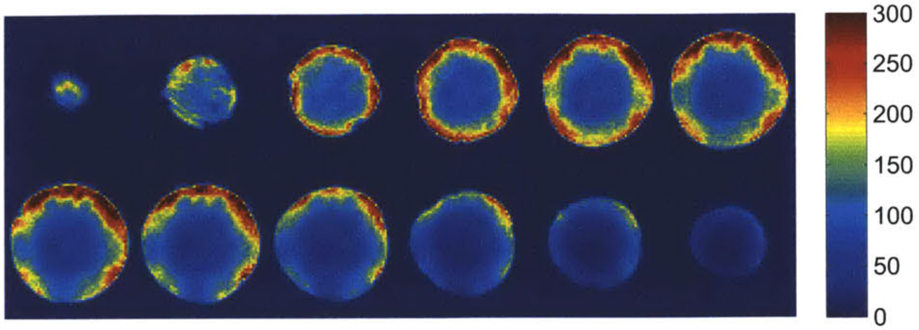

Figure 2-11: Temporal SNR of the single shot EVI acquisition of the agarose phantom. Axial cuts, 12 slices out of 64 shown in superior to inferior order.

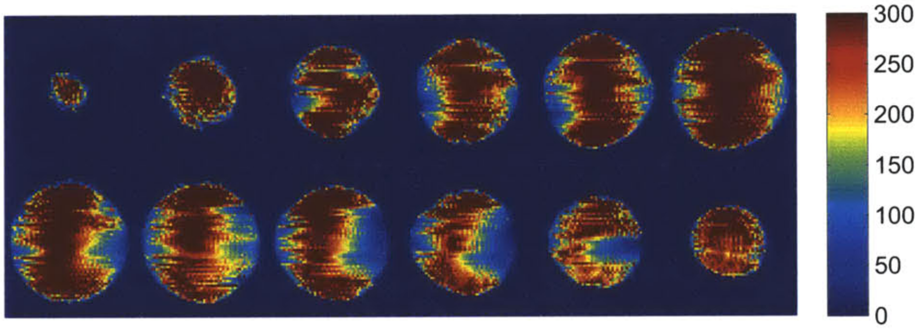

Figure 2-12: Temporal SNR of the 16-shot EVI acquisition of the agarose phantom. Axial cuts, 12 slices out of 64 shown in superior to inferior order.

An interesting issue arises from the wide noise bandwidth of the EVI time series data. The BOLD signal occupies mostly the low frequency range below 0.5 Hz, while an acquisition with a TR of 120 ms has a noise bandwidth of over 4 Hz. When measuring the variance of the data for the purpose of performing fMRI statistics, the statistics will always be penalized by out-of-band noise. One way of dealing with this is to simply lowpass filter the data at 0.5 Hz, so only noise in the BOLD passband is taken into account for variance measurements. Performing this reduction of the noise bandwidth by a factor of 8, yields a new time-series SNR which is 2.5 times improved over the full bandwidth tSNR measurement. The according maps can be

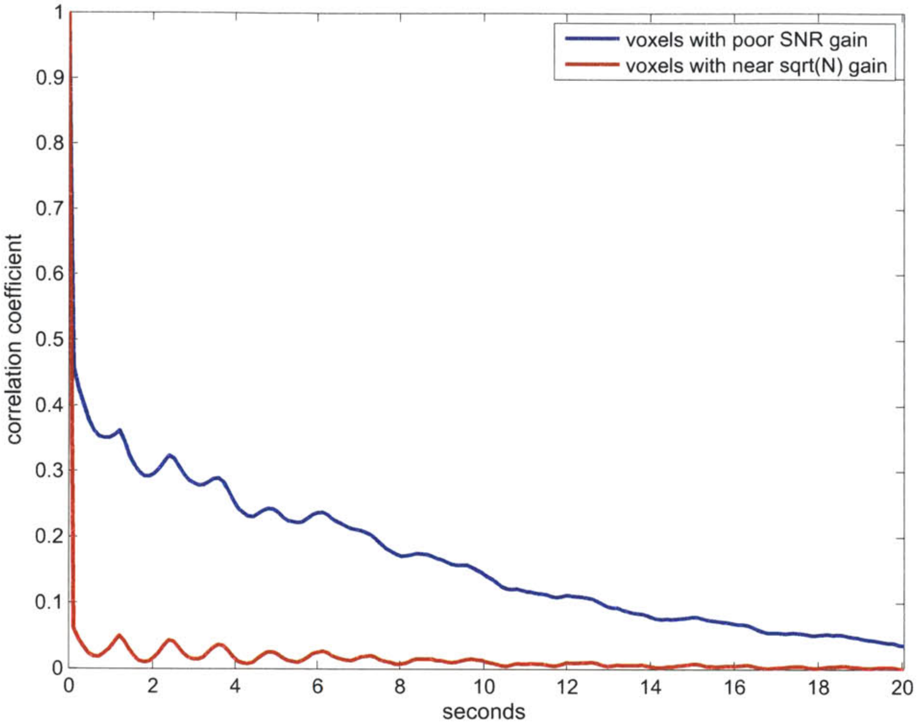

Figure 2-13: Plot of average auto-correlation functions for the groups of voxel, which have poor tSNR gain (gain < 2) in temporal averaging over 16 time-points (shown in blue), and those that have high tSNR gain (gain > 3), close to the ideal $\sqrt{N}$, shown in red.

seen in figure 2-19. Most interestingly this low-pass filter leads to an almost $\sqrt{N}$ improvement even in the cortical regions, which means that the noise above 0.5 Hz is almost white. It is also at contrast to averaging across time, which did not lead to a tSNR improvement of this magnitude due to the long autocorrelations in the cortical areas.

2.3.4 fMRI

The fMRI result in one subject can be seen in figure 2-20. The activity occurs contralateral to the stimulus as expected. The maps are thresholded at $t > 10$. It should be noted that none of the temporal auto-correlation was taken into account, nor is the selected canonical hemodynamic response function optimal for this data. The visual response to the stimulus is however robust enough to be easily picked up by a simple GLM. Further improvement in the detection sensitivity could be achieved by

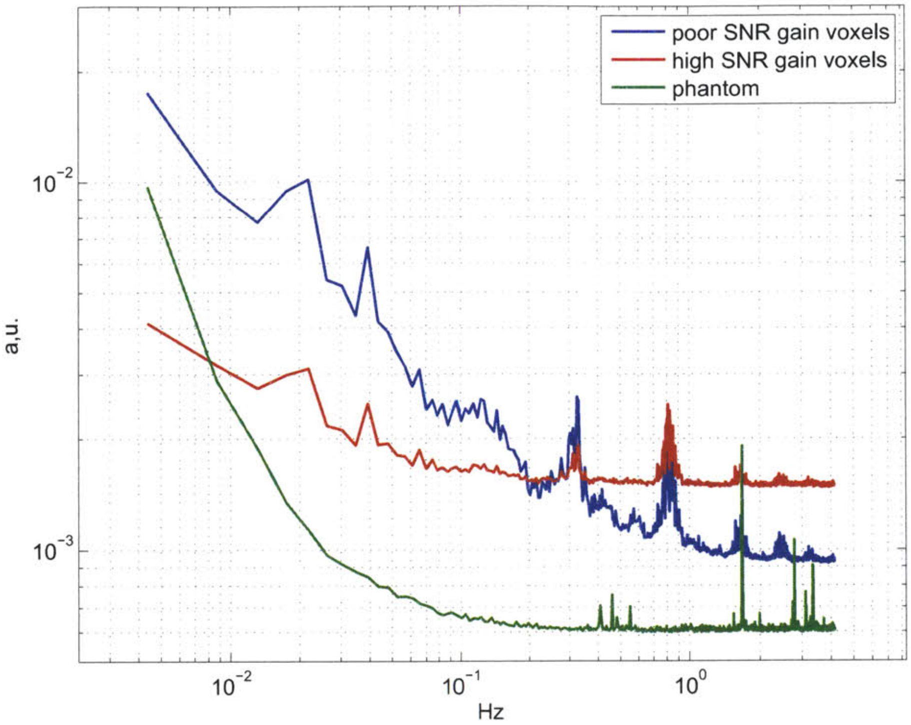

Figure 2-14: Plot of the noise spectra for the group of voxels with poor tSNR again, the voxels with high SNR gain and the agarose phantom. The human data shows distinct spectral peaks for respiration at 0.3 Hz, cardiac at 0.8 Hz as well as higher harmonics of the cardiac. A distinctive peak visible at 0.02 Hz appears to be due to a global signal, which can be removed. While the high-SNR gain voxels still feature cardio-respiratory noise components, the noise spectrum is flatter than than in the other group and thus explains the higher tSNR gains after averaging time points. The prominent peaks in the phantom data seem to stem mainly from voxels on the phantom border and are likely artifactual.

addressing those issues, however the prinicpal task of demonstrating BOLD sensitivity and the ability to localize the activity correctly has been achieved by this simple experiment. Further work is also needed to correctly measure contrast-to-noise ratio (CNR) from this data and to identify voxels with strong vascular contribution in order to measure the correct effect size. Another interesting issue arises from the observation of a strong low-frequency component apparently explained by a global signal as seen in figure 2-14, which suggest a global signal regressor might be benefitial in the GLM.

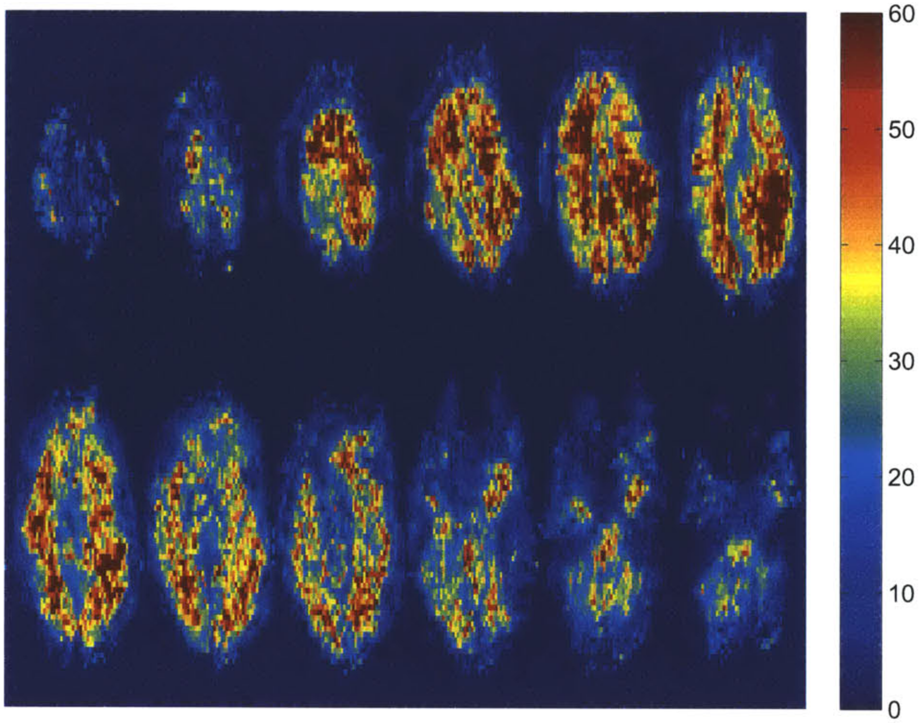

Figure 2-15: Temporal SNR of the 16-shot EVI acquisition of human brain. Axial cuts, 12 slices out of 64 shown in superior to inferior order.

2.3.5 physiological noise

The average power spectrum for the voxels that were activated in either condition of the fMRI experiment are plotted in figure 2-21. The power spectrum calculated from the stimulated runs is plotted in red, and the power spectrum of the same voxels during the rest runs is plotted in green. Peaks are clearly visible for the cardiac frequency at 1.2 Hz and its first harmonic at 2.4 Hz. Furthermore a peak can be seen at the frequency of respiration of 0.3 Hz. The most energy in the spectrum is at the frequencies below 0.2 Hz for both the stimulated run as well as the rest run, where the low-frequency component during the rest run is still assumed to be BOLD fluctuations at rest caused by resting state activity. The biggest interference to the BOLD response is the respiratory signal as it overlaps somewhat with the BOLD response in the spectrum, its power is however an order of magnitude less than that of the BOLD response in the activated run, so its influence on the detection of the BOLD signal might be negligible. For the rest run however, this difference is only about a

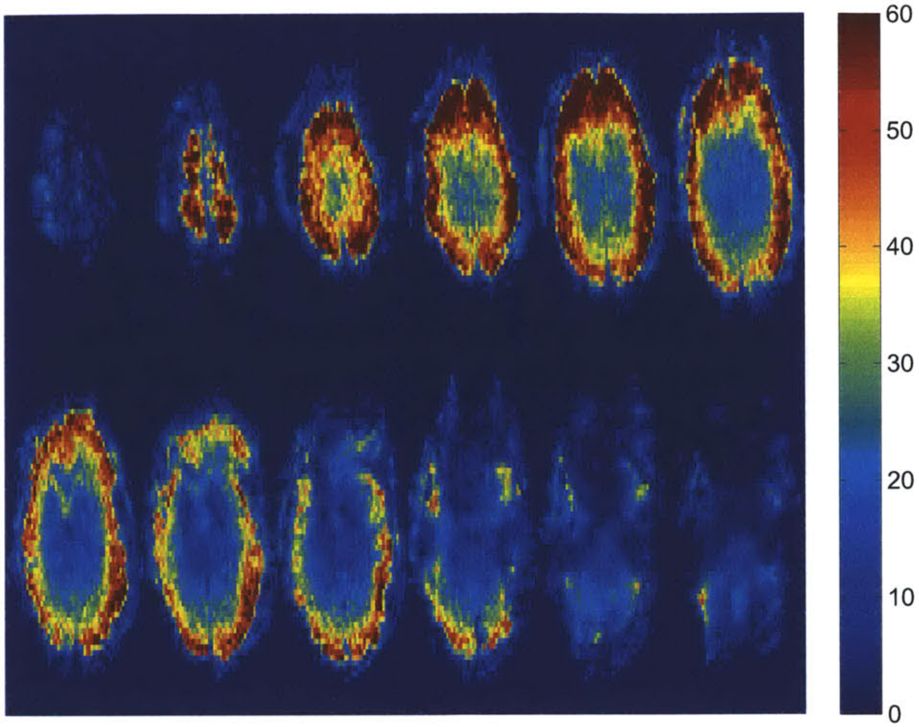

Figure 2-16: Temporal SNR of the single shot EVI acquisition of human brain. Axial cuts, 12 slices out of 64 shown in superior to inferior order.

factor of 2, so that for resting-state BOLD analysis, separation of the respiratory signal might be necessary.

The map of the spatial power distribution at the cardiac frequency of 1.3 Hz can be seen in figure 2-22. One can clearly see that most of the power seems to be located in voxels located in and around what appears to be major arteries in the neck, as well in some focal points of the brain, where major arteries might be located. It is not obvious whether this is due to pulsation of the tissue in and around the blood vessel, or whether the signal intensity of the blood itself changes with the frequency of the cardiac pulsation. Any fMRI activity in locations shown in this map would be likely severely compromised by cardiac fluctuations.

Similary a map at the respiratory frequency of 0.3 Hz has been created and can be seen in figure 2-23. The distribution of power at this frequency seems to be dominantly along the tissue-CSF interface and most pronounced along the partition-encoding direction (left-right). To my knowledge, there is no respiration related motion of the

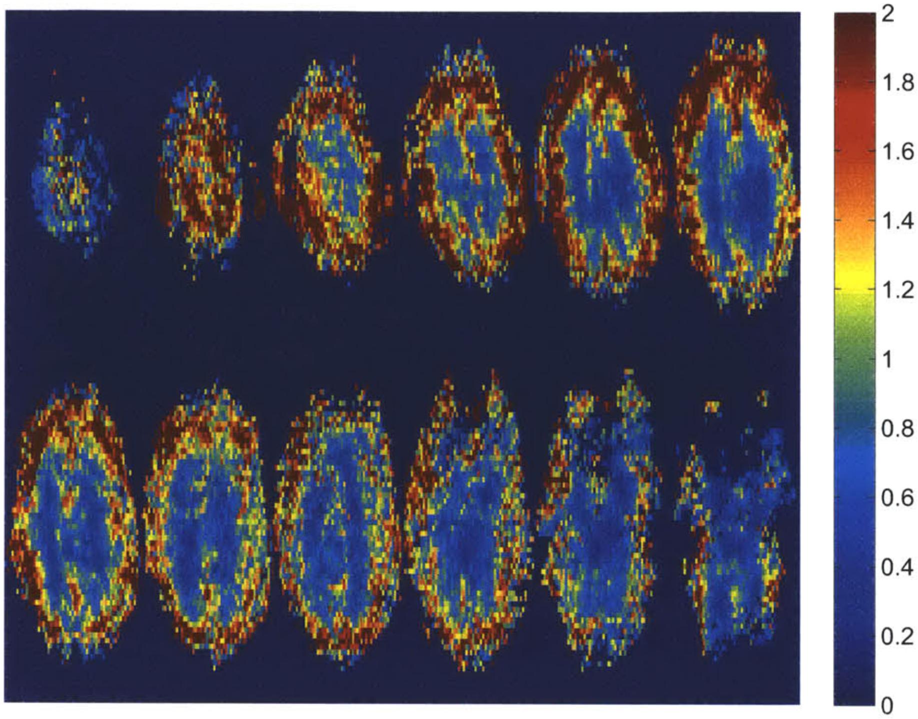

Figure 2-17: Ratio of temporal SNRs between the single-shot EVI acquisition and the 16-shot EVI acquisition of human brain. Axial cuts, 12 slices out of 64 shown in superior to inferior order. The single-shot data appears to have higher tSNR in the cortical areas, and less tSNR than the multi-shot acquisition in the center and inferior areas of the brain, where the g-factor losses dominate.

brain along the left-right direction of the brain. The map likely shows a secondary effect of B0-field changes in the brain due to changes in the lung air-volume during the respiratory cycle. This effect was characterized by van de Moortele et.al. at 7 T [12], however the same can be observed at 3 T, ifthe phase-encoding/partition-encoding bandwidth is low enough as well. When the subject breathes the lung volume changes, and causes a large susceptibility gradient which reaches all the way to the brain. As a result of the B0-field change, phase accumulates during the volume acquisition along the partition-encoding direction. This phase-ramp is then converted into translation of the image along the partition-encoding direction during the image reconstruction as effect of the Fourier-shift theorem. When the data is motion-corrected, the motion parameter along the partition encoding direction usually shows strong respiratory-wave like time-courses, which would further evidence this phenomenon. The inter-

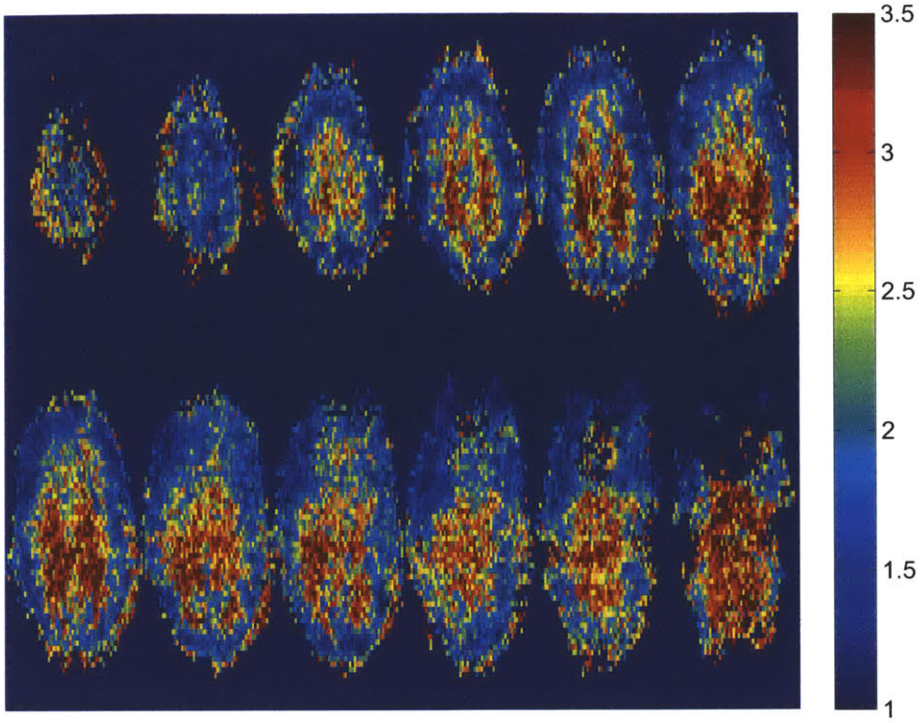

Figure 2-18: Ratio of tSNR between the series of averages of 16 time-points and the individual volume time series. Axial cuts, 12 slices out of 64 shown in superior to inferior order. It appears that there is high SNR gain by temporal averaging in the central areas that have high g-factors as well as some white matter structures, while there is very little tSNR gain in the cortical areas. If the noise were temporally white, a tSNR gain of 4 would be expected.

polation of the voxels along the tissue interface performed by the motion correction then leads to these voxels having intensities correlated in time with the respiration. This effect can probably be corrected by using an approach similar to the DORK method introduced by Pfeuffer et.al. [5], however the DORK method is designed under the assumption that the respiratory field shift is global inside a single axial slice, and in EVI, being a 3D method the situation is not that simple. Likely, a three-dimensional fieldmap as function of respiratory belt data can be trained from a small free-breathing dataset, and could then be used to perform corrections of this phenomenon based on respiratory belt recordings.

Lastly, the use of the pulse oxymeter data directly as regressor in the fMRI analysis GLM was investigated. For this purpose the pulse-oxymeter data was temporally aligned to the EVI time-series and resampled to the same sampling pattern. Due

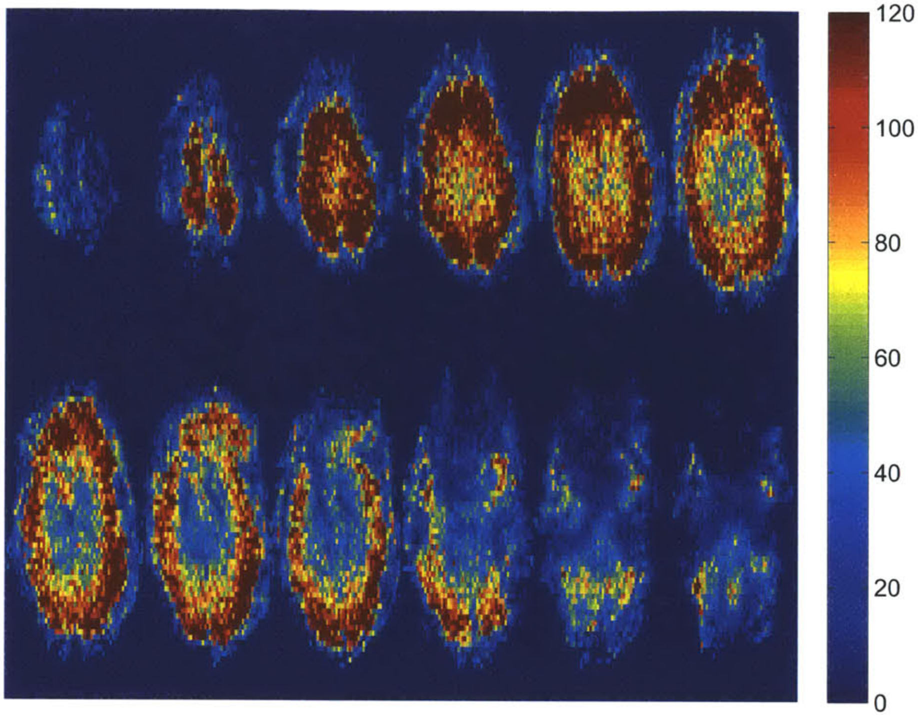
120
100
80
60
40
20
0

Figure 2-19: Temporal SNR of the single shot EVI acquisition of human brain, lowpass filtered at 0.5 Hz. Axial cuts, 12 slices out of 64 shown in superior to inferior order.

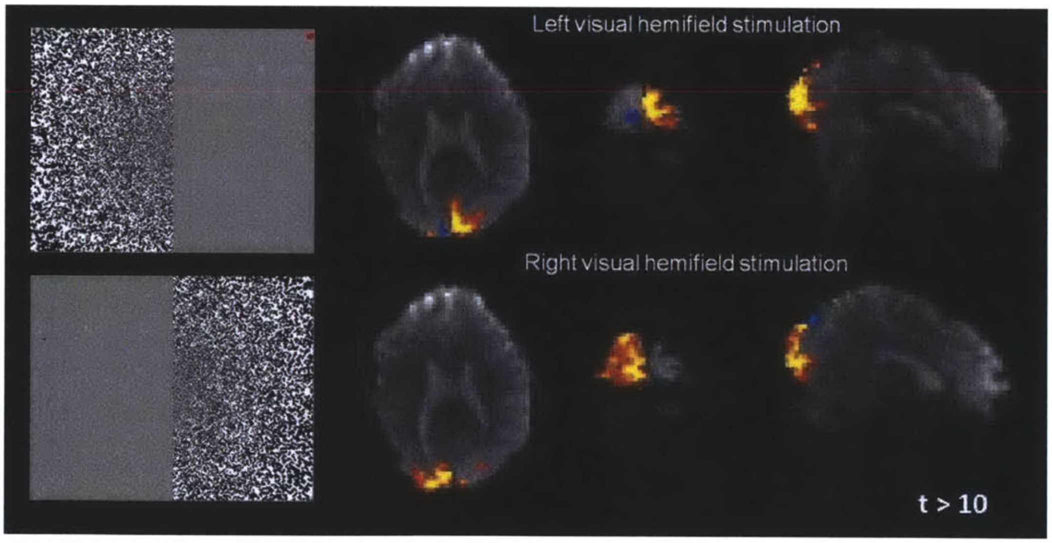
Left visual hemifield stimulation
Right visual hemifield stimulation
t > 10

Figure 2-20: Result of the basic GLM analysis of the visual hemifield task. All 8 runs were combined using a simple fixed-effects model. Overlay thresholded at a t-score of 10. The activity nicely localizes to the contra-lateral hemisphere of the stimulated visual hemifield as would be anticipated.

to the delay between the pulse-oxymeter placed on the finger and the pulse in the

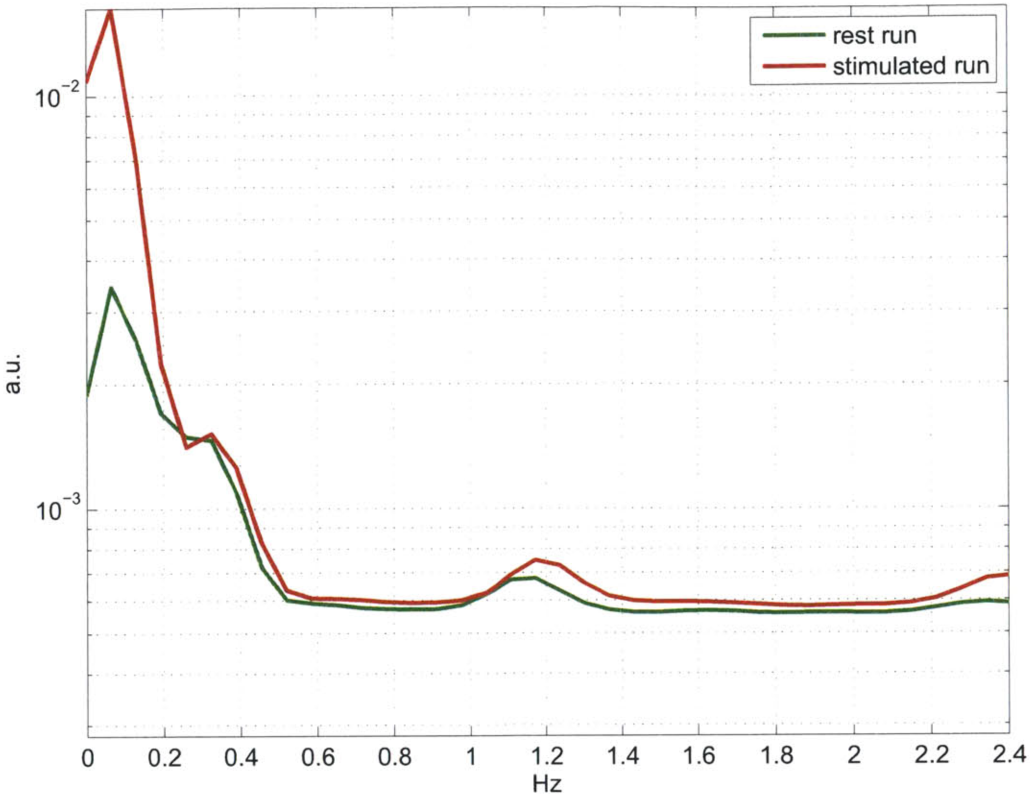

Figure 2-21: Power spectrum for the voxels that were activated in either condition during the fMRI task. Furthermore the power spectrum is plotted for the same voxels, but using time-series data from the rest runs. In both the stimulated runs, as well as the rest runs peaks can be seen for the cardiac frequency (1.3 Hz) and its harmonic, as well as the respiration frequency (0.3 Hz). By power, the respiration has the biggest influence on the signal, although its about an order of magnitude below the activated voxel signal. There is significant fluctuation in the low-frequency band, even during the rest run.

brain, a per-voxel GLM with an individually fitted delay had to be generated. Simple cross-correlation to determine the optimal delay was used, and it was found as the brain leading by 200 to 400 ms. The spatial map of the coffecients of regression from such a GLM can be seen in figure 2-24. It roughly resembles the map shown based on the cardiac frequency shown in figure 2-22. A more sophisticated way needs to be found to correctly determine the lag between the pulse oxymeter and the brain tissue voxels, and the resampling of the pulse-oxymeter data has to be adjusted for that as well, this figure clearly demonstrates that pulse oxymeter data can potentially be used directly as regressor in fMRI analysis techniques in order to regress out effects

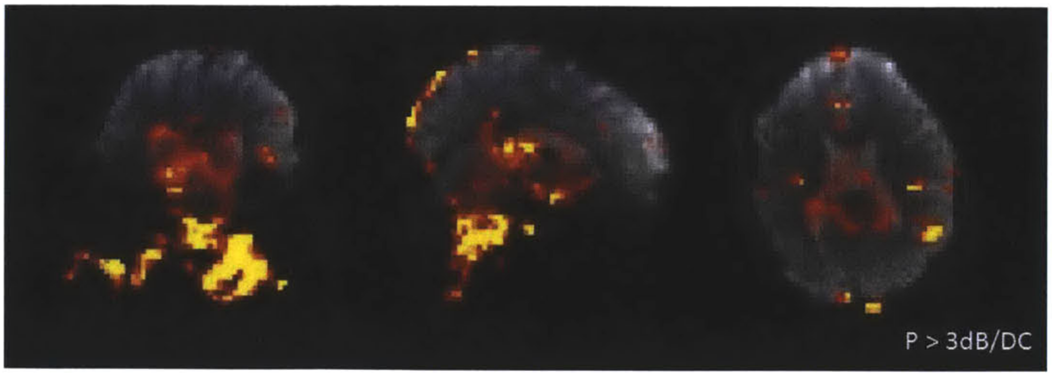

Figure 2-22: Spatial map of the power at the cardiac frequency of 1.3 Hz. The map has been thresholded at a level of 3dB above the DC-power of each voxel. The map shows clearly highly localized distribution at this frequency, which appear to be co-located to major arteries.

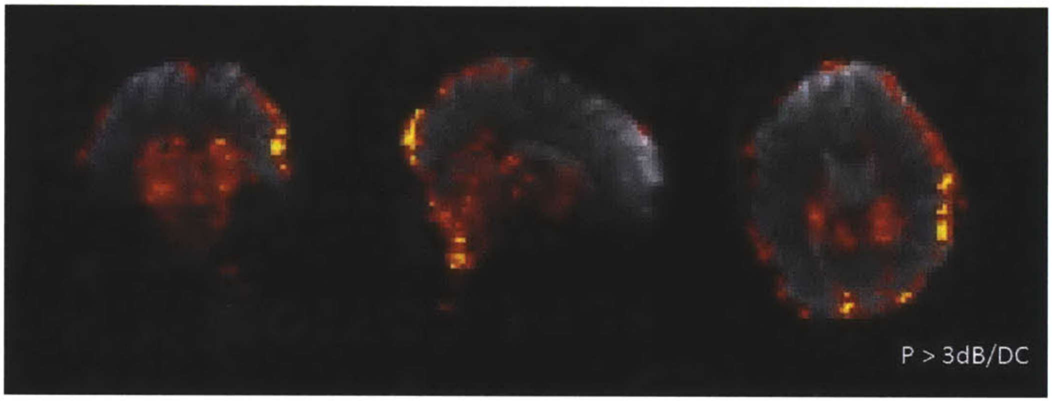

Figure 2-23: Spatial map of the power at the respiratory frequency of 0.3 Hz. The map has been thresholded at a level of 3dB above the DC-power of each voxel. The map shows most of the power to be at the tissue-CSF interface, dominantly along the partition-encoding direction.

related to brain pulsation.

2.4 Discussion

It was shown that single-shot EVI can be used for BOLD imaging at 3 T. Images with acceptable spatial resolution (3.25 mm nominal) were obtained with a temporal resolution of 120 ms and simple GLM analysis was able to detect activity in the expected location. In addition it was shown that physiological fluctions stemming from cardiac- and respiratory cycles are temporally and spectrally resolved at that

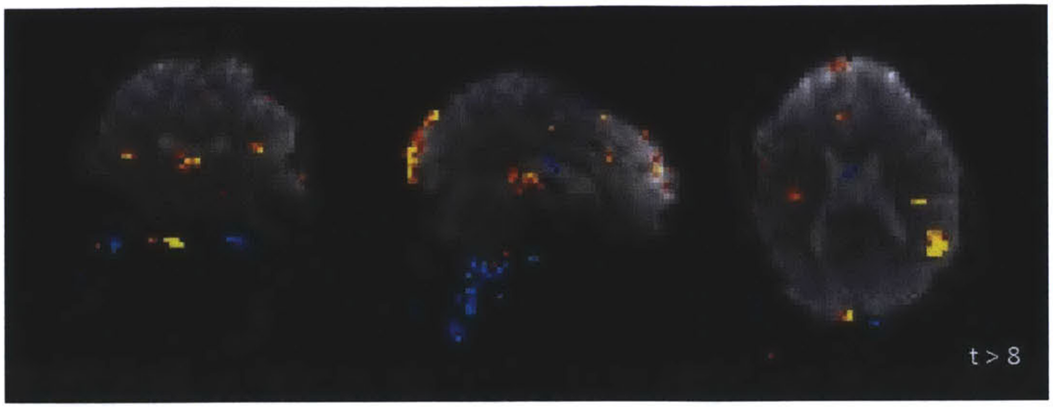

Figure 2-24: Spatial map of the coefficient of regression for the pulse-oxymeter regressor in the GLM. Again, similary to the cardiac frequency map, highly correlated voxels appear to be highly localized and appear to be co-located with major arteries.

temporal resolution. To my knowledge this is currently the fastest existing whole-brain imaging method with that spatial resolution that also generates images. Other 3D methods that provide this or a faster sampling rate are either heavily based on prior information or are only imaging changes relative to a baseline, not actually generating images for each individual time point.

This provides however only a starting point for EVI as functional imaging method. Analysis utilities that can handle the temporal resolution of the data or are able to attach statistical significance to the results obtained with this method, have yet to be developed. Initial analysis were performed using a canonical hemodynamic response function, which does not match the true hemodynamic response. It is doubtful that the exisiting hemodynamic response models can be setup to match the actual HRF with the temporal precision that they are measured in using EVI. The data that we have collected so far does not lend itself to the estimation of the HRF parameters, or the HRF itself. A different experimental design, providing more trials and single events, rather than blocks of activation, would need to be performed to allow the estimation of the HRF. A potential confound in this is that the spatial resolution is still less than nominal due to the readout duration being a bit longer than T2*. This is the likely cause for the longer autocorrelation functions seen in EVI compared to EPI. Increasing the spatial resolution will definitely increase the usefulness of EVI for functional imaging of the brain. There is two ways this can practically be achieved immediately. One is to use a head-gradient set, which allows the echo-spacing and therefore the readout duration to be cut in half. The second path would be to perform a slab selective EVI, giving up the whole brain coverage, which would also drastically reduce the readout duration, in favour of improved actual spatial resolution.

Furthermore, the spatial distortions make it difficult to coregister the EVI images to structural images taken of the subjects. Attempts were made to correct the distortion by using point spread function encoding similar to the work by Zaitsev et.al.[15], and data was collected with this method for several subjects, however the image processing required to perform distortion correction using the measured point spread functions exceeds the scope and time frame alotted for this thesis, so it is left for the future.

In the data collected for this studu the fMRI paradigm has no spectral overlap with either the cardiac or respiratory disturbances, so a simple GLM based on the paradigm suffices to separate these signals from the BOLD response. Removing these components therefore has no effect on the result at all. If the benefit of removing these signals was to be researched, a new experiment, possibly of event-related single-trial design, would have to be created, where there would be overlap between the cardio-respiratory signals and the BOLD response, and the removal of those components should actually lead to an improvement in BOLD detection sensitivty.

The tSNR results from the human studies performed so far appear to show that the time-series SNR is in fact physiological noise limited, as a measured time-series SNR of over 120 (see figure 2-19 should be close to the asymptotic physiological noise limited tSNR for a spatial resolution of $3.4 \times 3.4 \times 3.4\,\mathrm{mm}^3$ according to Triantafyllou et.al. [11]. Even if the spatial resolution is less than that, the tSNR would still be close to the asymptotic limit. This is interesting, considering the amount of thermal SNR reduction caused by the GRAPPA g-factor losses, $\sqrt{R}$ losses and the short TR compared to T1. This would indicate that possibly even higher acceleration factors could be used while maintaining an adequate tSNR, as the thermal SNR losses are not yet the limiting factor. Of course these statements apply only to the high-tSNR region visible in the tSNR maps, not to the center regions, where GRAPPA g-factor losses dominate.

Bibliography

[1] M. A. Griswold, P. M. Jakob, R. M. Heidemann, M. Nittka, V. Jellus, J. Wang, B. Kiefer, and A. Haase. Generalized autocalibrating partially parallel acquisitions (GRAPPA). *Magn Reson Med*, 47:1202–1210, Jun 2002.

[2] P Mansfield. Multi-planar image formation using nmr spin echoes. *Journal of Physics C: Solid State Physics*, 10(3):L55, 1977.

[3] P. Mansfield, R. Coxon, and J. Hykin. Echo-volumar imaging (EVI) of the brain at 3.0 T: first normal volunteer and functional imaging results. *J Comput Assist Tomogr*, 19:847–852, 1995.

[4] P. Mansfield, P. R. Harvey, and M. K. Stehling. Echo-volumar imaging. *Magnetic Resonance Materials in Physics, Biology and Medicine*, 2:291–294, 1994. 10.1007/BF01705255.

[5] J. Pfeuffer, P. F. Van de Moortele, K. Ugurbil, X. Hu, and G. H. Glover. Correction of physiologically induced global off-resonance effects in dynamic echo-planar and spiral functional imaging. *Magn Reson Med*, 47:344–353, Feb 2002.

[6] K. P. Pruessmann, M. Weiger, M. B. Scheidegger, and P. Boesiger. SENSE: sensitivity encoding for fast MRI. *Magn Reson Med*, 42:952–962, Nov 1999.

[7] C. Rabrait, P. Ciuciu, A. Ribes, C. Poupon, P. Le Roux, G. Dehaine-Lambertz, D. Le Bihan, and F. Lethimonnier. High temporal resolution functional MRI using parallel echo volumar imaging. *J Magn Reson Imaging*, 27:744–753, Apr 2008.

[8] P. M. Robson, A. K. Grant, A. J. Madhuranthakam, R. Lattanzi, D. K. Sodickson, and C. A. McKenzie. Comprehensive quantification of signal-to-noise ratio and g-factor for image-based and k-space-based parallel imaging reconstructions. *Magn Reson Med*, 60:895–907, Oct 2008.

[9] P. B. Roemer, W. A. Edelstein, C. E. Hayes, S. P. Souza, and O. M. Mueller. The NMR phased array. *Magn Reson Med*, 16:192–225, Nov 1990.

[10] A. W. Song, E. C. Wong, and J. S. Hyde. Echo-volume imaging. *Magn Reson Med*, 32:668–671, Nov 1994.

[11] C. Triantafyllou, R. D. Hoge, and L. L. Wald. Effect of spatial smoothing on physiological noise in high-resolution fMRI. *Neuroimage*, 32:551–557, Aug 2006.

[12] P. F. Van de Moortele, J. Pfeuffer, G. H. Glover, K. Ugurbil, and X. Hu. Respiration-induced B0 fluctuations and their spatial distribution in the human brain at 7 Tesla. *Magn Reson Med*, 47:888–895, May 2002.

[13] W. van der Zwaag, S. Francis, and R. Bowtell. Improved echo volumar imaging (EVI) for functional MRI. *Magn Reson Med*, 56:1320–1327, Dec 2006.

[14] Y. Yang, V. S. Mattay, D. R. Weinberger, J. A. Frank, and J. H. Duyn. Localized echo-volume imaging methods for functional MRI. *J Magn Reson Imaging*, 7:371–375, 1997.

[15] M. Zaitsev, J. Hennig, and O. Speck. Point spread function mapping with parallel imaging techniques and high acceleration factors: fast, robust, and flexible method for echo-planar imaging distortion correction. *Magn Reson Med*, 52:1156–1166, Nov 2004.

Chapter 3

Quiet Echo Planar Imaging

3.1 Introduction

In this part of my thesis I begin the sequence and image reconstruction efforts needed to tackle the problems associated with the loud acoustic noise generated by echo-planar imaging sequences. I outline the motivation behind this project, show the potential of the highly accelerated "blip-less" EPI approach taken through sound measurements of the implemented sequence, and discuss the image reconstruction problems my preliminary work has uncovered.

The acoustic noise generated by echo-planar imaging sequences poses several problems for fMRI. Firstly in some MRI machines and protocols the noise can easily reach 100 dB SPL[15, 16], which is a safety concern since the hearing of the subject could be irreparably damaged by exposure of such a noise level for the duration of the experiment. Furthermore this level of noise poses a significant challenge to the study of the auditory system, as it influences significantly how auditory stimuli are perceived and processed. It even acts as an auditory stimulus on its own. In addition, even non-auditory circuits in the human brain, such as working memory systems, are affected by the acoustic noise[9, 21, 8], thus a quieter imaging sequences might be desirable for a number of functional imaging studies. Another application of quieter EPI would be the study of sleep, in which the sleep of the subject should not be perturbed by the scanner noise. Lastly, the acoustic noise reduces the patient/subject comfort during the study, in particular in populations that might not be comfortable in participating in a fMRI study in the first place, such as pediatric subjects and adults suffering from anxiety disorders. I suspect that quieter functional imaging techniques will help alleviate the discomfort in these populations. All techniques attempting to make the MRI scan quieter without hardware modifications to the MRI machine center on reducing the amount of gradient switching as well as reducing the speed of the gradient switching (i.e. reducing the slew rate). This is because the transfer function of the acousto-mechanical response of most gradient coils seems to show fairly low levels only on the low-frequency region below its first resonant mode [10, 13]. Thus the details of these acoustical resonances is particularly important. For example, the high frequency acoustical resonance modes correspond to bending modes of a hollow cylinder and are thus sensitive to the dimensions and stiffness of the gradient coil cylinder. In the lower frequency region, the system of mounting in the bore is critical. Driving the sequence at the actual acoustic resonance frequencies of the gradient coil is usually avoided by the implementation of forbidden frequencies (or more practical forbidden echo-spacings in EPI), as they not only lead to very high intensity acoustic noise and poor image quality, but can also easily lead to mechanical damage to the gradient coil or its mounting in the magnet.

The quietest solution to this problem is the so called sparse sampling fMRI [7] (sometimes also referred to as clustered volume acquisition [4]). In this method, use is made of the fact that the BOLD response has an onset that occurs with a few seconds delay from the stimulus, so that one doesn't have to scan during the presentation of the stimulus, but still can capture the BOLD response to the stimulus by starting the acquisition after the stimulus has been presented. Of course the scanner acoustic noise will then also have its own BOLD response, so the acquisition should be stopped when the onset of the BOLD to the scanner acoustic noise occurs, leaving a short window of a few seconds only for the acquisition. Subsequently to the acquisition then one has to wait for the BOLD response to the scanner noise to disappear before presenting the next stimulus. It is obvious that this can lead to a very inefficient sampling scheme, with relatively few recorded trials in a practical amount of time, and one timepoint per stimulus or very reduced volume coverage to get multiple time points into the short acquisition window. This could be slightly improved by the use of extremely rapid imaging techniques as the single-shot echo-volume imaging technique shown in the previous chapter of this thesis, but overall, a continuous scanning technique would produce a considerably higher efficiency for auditory fMRI.

The application of continuous, quieter functional imaging techniques has been attempted before, for example by using non-EPI based imaging sequences, which rely on less gradient switching. Examples are the use of FLASH based fMRI [1] and functional BURST imaging [11]. While FLASH based fMRI was popular mostly while unshielded gradient coils (hardly suitable for EPI) were in common use, by today's standard its low temporal resolution is considered unacceptable, but its ability to achieve very high spatial resolution might still make it attractive for some study designs. The functional BURST method suffers from poor spatial resolution and poor BOLD weighting. In addition to its intrinsically inefficient nature, BURST produces a diffusion weighted contrast that destroys the intravascular contributions to the BOLD effect, which greatly reduces the sensitivity to BOLD at the commonly used field strengths of 1.5 T and 3 T.

There have also been attempts to reduce the acoustic noise from EPI pulse sequences by modifications to the EPI pulse sequence. Since parallel imaging reduces the amount of gradient switching by encoding less space, it was suggested to use accelerated imaging to reduce the acoustic noise. This was first done by de Zwart et.al. [3], using 2-fold accelerated EPI with SENSE image reconstruction. The time saved by the 2-fold reduction of gradient-encoded k-space lines, was used to slow down the gradient switch of the remaining gradient-encoded lines. This allowed a modest reduction of the scanner acoustic noise to 83 dB SPL, compared to 92 dB SPL in the unaccelerated version of the EPI sequence. The effective echo-spacing and spatial resolution was maintained in this approach, so that the image quality should generally not have suffered in exchange for the reduction in acoustic noise level. A different approach was implemented by Schmitter et.al. [19], where the blipped phase encoding commonly used in EPI was replaced by a constant phase encoding gradient, which other than at its prewinder and turn-off point at the end of the readout should make no sound at all, as its essentially a DC waveform. Schmitter furthermore made the readout waveform be a sinusoidal waveform rather than the modern trapezoids, which makes the noise from the readout waveform be very narrow-band. The readout waveform being very narrow-band, allows the EPI readout waveform to be optimized in such a way that its frequency is at a or close to a minimum in the acoustic transfer function of the gradient coil. The big downside of the Schmitter approach is that the readout waveform frequencies at which the scanner is quiet are so low that the echo-spacing gets to be very long, in their practical protocols even over 1 ms. The return to constant phase encoding and sinusoidal readout waveforms, which were used in the very early days of EPI as well, also means more difficult image reconstruction. In particular, the k-space trajectory associated with such a sequence is not cartesian, but instead is a zig-zag like cosine trajectory along k_y. While the non-linear sampling in k-space along the k_x direction can be dealt with by regridding methods, the interlaced sampling along k_y has to be addressed with interlaced sampling reconstruction. The special case that occurs in original EPI and Schmitter's quiet method has been addressed by Bracewell in 1978 [2], and successfully applied to EPI by Sekihara et.al. [20].

As part of this thesis I set out to generate an EPI sequence that is as quiet as possible, i.e. quieter than what had been achieved before while not compromising on the imaging speed and image quality. The goal is a noise level of substantially less than 70 dB SPL, so that it can be reduced to less than 35 dB SPL when ear plugs and ear muffs are added for further attenuation. Furthermore I need to maintain a 64 matrix size, yielding a nominal spatial resolution of 3.25 mm^3 and an effective echo-spacing of 0.5 ms or less, in order to not suffer from increased image distortion or blurring. Lastly it should be possible to acquire 26 slices in a TR of 2 seconds, which makes the quiet protocol entirely comparable to a "standard" fMRI protocol. In order to achieve this goal, I combine and extend the approaches of de Zwart and Schmitter. The biggest effect of this combination is that the use of accelerated imaging lets me reduce the effective echo-spacing and recover the speed lost due to slowing down the readout gradients. Furthermore, since we are now able to accelerate by more than just a factor of 2, the frequency of the readout sinusoid can be lowered well below those used by Schmitter et.al. producing even quieter noise levels. The image reconstruction of data from such a sequence now poses a significant problem. While I was able to adapt GRAPPA [6] to perform the parallel image reconstruction of the acquired data, the result is an interleaved set of zig-zag trajectories, which cannot be simply Fourier transformed without artifacts much like the data from the Schmitter sequence. When using 4-fold acceleration, the data becomes four-fold interlaced. It is not impossible to derive a 4-interlace interpolation function the same way Bracewell derived the 2-interlace equation in his book, however it will be problematic to use in practice. Interlaced-sampling (or bunched-sampling) reconstruction is theoretically possible for samples that are bunched arbitrary close, so long the signal to be reconstructed is n-times differentiable and noise-free. But, the closely bunch samples increases the noise amplification when noise is present. In the original EPI or Schmitters work, this was dealt with by either avoiding sampling close to the "corners" of the trajectory, or by agressively apodizing the corners, with the latter approach leading the effective loss of spatial resolution. The interlaved zig-zag as seen below in figure 3-1, has this problem not only at the corners, but also at the trajectory intersection points, making most of the k-space useless for such an approach. I therefore suggest an alternative approach for the image reconstruction.

3.2 Methods

3.2.1 Acoustic Measurements

All acoustic measurements shown in this chapter were performed with a Bruel & Kjaer 2238 Mediate sound level meter and Bruel & Kjaer 4188 quarter inch microphone. Both the meter and the microphone were factory calibrated by Bruel & Kjaer shortly before the measurements. The measurements were performed in a Siemens Avanto

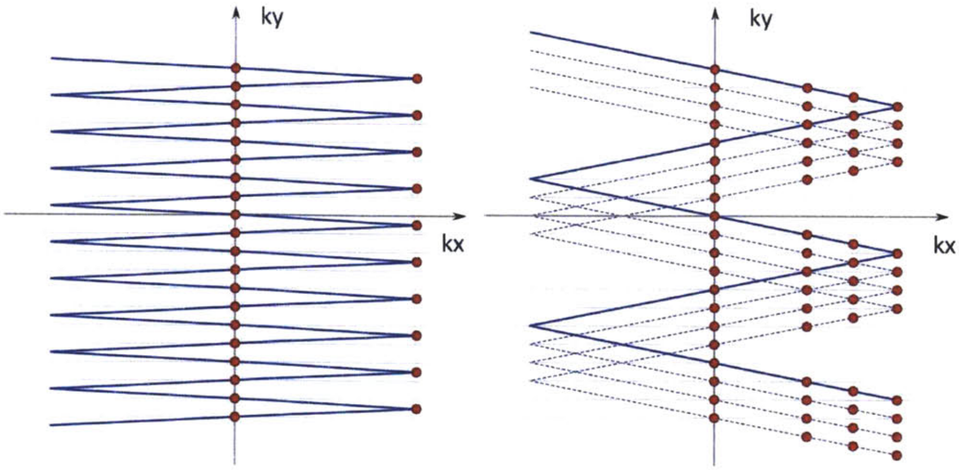

Figure 3-1: Schematic of k-space trajectories resulting from constant phase-encoding EPI. On the left, unaccelerated EPI forms a zig-zag trajectory, where only the samples at $k_x = 0$ are sampled uniformly along k_y, and the trajectory is undersampled at the extreme values of k_x. On the right, a 4-fold accelerated trajectory is shown with the solid line showing the acquired data and the stippled line showing the GRAPPA reconstructed data. The trajectory is uniformly sampled along k_y at $k_x = 0$, and undersampled not only at the corners, but also at the trajectory intersection points.

1.5 T scanner, with the microphone placed in the head coil at a location were the subjects left ear would be located. A 30 ft extension cable was used between the microphone and the noise level meter. All measurements were performed in dB A weighting. During the measurements the magnet's cold heads were turned off as well as the bore ventilation system to reduce the background noise level. Also all RF transmit was turned off in order to prevent direct induction of voltage into the microphone and microphone cable from the RF. The acoustic noise level was measured for the quiet EPI sequence proposed in this chapter as well as the MGH EPI sequence which is closely based on the Siemens stock EPI sequence. The measurements were performed for several echo-spacings, but at a fixed matrix size and slice-thickness. The number of slices was also kept constant at 26. Since the fat-supression pulse turned out to be rather acoustically noisy, several measurements were performed with the fat-suppression pulse removed.

3.2.2 Quiet EPI acquisition

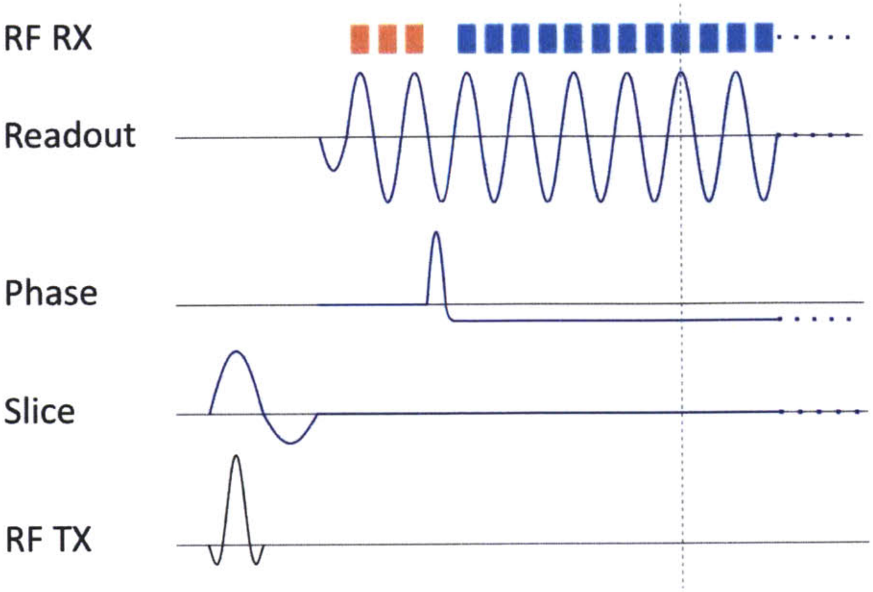

Figure 3-2: Schematic of the quiet EPI sequence. The general layout follows a regular EPI sequence, but the readout gradient waveform is sinusoidal and the phase encoding is constant, as opposed to blipped. The slice select gradient is rounded as well. Note, that the gap between the three phase-correction lines and the image lines in the readout is filled with another half-cycle to improve continuity.

The quiet EPI pulse sequence implemented with constant phase encoding gradient, sinusoidal phase-encoding prewinder and sinusoidal readout waveform is shown in figure 3-2. The gap between the three phase-correction navigator lines has been filled with another half-cycle of readout waveform to improve the continuity of the sound waveform. The slice selection gradient has been stretched and rounded sinusoidally to reduce its acoustic noise level. The readout waveform has a single fixed frequency, which now determines the EPI echo-spacing. Unlike in most implementations of trapezoidal EPI readouts, the bandwidth of the readout and the echo-spacing become uncoupled as the readout waveform frequency is a fixed parameter. If the readout bandwidth is increased, the sampling window is much shorter than the readout sinusoid half-cycle and the amplitude of the sinusoid is increased, but the echo-spacing remains fixed by the readout frequency. A slightly higher than minimal bandwidth is desirable in order to avoid sampling too close to the "corners" of the k-space trajectory where the sampling becomes bunched for the blip-less sequence. All imaging experiments were performed in a 1.5 T Siemens Avanto scanner with the Siemens product 32-channel coil.Images were acquired with a readout frequency of 500 Hz and an acceleration factor of $R = 2$ (BW=1056 Hz/px) as well as a readout frequency of 223 Hz and an acceleration factor of $R = 4$ (BW=468 Hz/px). The TE was set to 40 ms and the TR was 2 s. 26 slices with a thickness of 3 mm were acquired. The matrix size was set to 64×64, with a field of view of 210 mm, yielding an isotropic nominal in-plane resolution of 3.25 mm^2. The measurements were repeated with and without fat-suppression. The fat suppressed scans were substantially louder, however the fat-sat is effective at removing the chemical shift artifact associated with the fat frequency shift. However, many fMRI researchers have used EPI with no fat-sat in order to speed up the acquisition without adverse effects. This is possible if the fat artifact is stable in time. When assessing the reconstruction quality of the images, it is important to not confuse the fat chemical shift artifact with potential residual aliasing artifacts associated with the accelerated image reconstruction.

3.2.3 Quiet EPI image reconstruction

The preliminary image reconstruction started with the reflection of the odd readout lines, followed by the even/odd line phase-correction. The data was then regridded to make the sample-spacing linear along k_x. The regridding also transforms the k-space trajectory from a cosine along k_y into a straight "zig-zag". After regridding two separate GRAPPA [6] kernels were fit for the even and for the odd k-space lines. The reason for both the regridding and the fitting of two separate GRAPPA kernels is the requirement of a spatially invariant kernel imposed by the GRAPPA kernel. Non-linear sampling in k_x and zig-zagging along k_y would violate this condition. Regridded even lines and regridded odd lines, however allow a spatially invariant kernel to be fit. Once the GRAPPA kernels have been fit to the autocalibration lines (ACS), acquired at the beginning of the scan, they can be used to fill in the missing lines from the accelerated image data. At this point, in the preliminary image reconstruction, a simple 2D-FFT is performed to get the pilot images. Future work will concentrate on improved image reconstructions.

3.3 Results

3.3.1 Acoustic Measurements

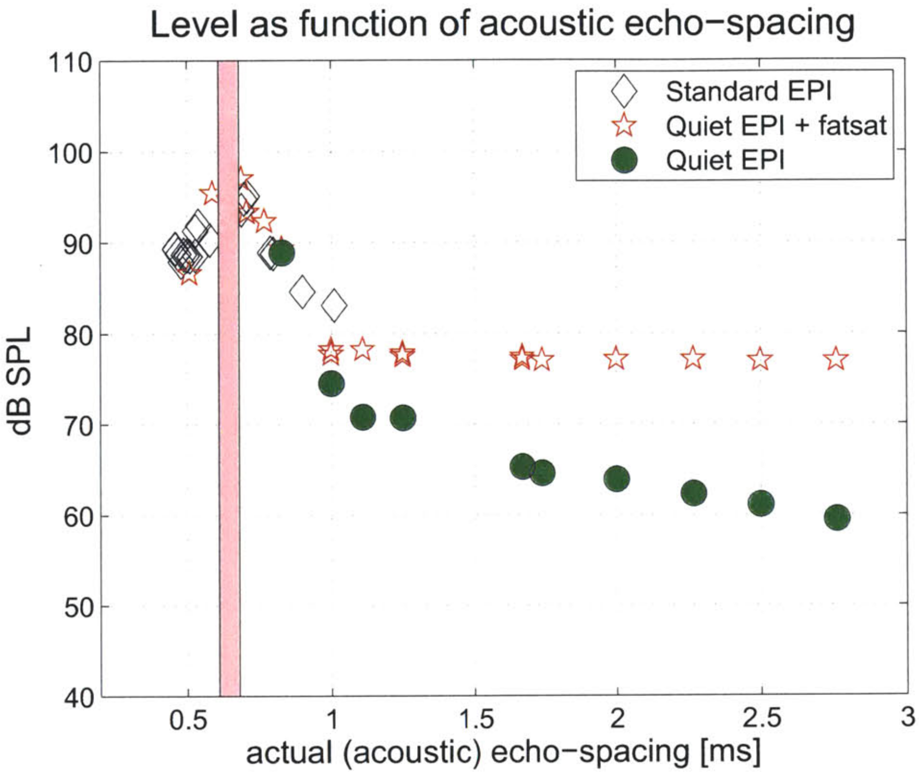

Figure 3-3: Plot of the acoustic noise level measurements taken with the standard MGH EPI sequence (black diamonds), the quiet EPI sequence (red pentagrams) and the quiet EPI sequence without the fat suppression pulses (green circles). The acoustic echo-spacing is the half-period of the fundamental frequency of the readout waveform. If acceleration is used, the effective echo-spacing will be the acoustic echo-spacing divided by the acceleration factor R. The pink band between 0.6 and 0.7 ms echo-spacing denotes a forbidden range of echo-spacings due to an acoustic resonance mode of the gradient coil in that range. Also note the increase in noise level towards the band from both sides.

The results from the acoustic measurements can be seen in figure 3-3. It can be seen that for both conventional EPI and the quiet EPI sequence implemented here, the sound levels are about the same for acoustic echo-spacings below 1 ms. For longer echo-spacings the standard sequence reaches an asymptote of above 80 dB SPL. The quiet sequence reaches a level just above 70 dB SPL. The relatively high level of the asymptote of the quiet sequence was found to be due to the relatively loud gradient spoilers associated with the fat-suppression block. When the fat suppression was removed, the noise level lowered to near 60 dB SPL at acoustic echo-spacings above 2 ms. A good target for this work seemed to be the levels of about 65 dB SPL measured at acoustic echo-spacings just below 2 ms. The distortion requirements of fMRI would thus require an acceleration factor of $R = 4$ to bring this sequence to an effective echo-spacing below 0.5 ms. If a higher noise level is acceptable, depending on application, one should naturally choose a shorter acoustic echo-spacing and therefore improve image quality since less acceleration is required.

3.3.2 Images obtained with GRAPPA/Fourier transform

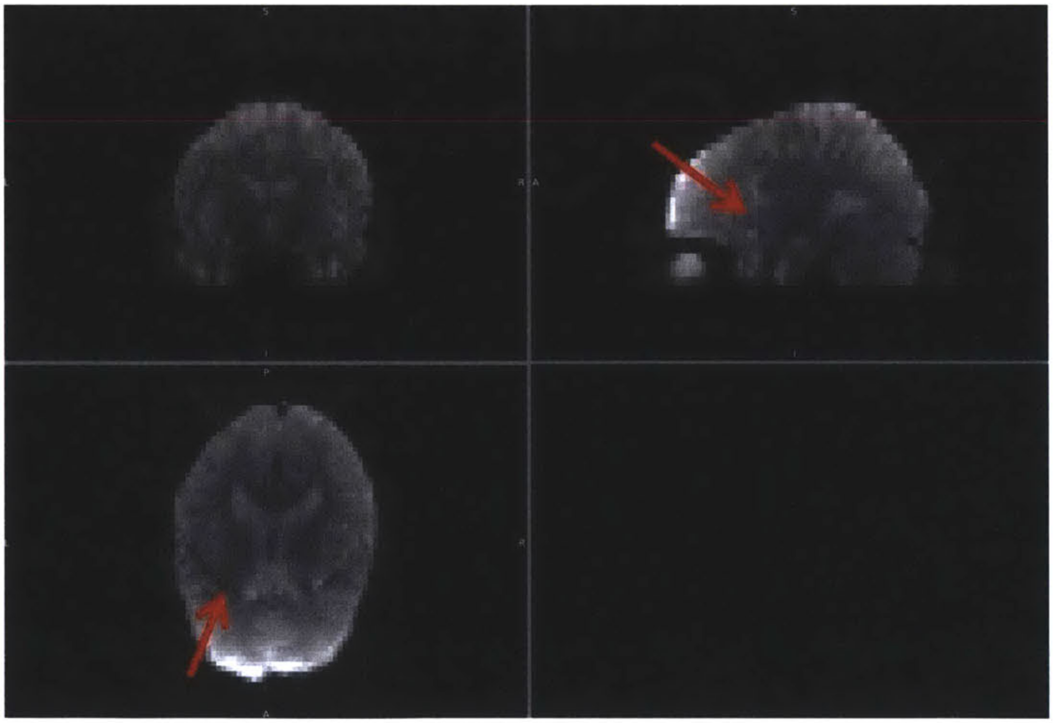

Figure 3-4: Images acquired with an acceleration factor of R=2 and reconstructed with GRAPPA and Fourier transform. The Fourier reconstruction causes aliasing artifacts due to the zig-zag trajectory.

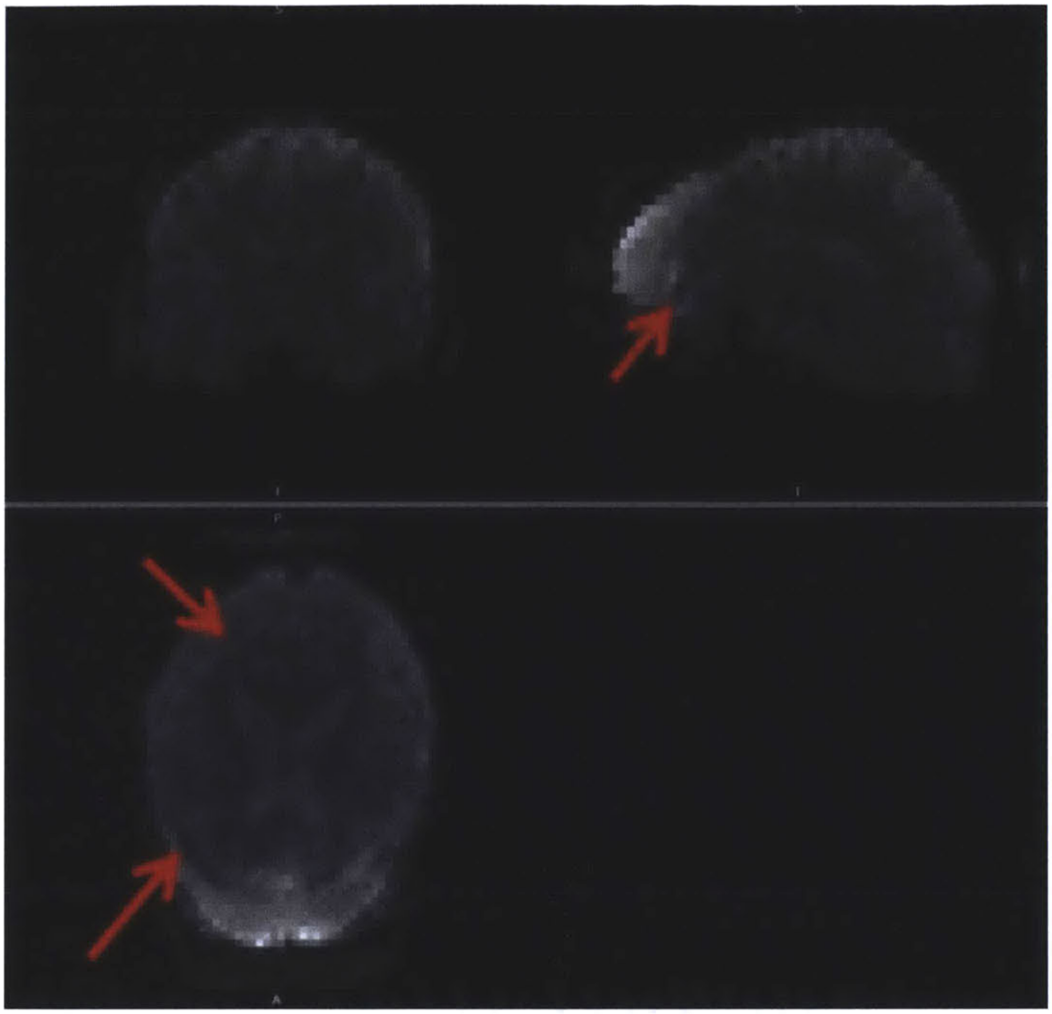

Figure 3-5: Images acquired with an acceleration factor of R=4 and reconstructed with GRAPPA and Fourier transform. This simplified reconstructed causes blurring noticable in the images, as well as aliasing type artifacts in denoted by the red arrows in the images.

Images reconstructed with Fourier transform only can be seen in figures 3-4 and 3-5. Because the Fourier transform neglects the zig-zag nature of the trajectory, aliasing artifacts can be observed in both images. At high-acceleration, the non-uniform coverage of k-space, also causes blurring in the images, since the Fourier transform does not account for this either.

3.4 Discussion

The work in this chapter validates the noise performance of a sequence that clearly leads to very quiet EPI with acceptable image quality. There is room for improvement in several parts of this work. Firstly, the image reconstruction needs to be converted to an approach that is suitable to non-cartesian non-uniformly sampled and intersecting trajectories. My attempts of solving this problem with more "conventional" approaches, which essentially attempt to bring the data into a format such that an FFT can be used to reconstruct them have clearly shown the limitations of such approaches. In general MRI reconstruction has always attempted to make data processible by FFT in order to make the computational costs of the image reconstruction practical. Today, however, the computational cost of DFT, NUFFT[5] and iterative approaches for "small" problems such as the 64×64 images matrices used here, has become acceptable. Especially since the bulk of computation would have to be performed only once per time series, unless dynamic corrections are to be included in the reconstruction. In addition GPU computation techniques can make the computation of problems of this scale almost negligible. I'm convinced that an implementation of such a more general image reconstruction technique will yield good quality images.

There is also room for improvement in the acoustic aspects of this sequence. For example making use of knowledge of the minima in the scanners frequency response function. A detailed measurement of the acoustic gradient transfer function can reveal such minima and allow the selection of much higher readout frequencies than the one I have conservatively picked now. Furthermore the waveforms implemented employ a very high slew rate during the zero-crossing of the sinusoid. Thus, the beginning or end of a sinusoidal waveform could still produce substantial amount of broadband acoustic noise. Additional shaping of the sinusoidal gradient waveforms at each end of the readout to slowly start without a sharp ramp up could further reduce the acoustic noise.

Lastly, as part of this work, the fat suppression had to be removed to make the sequence very quiet. While the fat intensity is not variable in time, and should therefore not harm fMRI analysis, there are reasons for including fat suppression. For one, the chemical shift artifact associated with the fat might cover voxels with fMRI activity in an unfavourable way, and also make coregistration to anatomical images as well as motion correction more difficult. Since fat suppression requires gradient spoiling to work properly, and a quiet gradient spoiling will take up a lot of time, my suggestion is to use water excitation[17, 14] in this pulse sequence. In water excitation, the excitation pulse of the sequence is not only spatially (slice) selective, but also spectrally selective to water. The most commonly used RF pulses for this purpose are so called binomial pulses, in which the combination of 3 or more sequentially pulses have a spectro-spatial response such that they are selecting the desired slice in space, excite mostly spins at the water frequency and have a Null at the CH2 frequency, which is the most common group in lipids. It is also possible to design spectro-spatial pulses on arbitrary gradient waveforms using variable rate pulse design[18, 12], which will make it possible to obtain a good slice profile using a sinusoidally shaped slice-select gradient. Such an implementation would solve both the quiet slice-selection problem as well as the fat suppression problem without using up too much time, such that the performance of the quiet EPI sequence would be compromised.

Bibliography

[1] F. Baumgart, B. Gaschler-Markefski, M. G. Woldorff, H. J. Heinze, and H. Scheich. A movement-sensitive area in auditory cortex. *Nature*, 400:724–726, Aug 1999.

[2] Ronald N. Bracewell. *Fourier Transform and its Applications.* McGraw-Hill, New York, 1978.

[3] J. A. de Zwart, P. van Gelderen, P. Kellman, and J. H. Duyn. Reduction of gradient acoustic noise in MRI using SENSE-EPI. *Neuroimage*, 16:1151–1155, Aug 2002.

[4] W. B. Edmister, T. M. Talavage, P. J. Ledden, and R. M. Weisskoff. Improved auditory cortex imaging using clustered volume acquisitions. *Hum Brain Mapp*, 7:89–97, 1999.

[5] J. A. Fessler. On NUFFT-based gridding for non-Cartesian MRI. *J. Magn. Reson.*, 188:191–195, Oct 2007.

[6] M. A. Griswold, P. M. Jakob, R. M. Heidemann, M. Nittka, V. Jellus, J. Wang, B. Kiefer, and A. Haase. Generalized autocalibrating partially parallel acquisitions (GRAPPA). *Magn Reson Med*, 47:1202–1210, Jun 2002.

[7] D. A. Hall, M. P. Haggard, M. A. Akeroyd, A. R. Palmer, A. Q. Summerfield, M. R. Elliott, E. M. Gurney, and R. W. Bowtell. "Sparse" temporal sampling in auditory fMRI. *Hum Brain Mapp*, 7:213–223, 1999.

[8] S. Haller, A. J. Bartsch, E. W. Radue, M. Klarhofer, E. Seifritz, and K. Scheffler. Effect of fMRI acoustic noise on non-auditory working memory task: comparison between continuous and pulsed sound emitting EPI. *MAGMA*, 18:263–271, Nov 2005.

[9] S. Haller, G. A. Homola, K. Scheffler, C. F. Beckmann, and A. J. Bartsch. Background MR gradient noise and non-auditory BOLD activations: a data-driven perspective. *Brain Res.*, 1282:74–83, Jul 2009.

[10] T. Hamaguchi, T. Miyati, N. Ohno, M. Hirano, N. Hayashi, T. Gabata, O. Matsui, T. Matsushita, T. Yamamoto, Y. Fujiwara, H. Kimura, H. Takeda, and Y. Takehara. Acoustic noise transfer function in clinical MRI a multicenter analysis. *Acad Radiol*, 18:101–106, Jan 2011.

[11] P. M. Jakob, G. Schlaug, M. Griswold, K. O. Lovblad, R. Thomas, J. R. Ives, J. K. Matheson, and R. R. Edelman. Functional burst imaging. *Magn Reson Med*, 40:614–621, Oct 1998.

[12] G. R. Lee, J. A. Tkach, and M. A. Griswold. Time-efficient slab-selective water excitation for 3D MRI. *Magn Reson Med*, Jun 2011.

[13] G. Li and C. K. Mechefske. Structural-acoustic modal analysis of cylindrical shells: application to MRI scanner systems. *MAGMA*, 22:353–364, Dec 2009.

[14] C. H. Meyer, J. M. Pauly, A. Macovski, and D. G. Nishimura. Simultaneous spatial and spectral selective excitation. *Magn Reson Med*, 15:287–304, Aug 1990.

[15] M. E. Ravicz, J. R. Melcher, and N. Y. Kiang. Acoustic noise during functional magnetic resonance imaging. *J. Acoust. Soc. Am.*, 108:1683–1696, Oct 2000.

[16] C. V. Rizzo Sierra, M. J. Versluis, J. M. Hoogduin, and H. D. Duifhuis. Acoustic FMRI noise: linear time-invariant system model. *IEEE Trans Biomed Eng*, 55:2115–2123, Sep 2008.

[17] F. Schick. Simultaneous highly selective MR water and fat imaging using a simple new type of spectral-spatial excitation. *Magn Reson Med*, 40:194–202, Aug 1998.

[18] S. Schmitter and M. Bock. Acoustic noise-optimized VERSE pulses. *Magn Reson Med*, 64:1446–1452, Nov 2010.

[19] S. Schmitter, E. Diesch, M. Amann, A. Kroll, M. Moayer, and L. R. Schad. Silent echo-planar imaging for auditory FMRI. *MAGMA*, 21:317–325, Sep 2008.

[20] K. Sekihara and H. Kohno. New reconstruction technique for echo-planar imaging to allow combined use of odd and even numbered echoes. *Magn Reson Med*, 5:485–491, Nov 1987.

[21] D. Tomasi, E. C. Caparelli, L. Chang, and T. Ernst. fMRI-acoustic noise alters brain activation during working memory tasks. *Neuroimage*, 27:377–386, Aug 2005.

Chapter 4

Stimulus Induced Rotary Saturation

4.1 Introduction

Magnetoencephalography measures magnetic fields near the scalp and infers a distribution of dipole current sources within the cortex. The rationale is that postsynaptic currents occurring synchronously in a population of tens of thousands of cortical pyramidal cells can be modeled as a single current dipole. Because the cells are aligned almost perfectly parallel to each other, the dipolar fields of all the neurons add constructively. Unfortunately it is difficult to learn the microscopic distribution or even amplitude of the currents based on the detected MEG field pattern since MEG measures fields at the scalp (far from the dipole) where the structure of the dipole is not easily discernable. For example, it can be difficult to distinguish between a single larger dipole or a group of parallel small dipoles [10]. Also, there could be cancellation among local dipoles in the folded cortex [10]. Nevertheless, an estimate of the equivalent dipole current strengths can be made within the assumption of the MEG reconstruction and typical numbers range from 5 to 120 nAm with many robust stimulus paradigms giving dipole sources in the tens of nAm range [11]. The temporal characteristics of the MEG-detected dipoles show a range of responses, most typically temporally asymmetric bipolar and multi-phasic responses with significant spectral power at frequencies below 100 Hz [22]. In addition to the transient evoked response, oscillatory fields can be evoked, for example using auditory click-trains [18]. Thus in this case, a narrow-band peak at the stimulus repetition frequency is clearly visible in the MEG-detected fields. Similar narrow-band fields have been detected by MEG during visual paradigms with alternating checkerboard stimuli [31].

The direct detection of neuronal activity using MR imaging techniques has been pursued for over a decade [2, 5, 6, 14, 15, 25, 30, 27, 35] and the progress has recently been reviewed [2]. Most of the proposed techniques are based on the detection of phase shifts or dephasing caused by the extremely small changes in the local B_0 field induced by local neuronal currents. The phase shift or dephasing of the detected MR magnetization accumulates during the TE period of either a gradient echo or spin echo sequence. The phase shift experienced by a given spin within the voxel, $\gamma \mathrm{B}_{\mathrm{neural}}\mathrm{TE}$, can be either positive or negative depending on the sign of the z-component of the field produced by the local current. The total dephasing measured in the image is proportional to the integral of this phase shift over the voxel volume and its temporal integral over the sensitive period of the sequence. The phantom findings are generally encouraging, with detectable local magnetic fields as small as 0.2 nT [5] and current dipoles as small as 6.3 nAm [14], but the in vivo literature contains some positive findings [8, 35], but mostly negative findings [9], including a failure to reproduce the the paradigm of Xiong et al [25].

Understanding the microscopic spatial distribution and time course of the neuronal currents is critical to assessing the potential ability of these MR-based methods to detect neuronal activation. The phase sensitive portion of the MR sequence must be properly timed relative to the transient or oscillating neuronal current to insure that cancellation of the induced phase during a biphasic or multi-phasic current is minimized. For example, the phase sensitive portion of the sequence (the TE period of a gradient recalled echo sequence) might be limited to a single lobe of a biphasic response. Or, for a spin echo sequence, the timing of the 180° pulse can be chosen to occur at the transition between the two phases of the response allowing the biphasic signal to be detected without cancellation [30]. Finally, the conventional methods using T_2 and T_2^* are only sensitive to the component of the local field along the applied external B_0 field.

The spatial distribution of the current within the voxel can also lead to cancellation of the phase shift induced in the MR signal. Even a DC current in a small, straight wire running through the center of the voxel will not induce a net phase shift in the MR signal in that voxel; the current must be offset from the voxel center to produce a net phase accrual [2]. This arises since the phase is sensitive to the sign of the magnetic field and thus the integral of the phase shift over the voxel is zero for this symmetric case. In other cases, the magnetic field is expected to cancel for points within the voxel. For example, for a uniform distribution of discrete parallel wires there are some areas where the magnetic field itself cancels, but the integral of the phase shift over the region cancels everywhere but at the edge of the distribution [24]. In this case the signal will experience magnitude dephasing but not a net phase shift. In a recent simulation study, Park et.al. [24] numerically calculated the effects of neuronal magnetic fields on voxel magnitude and phase, simulating both dendritic as well as axonal currents. They estimate average neuronal fields of 0.3 nT for simultaneous dendritic currents.

Recently, the use of ultra-low-field MRI has been proposed to detect neuronal currents [16, 17]. An extremely low B_0 measurement field allows resonant interactions between the neuronal currents and spin magnetization if γB_0 is brought into the frequency range of the neuronal currents. Although their first measurements were at significantly higher fields, Kraus and colleagues proposed static measurement fields weaker than 0.025 Gauss using a SQUID magnetometer to detect the MR signals at a Larmor frequency of less than 100 Hz [19, 33]. In this scenario, the transient neuronal fields can possibly act as resonant excitation pulse providing the initial excitation of the proton magnetization. Thus, the neuronal current supplies the local B_1 field for excitation and no transverse magnetization should be detected in locations without neuronal currents. Contrary to the high-field MRI-based phase shift approaches mentioned above, multi-phasic or oscillatory currents are beneficial for increasing the tip angle and thus the detected response – provided they have significant spectral power at the Larmor frequency. However, like the high-field phase shift methods, the technique is still susceptible to cancellation effects from the spatial symmetry of the currents within a voxel. Also, the method is sensitive only to the component of the neuronal field perpendicular to the z-axis and the effect is still dependent on the sign of the neuronal current. Thus, a small, straight wire running through the center of the voxel along the static magnetizing field direction produces an excitation giving transverse magnetization along opposite directions in the $x-y$ plane on opposite sides of the wire. Thus, no net signal from the voxel is expected for this situation. The low-field method is also adversely affected by the small Boltzman population and other technical confounds of the low-frequency MRI apparatus.

In this work, we introduce a new approach to effectively lower the Larmor frequency below 100 Hz in high-field MR systems based on the spin-locking mechanism [1]. During a spin-lock, the magnetization is locked in the rotating frame by an RF field, the so-called spin-lock field $\mathrm{B}_{\mathrm{1lock}}$. The effective resonance frequency in the rotating frame during the spin-lock condition is very close to $\omega_{\mathrm{1lock}} = \gamma \mathrm{B}_{\mathrm{1lock}}$, deviating only by a potential Bloch-Siegert shift [4]. This latter small shift in resonance frequency results from the counter-rotating field component of a linearly polarized time-varying field. The Larmor frequency in the rotating frame can be chosen by setting the RF power of the spin-lock pulse. In this work, we acquire phantom data with $\gamma \mathrm{B}_{\mathrm{1lock}}$ ranging from 20 Hz to 200 Hz. $\mathrm{T}_{1\rho}$ relaxation occurs in the spin-lock state from external magnetic field fluctuations with a z-component at the resonant frequency $\gamma \mathrm{B}_{\mathrm{1lock}}$ and harmonics.

Redfield described the saturation of the spin-locked magnetization with an external coil and audio frequency source as "rotary saturation" [29]. Redfield analyzed rotary saturation in solids using $\mathrm{B}_{\mathrm{1lock}}$ fields large compared to the local fields. He derived a steady state magnetization change in the detected spin locked magnetization M_ρ compared to its initial value M_0 for the solid state which is given by:

$$\frac{\mathrm{M}_0 - \mathrm{M}_\rho}{\mathrm{M}_0} = \gamma^2 {\mathrm{B}_{\mathrm{rotarysat}}}^2 \pi \mathrm{T}_{1\rho} f(\omega_{\mathrm{1lock}}), \tag{4.1}$$

where $B_{\text{rotarysat}}$ is the applied rotary saturation field (a function hopefully carried out by the oscillating neuronal fields), $T_{1\rho}$ is the spin-lattice relaxation in the spin-locked state and $f(\omega_{\text{1lock}})$ is the Lorentzian shape function which has a value of 1s on resonance, when $\gamma B_{\text{1lock}} = \gamma B_{\text{rotarysat}}$ [1].

Since Eq. 4.1 was derived for solids and describes a steady state effect. In order to model the effect in liquids and for transitory applications of a rotary saturation field, we model the rotary saturation effect as a coherent rotation away from the B_{1lock} direction by the rotary saturation field (neuronal field). The equations of motion for the magnetization in the spin-lock state are formulated in the doubly rotating frame as:

$$\frac{dM}{dt} = \gamma M \times \left[H_{\text{eff}} \left(1 - \frac{\omega_{\text{rotarysat}}}{\gamma |H_{\text{eff}}|} \right) + B_{\text{rotarysat}} \right] - R(M - M_{\rho}), \tag{4.2}$$

$$R = \begin{pmatrix} \frac{1}{T_2^*} & 0 & 0 \\ 0 & \frac{1}{T_2^*} & 0 \\ 0 & 0 & \frac{1}{T_{1\rho}} \end{pmatrix} \tag{4.3}$$

where H_{eff} is the effective field formed from the applied B_{1lock} and the off-resonance pseudo-field $\Delta\omega/\gamma$, M_{ρ} denotes the equilibrium magnetization in the rotating frame, which is very small since B_{1lock} is small. Here H_{eff} is the relevant axis toward which the magnetization is at equilibrium, is not the static magnetic field direction. If both the spin-lock RF and the rotary saturation field $B_{\text{rotarysat}}$ is on resonance, then H_{eff} is B_{1lock}. $B_{\text{rotarysat}}$ is the audio-frequency field applied orthogonal to the spin-lock axis (here B_{1lock} is taken to be along the x-axis in the singly rotating frame), To preserve the analogy to the singly rotating from, the axes of the doubly rotating frame are renamed so that the z-axis is the equilibrium direction. Thus in the doubly rotating frame, the z-axis is the direction of B_{1lock}. Then $B_{\text{rotarysat}}$ must be applied orthogonal to B_{1lock} to produce a rotation. The magnetization relaxes along H_{eff} with the time constant $T_{1\rho}$, and in the other two directions with the time constant T_2^*. We propose to utilize spin-locking to sensitize the spins to neuronal magnetic fields oscillating at the Larmor frequency in the rotating frame, where γB_{1lock} ranges between 20 and 500 Hz, as set by the applied B_{1lock}. Oscillating neuronal currents with spectral power at γB_{1lock} are then capable of producing rotary saturation of the spin-locked magnetization. Thus, the neuronal currents produce a resonant saturation effect on the MR signal in the rotating frame during the spin-lock state, and the spin-lock state can be tuned to be sensitive to a frequency of interest by adjusting γB_{1lock} . In practice, we anticipate choosing γB_{1lock} to the expected frequency of the neuronal oscillations to sensitize the sequence to these frequencies. Thus the neuronal currents induced by the stimulus create the rotary saturation effect. In analogy with the classic rotary saturation experiment of Redfield [29], we refer to this potential method as Stimulus-Induced Rotary Saturation (SIRS).

To validate the potential of SIRS to detect local current dipoles associated with neuronal activation, we performed two different experiments. The first is the measurement of rotary saturation spectra to characterize the rotary saturation effect from a current dipole. Secondly, we performed a block-design experiment in order to establish detection limits of the method compared to conventional phase-sensitive methods.

4.2 Methods

The measurements were performed in a 17-cm diameter spherical phantom filled with a solution of saline (0.9 % NaCl) and 0.25 ml of Gadopentetate dimeglumine (Magnevist, Berlex Laboratories) yielding a T_1 measured by inversion recovery of 485 ms. The current dipole had a length of 1 cm was formed from 0.89 mm diameter insulated copper wire exposed only at the tips. The current dipole (nAm) produced by this phantom is therefore the product of the current and the dipole length. A photograph of the dipole and a schematic of the driving circuit is shown in Fig. 4-1. The return path for the current was therefore an ionic current distributed within the saline. The dipole was placed 3.9 cm from the edge (4.6 cm from center) of the phantom and the phantom was aligned so that the current dipole was perpendicular to the B_0 field. The dipole was on the end of an insulated rigid copper coaxial cable that extended approximately 2 cm out of the phantom. Thus, with the exception of the two 0.5 cm portions of the dipole, the current was confined to a semi-rigid coaxial cable. Outside of the phantom, the coax was wound into a four-turn solenoid and tuned with a parallel capacitor to form a trap circuit resonant at the Larmor frequency (123 MHz) to reject RF common-mode currents that might be induced by the RF onto the dipole supply leads.

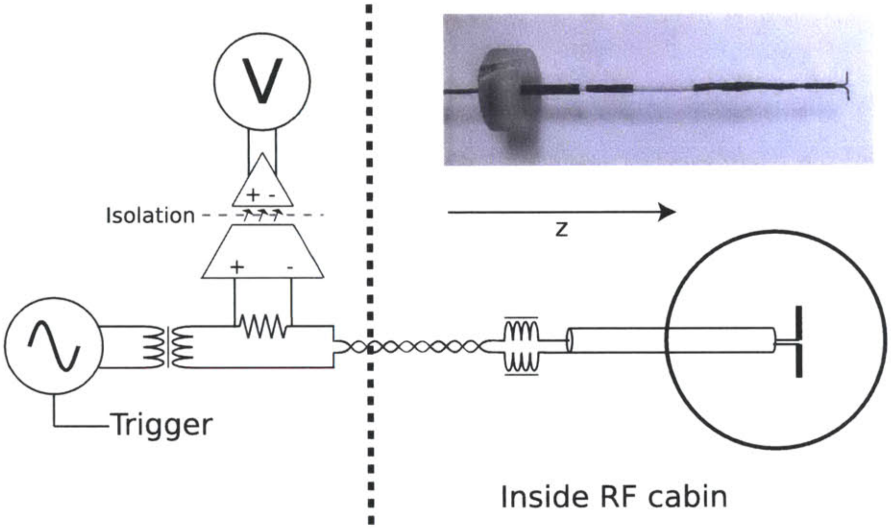

Figure 4-1: Circuit diagram of the apparatus for applying oscillating currents to the dipole phantom during the spin-locking. The function generator is gated by a logic pulse generated by the pulse sequence so that its output is non-zero only during TSL. The output of the function generator then goes through an isolation transformer to eliminate DC and common-mode currents and drives the dipole phantom through a series resistor (10 kΩ) and series RF chokes to block RF pickup on the lines. The current in the phantom is measured by monitoring the voltage drop across the 10 kΩ series resistor using an optically isolated operational amplifier with a gain of 10 and 500 kΩ input impedance. The RMS amplitude of the output of the operational amplifier is measured with a digital oscilloscope.

The magnetic field strengths generated by the current dipole were calculated from the current dipole moment using the equations published by Heller et.al. [12]. The exact dipole location in the sphere was determined based on a high-resolution, 3D turbo spin echo image of the phantom. The calculation was performed for a 2 cm × 2 cm region of interest centered at the current dipole. Since the equations of Heller et.al [12] assume an infinitely small dipole, we modeled our extended dipole by superposition of 1000 dipoles distributed with $10\,\mu$m spacing along the extent of our dipole. The dipole is connected to a digital frequency synthesizer (Global Specialties model 2003) via an audio transformer to eliminate DC offsets and a twisted pair cable with 1μH series RF chokes to prevent the conduction of signals at RF frequencies. The frequency synthesizer uses a gating pulse controlled by the MR pulse sequence in order to supply current only during the spin-lock portion of the sequence. The current through the phantom was determined by measuring the voltage across a $10\,\mathrm{k}\Omega$ series resistor using an optically isolated differential probe with approximately $500\,\mathrm{k}\Omega$ input impedance.

A 3 T whole-body MR scanner (Siemens Medical Solutions, Erlangen, Germany) was used with a transmit and receive birdcage head coil. The spin-lock prepared EPI pulse sequence [7] used is shown in Fig. 4-2. It consists of a $90\,^\circ$ hard pulse in y-direction, immediately followed by a rectangular spin-lock pulse in x-direction, which remains on for the duration TSL. The spin-lock period is followed by a hard $90\,^\circ$ pulse in $-y$-direction which returns the spin-locked magnetization to the longitudinal axis for detection by the standard gradient echo EPI sequence. All remaining transverse magnetization is spoiled by immediately following spoiler gradients. The entire spin-lock preparation is non-selective. Following the preparation a single-slice EPI sequence is used to acquire the $\mathrm{T}_{1\rho}$ weighted image (64x64 matrix, 20-cm FOV, 3.1x3.1 mm, 4-mm thickness with a TE of 19 ms, TR of 1 s, and a readout bandwith of 2298 $^{\mathrm{Hz}}/_{\mathrm{px}}$). For the studies addressing the sensitivity of the technique to dipolar fields, the spin-lock duration, TSL, was 100 ms. In order to determine the $\mathrm{T}_{1\rho}$ of the phantom, TSL was set to 0, 15, 30, 50, and 70 ms, and the resulting image intensity was fit to the relation $\mathrm{I} = \mathrm{M}_0 \exp(-\mathrm{TSL}/\mathrm{T}_{1\rho})$.

4.2.1 Bloch Equation simulation

The simulation starts with the magnetization aligned along the spin-lock field. During the spin-lock phase the audio-frequency saturation field acts to rotate the magnetization away from the spin-lock field. The Bloch simulator tracks all three components of the magnetization in Eq. 4.3, however only the component along the spin-lock

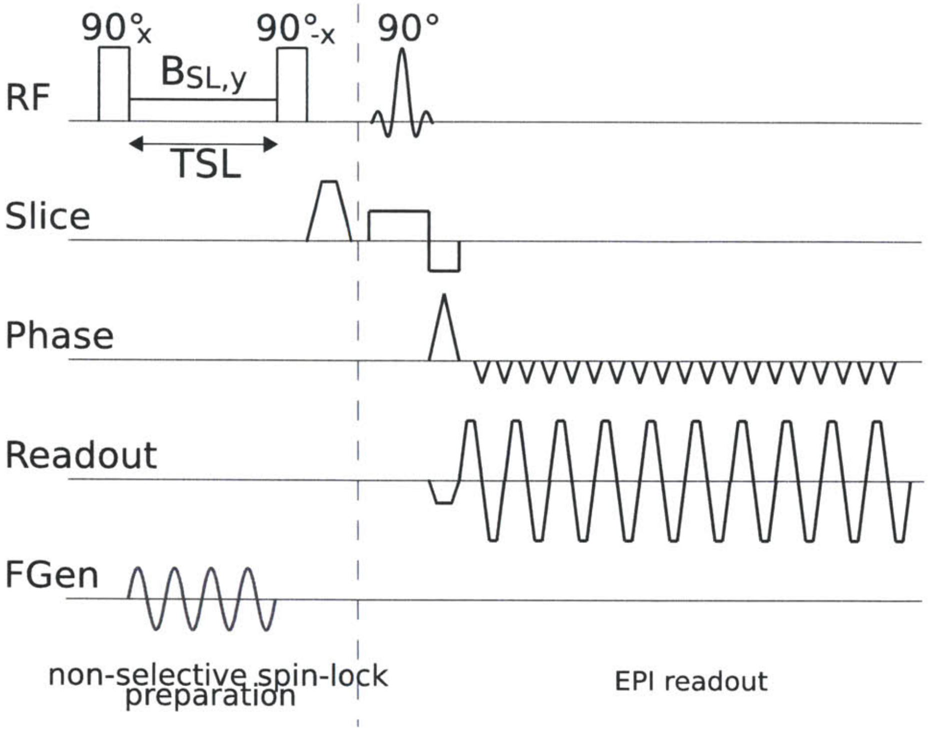

Figure 4-2: Pulse sequence diagram for the spin-lock prepared EPI sequence. After an initial 90 ° excitation, the magnetization is spin-locked along the y-axis by a continuous wave RF pulse applied for a time TSL. Immediately following the spin-lock period, TSL, the magnetization is rotated back to the z-axis by the 90°_{-x} pulse. The the traditional EPI sequence images the magnetization which experienced the spin-lock state. $T_{1\rho}$ relaxation processes during TSL are therefore expected to diminish the signal intensity in the EPI image. The sinusoidal current input to the phantom is applied during the spin-lock period and is shown schematically in the bottom trace.

field is of interest since this component will be returned to the z-axis for subsequent imaging. The other components of the magnetization are dephased by the spoiler gradients following the 90 ° pulse. We simulated the Bloch equations in the doubly rotating frame using an MATLAB code solver with parameters matching the phantom (T_1=1.1s, T_2=0.95 s, $T_{1\rho}$=0.98 s, T_2^*=50 ms) and human brain gray matter at 1.5 T (T_1=0.9 s, T_2=80 ms, $T_{1\rho}$=147 ms, T_2^*=50 ms). Here $T_{1\rho}$ was taken from the $R_2 = 1/T_2$ and $R_1 = 1/T_1$ values using the equation [1]:

$$T_{1\rho} = \frac{2}{(R_2 + R_1)}. \tag{4.4}$$

The rotary saturation spectra simulate the case where a $B_{\text{rotarysat}}$ field of 1 nT and

5 nT is swept in frequency past the γB_{1lock} resonance value. Spectra were obtained for $\gamma B_{1lock} = 10$, 20 and 40 Hz for both the phantom and human relaxation parameters with a spin-lock duration of 100 ms.

4.2.2 Rotary saturation spectra

In order to measure the rotary saturation spectra, the frequency of the synthesizer was swept from below resonance to above the expected rotary saturation resonance, in 1 Hz steps. Each frequency was repeated for 20 images. In order to exclude potential systematic errors, the frequencies were alternately swept up from 20 Hz to 60 Hz or down from 60 Hz to 20 Hz. The spectra taken with γB_{1lock} set to 10 Hz and 20 Hz were swept from 2 Hz to 60 Hz. The entire rotary saturation spectrum measurement was repeated for each B_{1lock} amplitude in order to experimentally confirm the resonance frequency in the rotating frame. Due to capacitive effects in the phantom, the impedance of the phantom, and therefore the current amplitude depends on the frequency of the applied current. The currents reported for the rotary saturation spectra refer to the current measured when the synthesizer was set to the resonance frequency γB_{1lock} . Since the other measurements were performed at a fixed frequency this effect was a limited disruption. For a 50 Hz driving source, the impedance of the phantom was measured to be 950 Ω.

4.2.3 Block design experiment

In the block detection experiment the gating of the function generator was activated to produce the oscillating current for "on" blocks and deactivated for "off" blocks. Thus, a driving current was present only during the spin-locking period of the "on" blocks. The function generator was set to the resonance frequency previously determined with a rotary saturation spectrum measurement. Although γB_{1lock} was set to be 40 Hz based on the scanners transmit adjustment procedure, the minimum was detected at 37 Hz. All block-design measurements were thus performed with the function generator set to 37 Hz. The on-resonance and off-resonance blocks lasted for 20 TR periods of 1s each and were repeated 10 times during each run. Total run time was 6 min, 40 s for the blocks plus 20 dummy scans to insure that the magnetization was in steady state. For high current levels two runs were collected, for the low current levels six runs were collected and analyzed together. Statistical significance was established using a two-sided t-test between the "on" and "off" blocks for each voxel in the image. Block detection experiments were performed at function generator voltage settings of 4 V, 0.4 V and 0.2 V, yielding a measured current (from the voltage drop across the series 10 kΩ resistor) of $118\,\mu A$, $11.5\,\mu A$, and $5.6\,\mu A$, respectively, corresponding to current dipoles of 1180 nAm, 115 nAm, and 56 nAm respectively.

4.3 Results

Spin-lock Images Figure 4-3 shows representative spin-lock images for both the phantom with $\gamma \mathrm{B}_{1\mathrm{lock}} = 40\,\mathrm{Hz}$ as well as a human image obtained with $\gamma \mathrm{B}_{1\mathrm{lock}} = 40\,\mathrm{Hz}$ and 10 Hz.

4.3.1 Magnetic field calculation

Figure 4-4 shows the magnitude of the z-component of the magnetic field associated with a 56 nAm current dipole shown in an axial plane centered on the dipole. Figure 4-4 also shows a plot of magnetic field of the dipole along with a reference plot derived from the Biot-Savart law for a thin, long straight wire. The field is calculated to be 1 nT at a distance of 1.5 mm from the dipole. At this distance the 1 cm extended dipole looks approximately like an infinite wire.

4.3.2 Bloch simulation

Figure 4-5 shows the simulation results for the phantom and the human gray matter relaxation parameters. Rotary saturation spectra are shown for $\gamma \mathrm{B}_{1\mathrm{lock}}$ of 10, 20 and 40 Hz and applied audio-field strengths of 1 nT and 5 nT. In each case, as the frequency of the simulated $\mathrm{B}_{\mathrm{rotarysat}}$ field is swept past the resonance condition

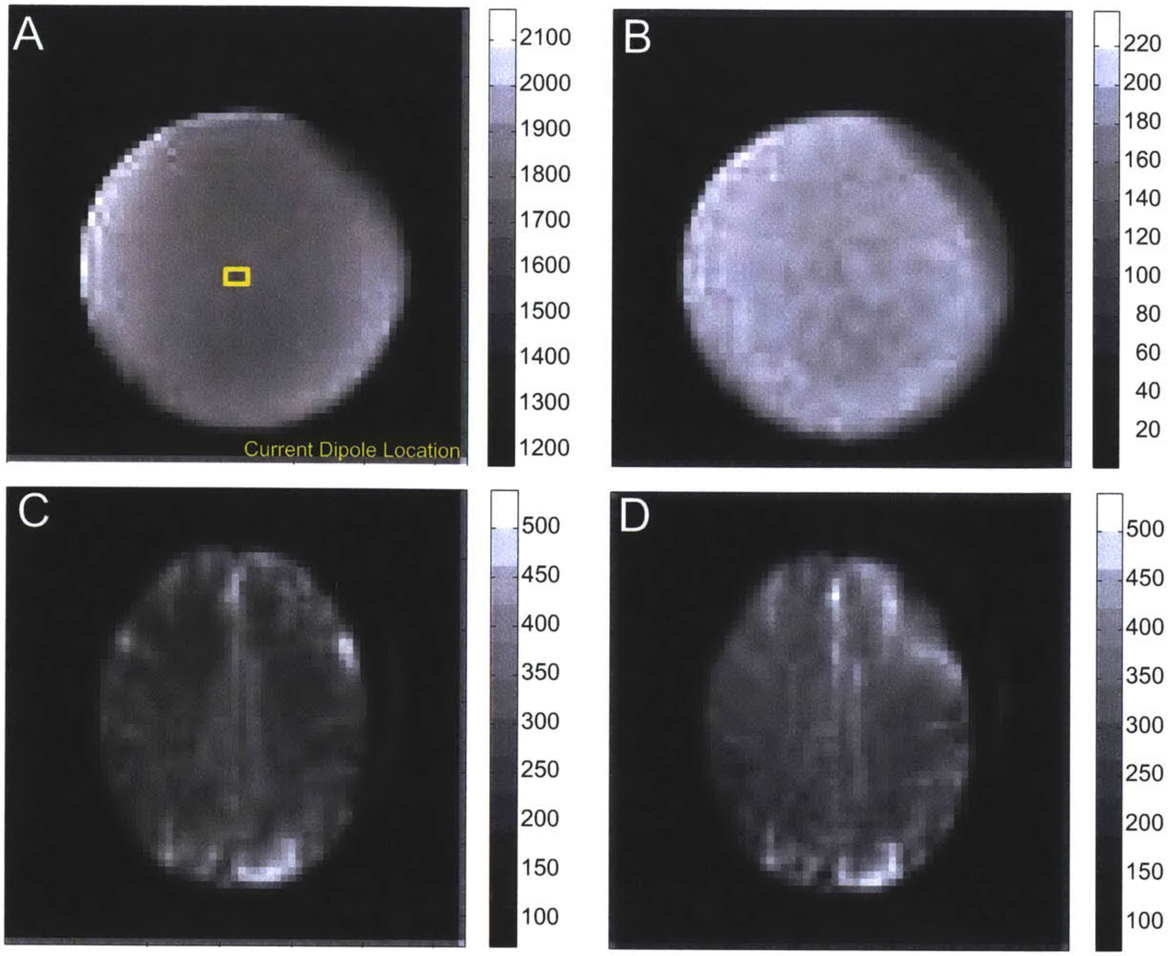
A
2100
2000
1900
1800
1700
1600
1500
1400
1300
1200
Current Dipole Location
B
220
200
180
160
140
120
100
80
60
40
20
C
500
450
400
350
300
250
200
150
100
D
500
450
400
350
300
250
200
150
100

Figure 4-3: Representative spin-lock prepared images from the sequence of Fig. (A) phantom image spin-locked with $\gamma \mathrm{B}_{\mathrm{1lock}}$ =40 Hz shown with the location of the current dipole overlaid in yellow. (B) Time-series standard deviation of a time-series of 420 of the spin-lock prepared images. (C) Brain image obtained with the spin-lock prepared sequence with $\gamma \mathrm{B}_{\mathrm{1lock}}$ =40 Hz and (D) $\gamma \mathrm{B}_{\mathrm{1lock}}$ =10 Hz.

at $\gamma \mathrm{B}_{\mathrm{1lock}}$, a reduction of signal is observed which peaks when $\mathrm{B}_{\mathrm{rotarysat}} = \gamma \mathrm{B}_{\mathrm{1lock}}$. The linewidth and degree of saturation in the Bloch simulations was found to be independent of $\gamma \mathrm{B}_{\mathrm{1lock}}$. The effect is roughly linear with $\mathrm{B}_{\mathrm{rotarysat}}$ for small $B_{\mathrm{rotarysat}}$. For a neuronal oscillations at 10, 20 and 40 Hz, a $B_{\mathrm{rotarysat}}$ field of 6.8 nT reduced the magnetization by 0.1 % for the 100 ms spin-lock duration experiment using gray matter relaxation parameters at 1.5 T. The neuronal field causing a 0.1 % magnetization change decreased to 4.0 nT and 2.2 nT for spin-lock durations of 200 ms and 500 ms respectively.

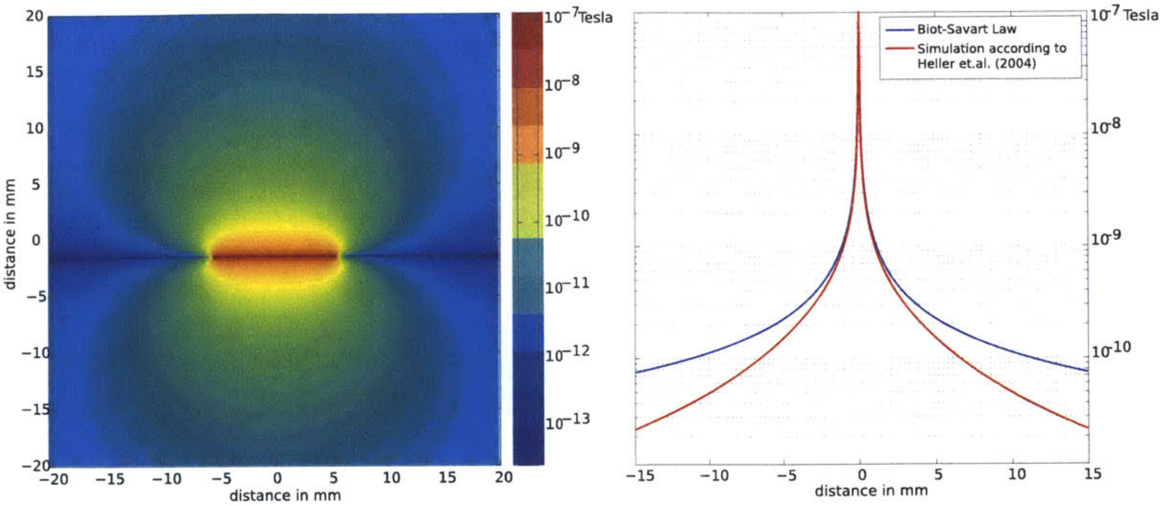

Figure 4-4: Magnitude if the z-component if the magnetic field associated with the current dipole phantom. Left, axial image of the z-component of the field for a $5.6\,\mu A$ current in the dipole (56 nAm dipole moment) based on the distributed dipole model. A field of 1 nT is estimated for a distance of 1.5 mm from the wire. Right, plot along the y-axis showing both the field values derived from the distributed dipole model and the Biot-Savart law for a long thin wire.

4.3.3 Rotary saturation spectra

The phantom data (Fig. 4-6) show a decrease in image amplitude when the applied current in the phantom oscillates at close to the Larmor frequency in the rotating frame, $\gamma B_{1\text{lock}}$. The observed linewidth of the saturation spectra is about 6 Hz FWHM. The peak often appeared at a slightly (2 Hz) higher frequency than expected from the $B_{1\text{lock}}$ level determined from the instruments standard transmit calibration, possibly due to the Bloch-Siegert shift [4] or a mis-calibrated B_1 level. For high dipole current strengths ($400\,\mu A$), the rotary saturation effect achieved a 30 % amplitude decrease. For a small dipole current ($16\,\mu A$), the shape of the rotary saturation spectrum can still be observed in voxels immediately neighboring the dipole. The amplitude minimum still occurs close to the selected Larmor frequency in the rotating frame as expected. The observed linewidth of the rotary saturation spectra is also about 6 Hz.

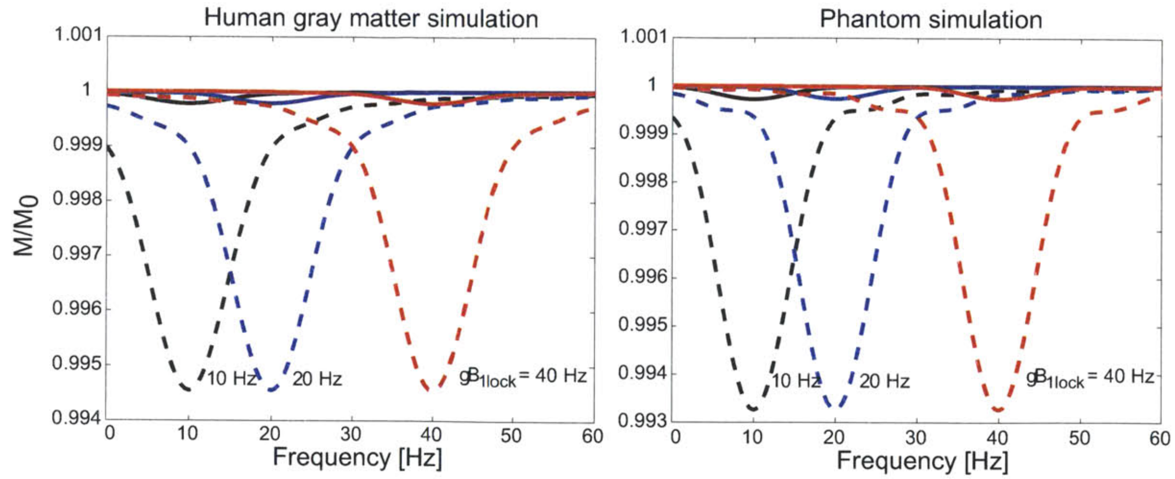

Figure 4-5: Simulation of the rotary saturation effect based on the Bloch equations in the rotating frame. The simulations show the fraction of the spin-locked magnetization as a function of the frequency applied $B_{\mathrm{rotarysat}}$ field. When the frequency of $B_{\mathrm{rotarysat}}$ reaches the resonance condition in the rotating frame (equal to $\gamma B_{1\mathrm{lock}}$) the spin-locked magnetization is rotated away from the spin-lock field $B_{1\mathrm{lock}}$. In the spin-lock prepared experiment, only the spin-locked magnetization is returned to the longtudinal axis for subsequent imaging. Simulations were performed for human gray matter at 1.5 T ($T_1 = 1100\,\mathrm{ms}$, $T_2 = 950\,\mathrm{ms}$, $T_2^* = 100\,\mathrm{ms}$). The effect is shown for rotary saturation at $\omega_{\mathrm{rotarysat}}$ of 10 Hz,20 Hz and 40 Hz (black, blue and red curves respectively) using $B_{\mathrm{rotarysat}}$ of 1 nT (solid line) and 5 nT (dashed line).

4.3.4 Block detection experiment

The t-test maps from the block design runs at each of the three current levels are shown in Fig. 4-7. The t-test results are overlaid on a high-resolution Turbo-spinecho image, but an example of an individual spin-lock prepared echo-planar image is shown in Fig. 4-3a. The two runs performed with 4 V function generator setting ($118\,\mu A$ current through the dipole) resulted in a large number of significant ($p < 0.001$) voxels above and below the dipole, in approximate agreement with the expected distribution of the z-component of the dipolar field. The six runs performed with 0.4 V function generator setting ($11.5\,\mu A$ in the dipole) showed significant voxels only within 5 mm above and below the dipole. The lowest current experiment performed with a 0.2 V function generator setting ($5.6\,\mu A$ in the dipole) yielded three significant voxels, all immediately below the dipole. The percentage signal change observed was 0.15 % for the $5.6\,\mu A$ current in the dipole.

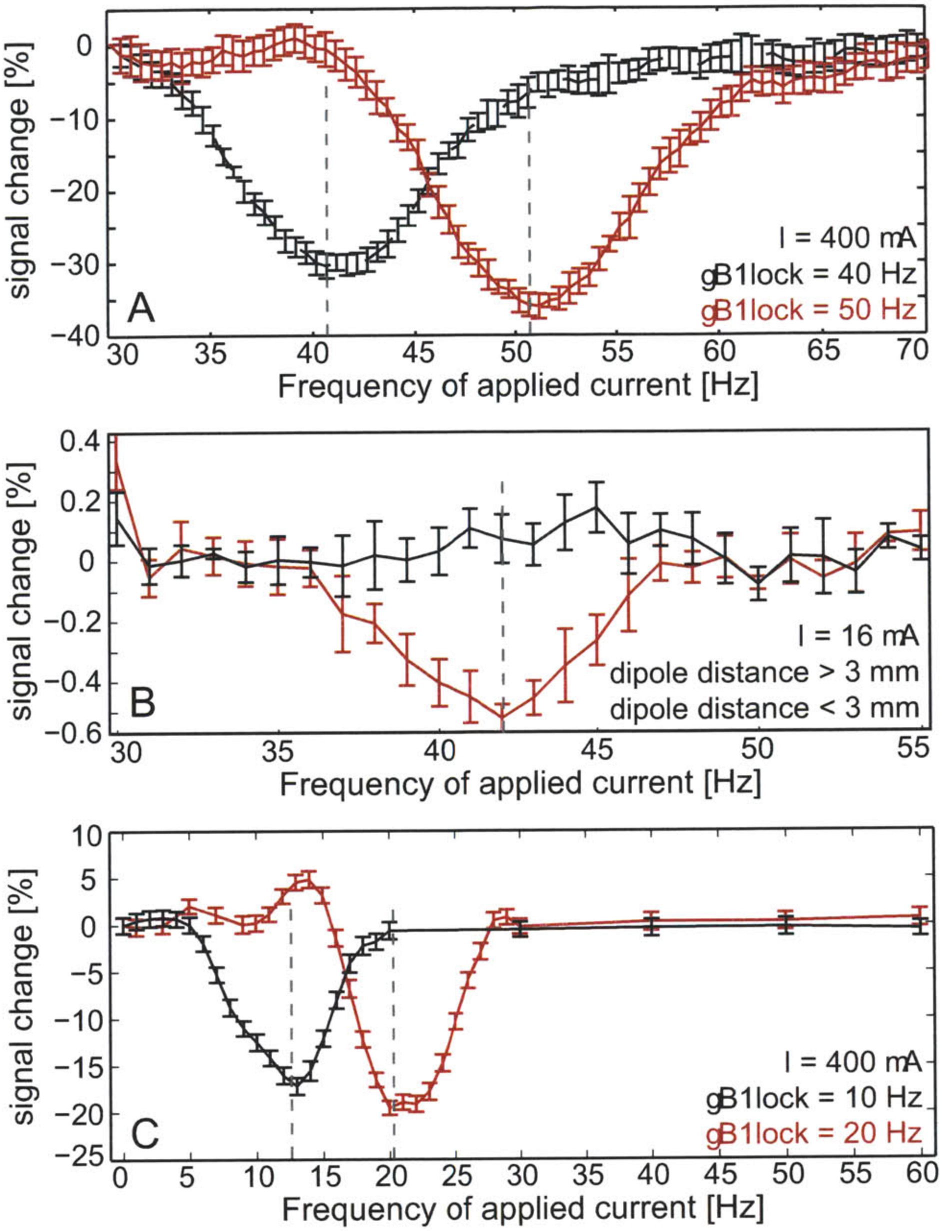

Figure 4-6: Simulation of the rotary saturation effect based on the Bloch equations in the rotating frame. The simulations show the fraction of the spin-locked magnetization as a function of the frequency applied $\mathrm{B}_{\mathrm{rotarysat}}$ field. When the frequency of $\mathrm{B}_{\mathrm{rotarysat}}$ reaches the resonance condition in the rotating frame (equal to $\gamma \mathrm{B}_{1\mathrm{lock}}$) the spin-locked magnetization is rotated away from the spin-lock field $\mathrm{B}_{1\mathrm{lock}}$. In the spin-lock prepared experiment, only the spin-locked magnetization is returned to the longtudinal axis for subsequent imaging. Simulations were performed for human gray matter at 1.5 T ($\mathrm{T}_1 = 1100\,\mathrm{ms}$, $\mathrm{T}_2 = 950\,\mathrm{ms}$, $\mathrm{T}_2^* = 100\,\mathrm{ms}$). The effect is shown for rotary saturation at $\omega_{\mathrm{rotarysat}}$ of 10 Hz,20 Hz and 40 Hz (black, blue and red curves respectively) using $\mathrm{B}_{\mathrm{rotarysat}}$ of 1 nT (solid line) and 5 nT (dashed line).

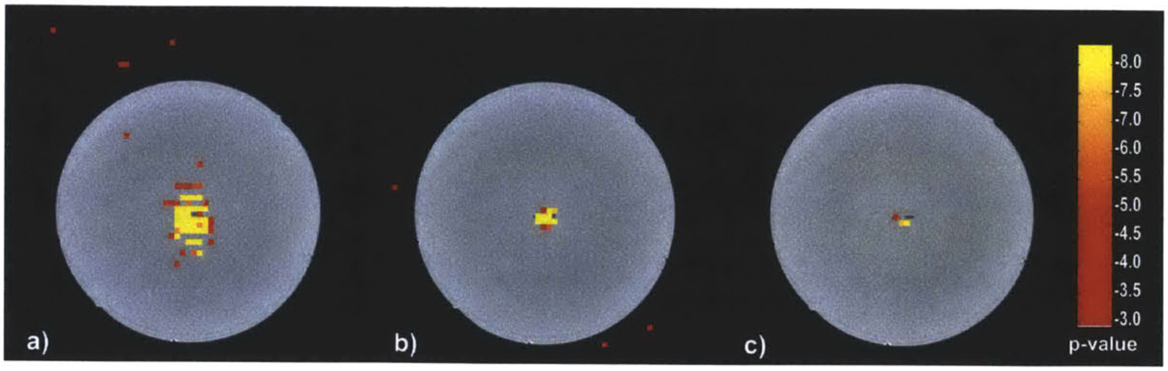

Figure 4-7: Two-sided t-test results (not Bonferroni corrected) from the block-design paradigm shown with a lower threshold of $p < 10^{-3}$ and a color scale saturation level of $p < 10^{-8}$. All block designs were 20 s per period, and $\gamma \mathrm{B}_{1\mathrm{lock}} = 40\,\mathrm{Hz}$. T-test results are overlaid on a high-resolution Turbo Spin Echo (TSE,RARE) image which allows visualization of the current dipole's wires. A) $118\,\mu A$ applied current, B) $11.5\,\mu A$ applied current C) $5.6\,\mu A$ applied current.

4.4 Discussion

The validation of this methodology is based on the equivalent current dipole model which is commonly utilized in MEG data analysis. The rationale is that postsynaptic currents occurring synchronously in a population of tens of thousands of cortical pyramidal cells can be modeled as a single current dipole because the cells themselves are almost perfectly parallel to each other and thus the dipolar fields of all the neurons add constructively. From the far field it is impossible to distinguish between a single larger dipole or a group of parallel small dipoles. Thus, this phantom study is an appropriate benchmark for the MEG experiment. Here our phantom tries to match the magnetic fields observed in MEG using a single artificial dipole. For the MR experiment, however, the dipolar fields are detected locally by their effect on the MR signal, in our case due to their rotary saturation effect on neighboring water. In this case, the relevant magnetic fields are not the far-fields of the dipole, as in MEG, but the local fields among the neurons. Nonetheless, a single current dipole provides an easy-to-construct approximation which at least matches the neural situation very closely in the far field but likely only to an order of magnitude in the local fields of activated cortex. While we show that the rotary saturation method appears to have adequate sensitivity to local magnetic fields using a current dipole phantom, T_2^*-based phase and amplitude methods are also adequate by these measures. For example, Konn et al are able to see a minimum dipole moment of 6.3 nAm (current of $1.3\,\mu A$ and dipole size of 5 mm) using the phase shift in EPI in a phantom similar to ours using 62 minutes of averaging [14]. Normalizing for averaging time, this corresponds to a dipole moment of 77 nAm ($10\,\mu A$ current) in a minute of scan time. Pell et al [26] used the magnitude changes and observed a minimum current of $1.7\,\mu A$ in a 1.8 min run; a normalized sensitivity of $2.3\,\mu A$ in a minute of scan time. The block design results shown in Fig. 4-7 show a non-Bonferoni corrected p-value of 10^{-7} for a 56 nAm dipole ($5.6\,\mu A$ current) in 40 minutes of imaging time. However, unlike the phase and magnitude EPI experiments, the signal change in the SIRS experiment does not scale linearly with current. The method detects the reduction in magnetization as the spin-locked magnetization is rotated away from the spin-lock axis, thus scales as $1-\cos(\phi) \approx \phi^2/2$ where ϕ is the small tip angle induced by the rotary saturation field in the doubly rotating frame. Since ϕ is proportional to $B_{\mathrm{rotarysat}}$, and thus the current, the effect is expected to scale with the square of the current. Thus, for the SIRS experiment an 1 minute experiment would be expected to detect a 2.5 fold smaller current than the 40 min experiment. This suggests the ability to detect a 22.4 nAm dipole or $2.2\,\mu A$ current in the normalized 1 minute of imaging time. While larger than that of the other two studies, or result occurred with a Bonferroni corrected p-value of approximately 2×10^{-5} compared to the threshold for statistical significance of $p = 10^{-3}$ used in the Pell result. The failure of the T_2^*-weighted imaging to detect actual neuronal currents in human experiments suggest that the single current dipole phantom does not adequately mimic the local phenomena near the neurons. Our best insight into whether or not the SIRS method (or other MR methods) is sufficiently sensitive to allow detection of neuronal fields comes from microSQUID measurements of evoked fields near the cortex. Okada and colleagues has measured the magnetic fields 1.2 mm above the cortex of juvenile swine [23]. They measure fields in excess of 1 pT in response to snout stimulation. While the current dipole model used provides a diffuse current return path similar to that expected in vivo, practical implementation of the phantom causes problems which make it difficult to use for DC current measurements. When a DC current is used, electrolysis at the electrode tips occurs causing gas bubbles and alteration of the current. Eventually the tips must be sanded. Although platinum exhibits reduced electrolysis, unlike copper it is severely diamagnetically different from water and altered the EPI images. Thus, we did not perform a direct comparison to the DC current measurements in the literature using T_2^* weighted EPI phase and amplitude measures and rely on the extensive literature for the sensitivity of these methods. A major difference between the macroscopic phantom's local fields and that within the microscopic distribution of neurons is likely caused by the spatial cancellation effects in both field and MR phase arising from the multiple parallel neuronal currents in neighborhood of activated cortex. We break this down into two effects. First is the cancellation of the neuronal magnetic fields at some spatial locations within the distribution of synchronous neurons. For water at spatial locations where this cancellation occurs, it is unlikely that any MR method will be able to detect a signal change. For example, a region with uniformly spaced, current-carrying discrete wires with aligned currents, the magnetic field cancels at spatial locations half way between the wires and is reduced near these locations. The second concern is based on how the surviving fields affect the MR signal. The signal changes are determined by integrating the local effects over both time and space. Spatially, the magnitude and phase changes in a T_2^*-weighted experiment are determined by integrating over the voxel. In this case, the effect can be reduced by the symmetry of the voxel with respect to the current distribution. For example, a single current-carrying wire centered on the voxel will not produce a net phase shift, and will exhibit a reduced magnitude reduction. Park and colleagues estimate the signal and magnitude changes for a region of activated cortex larger than a voxel. In this case, the voxels near the edge of the activated region have the strongest effect. Considering time-domain effects is important for neuronal currents which reverse polarity during the measurement period. In the case of a symmetric multi-phasic current time course, there can be complete elimination of the accrued phase shift in the MR signal. MEG experiments suggest that at least partial cancellation will occur for many stimuli. This effect can be reduced by carefully timing the MR pulse sequence relative to the evoked response so that the phase sensitive part of the MR experiment only occurs during one phase of the response, or exactly straddles the refocusing pulse of a spin echo experiment [30]. An additional source of cancelation of the neuronal magnetic fields can derive from a lack of phase coherence among the neuronal currents. This leads to incomplete superposition among the individual neurons fields. This is a problem common to all neuronal magnetic field measurements including MEG since the distal nature of the MEG detectors is unlikely to help a lack of phase superposition. Although phase cancellation among the local fields undoubtably occurs, a 1 nT estimate for the strength of local neuronal fields within millimeters of the activation is supported MicroSQUID measurements close to the cortex indicate the presence of neuronal magnetic fields above 1 nT at a distance of 1 mm above active cortex [23, 13]. The rotary saturation approach presented here cannot offer improved detection in areas where the fields from the local neuronal currents cancel, but likely has advantageous spatial and temporal averaging properties relative to MR phase measurements and T_2^*-weighted imaging. The saturation method does not suffer from intra-voxel cancellation due to the phase of the saturation field; local water molecules will be saturated by the neuronal fields regardless of the phase of these fields, and the averaged effect over the voxel or time-period of the spin locking will always further reduce the signal intensity. A further limitation that is common to both our approach and the T_2^*-based methods is that the neuronal magnetic field needs to be parallel to B_0 in order to have an effect. When investigating the cerebral cortex and assuming large pyramidal neurons to be the main generator of the neuronal magnetic field, only certain regions of the cortex satisfy this condition for a given head position, thus, in an in vivo experiment the target area needs to be carefully selected and the subjects head appropriately positioned. A similar "orientation blindness" occurs in MEG which is insensitive to radial dipoles. For the Rotary Saturation experiment, the neuronal fields must be oriented orthogonal to the spin-lock field. If needed the experiment could be repeated with the spin-lock along the other axis to eliminate the orientation blindspot. Furthermore, there are additional limitations to an in vivo rotary saturation experiment. The spin-locking period is limited in time by both SAR restrictions and the $T_{1\rho}$ time. The method, as implemented, was limited to single-slice measurements, although multi-slice spin-locking sequences have been developed for other purposes [34]. In a motional narrowed regime, such as the bulk water that is usually imaged in MRI, the $T_{1\rho}$ time is almost identical to T_2 when the spin-lock is performed on resonance [20]. Practically this limits the spin-lock duration to about 100 ms. Furthermore, the selected Larmor frequency in the rotating frame has an upper limit due to the SAR restrictions and a lower limit imposed by the ability to create a spin-lock. However, our initial tests with in vivo imaging have found that Larmor frequencies in the rotating frame as low as 10 Hz are feasible (see Fig. 4-3). Additionally, the method is currently sensitive to only a single frequency of neuronal currents but could, in principle, be extended to at least several frequencies. We designed our phantom experiment to demonstrate the SIRS effect in the frequency range of evoked responses commonly observed in MEG/EEG measurements of the human brain. Virtually all magnetic fields originating from postsynaptic currents have frequencies of less than 120 Hz, with the bulk of fields being below 20 Hz. Examples for experiments that evoke narrow-band oscillations are auditory click-trains [18], somatosensory stimulation with rapid electrical or mechanical pulse trains [28] and visual stimulation with periodic rapidly changing intensity [21]. It is also possible to evoke or induce so called gamma oscillations (30 Hz-60 Hz) with specific stimuli, which will give rise to narrow-band magnetic fields occurring often from the sensory cortex associated with the modality. Contamination by the BOLD effect is a problem common to all MR neuronal current methods and several studies have attempted to address this [2] For example, eliminating BOLD contamination might be achieved by timing to make the experiment sensitive only to the early response and not the later BOLD signal. This requires a long Inter-Stimulus Interval (ISI) and renders the experiment inefficient. A second approach is to saturate the BOLD effect by attempting to have similar BOLD responses for all conditions. For the SIRS method this might involve altering the stimulus frequency by approximately 10 Hz so that the Rotary saturation effect is on-resonance for one condition and off resonance for the other. This gives full SIRS contrast but little BOLD changes if the two stimuli have similar BOLD response. A third method is to attempt to reduce the BOLD effect by performing the study at low B_0 fields. Unlike BOLD, most neuronal current methods (including SIRS) are expected to have little dependence on B_0. The contrast itself is not altered for SIRS except through secondary effects such as relaxation times changes. Since T_2 and thus $T_{1\rho}$ are expected to lengthen at lower B_0, SIRS contrast should slightly improve with experiments at lower B_0 field. Similarly the reduced Specific Absorption Rate (SAR) constraints will allow longer TSL and more sensitive detection. The time series SNR is expected to have only modest decreases as the B_0 is lowered due to the dominance of physiological noise at high field for conventional voxel volumes [32]. Finally, there is some hope that pharmacologic preparation might help for neuronal current studies in animal models. Here agents are being sought which act only on astrocytes and effect the flow response but not electrophysiology [3].

The sensitivity of the method is limited by $T_{1\rho}$ and the spin-lock duration TSL. $T_{1\rho}$ is influenced by many parameters including the B_0 field, the spin-lock field amplitude ($B_{1\mathrm{lock}}$) the temperature, and the tissue type. Borthakur et al found $T_{1\rho}$ for gray and white matter to be 99 ms and 85 ms respectively at $\gamma B_{1\mathrm{lock}} = 500\,\mathrm{Hz}$ at 1.5 T. The corresponding T_2 values were 75 ms and 66 ms. Thus, the $T_{1\rho}$ in the brain is similar in magnitude to T_2, but not identical.

4.5 Conclusion

We introduce a new method by which neuronal currents might be construed to affect MR signals. We demonstrate that the method has the sensitivity to detect the magnetic fields of dipole current sources of similar magnitude and frequencies to that observed in MEG experiments. The method is an analog to the excitation of MR signal by neuronal fields proposed by Kraus [16] for ultra-low field MRI, but has the advantage of being applicable to standard high-field MR instrumentation. While we have not yet demonstrated its ability to detect neuronal fields in vivo, the method has many favorable spatial and temporal averaging properties which may be holding back conventional MR phase and T_2^* magnitude-based studies.

Bibliography

[1] A. Abragam. *Principles of Nuclear Magnetism*, volume 32 of *International Series of Monographs on Physics.* Oxford University Press, New York, paperback edition, 1983.

[2] P.A. Bandettini, N. Petridou, and J. Bodurka. Direct detection of neuronal activity with mri: fantasy, possibility, or reality? *Applied Magnetic Resonance*, 29:65–88, Mar 2005.

[3] M. H. Baslow, V. V. Dyakin, K. L. Nowak, B. L. Hungund, and D. N. Guilfoyle. 2-PMPA, a NAAG peptidase inhibitor, attenuates magnetic resonance BOLD signals in brain of anesthetized mice: evidence of a link between neuron NAAG release and hyperemia. *J. Mol. Neurosci.*, 26:1–15, 2005.

[4] F. Bloch and A. Siegert. Magnetic resonance for nonrotating fields. *Phys. Rev.*, 57(6):522–527, Mar 1940.

[5] J. Bodurka and P. A. Bandettini. Toward direct mapping of neuronal activity: MRI detection of ultraweak, transient magnetic field changes. *Magn Reson Med*, 47:1052–1058, Jun 2002.

[6] J. Bodurka, A. Jesmanowicz, J. S. Hyde, H. Xu, L. Estkowski, and S. J. Li. Current-induced magnetic resonance phase imaging. *J. Magn. Reson.*, 137:265–271, Mar 1999.

[7] A. Borthakur, J. Hulvershorn, E. Gualtieri, A. J. Wheaton, S. Charagundla, M. A. Elliott, and R. Reddy. A pulse sequence for rapid in vivo spin-locked MRI. *J Magn Reson Imaging*, 23:591–596, Apr 2006.

[8] L. S. Chow, G. G. Cook, E. Whitby, and M. N. Paley. Investigating direct detection of axon firing in the adult human optic nerve using MRI. *Neuroimage*, 30:835–846, Apr 2006.

[9] R. Chu, J. A. de Zwart, P. van Gelderen, M. Fukunaga, P. Kellman, T. Holroyd, and J. H. Duyn. Hunting for neuronal currents: absence of rapid MRI signal changes during visual-evoked response. *Neuroimage*, 23:1059–1067, Nov 2004.

[10] Matti Hämäläinen, Riitta Hari, Risto J. Ilmoniemi, Jukka Knuutila, and Olli V. Lounasmaa. Magnetoencephalography—theory, instrumentation, and applications to noninvasive studies of the working human brain. *Rev. Mod. Phys.*, 65(2):413–497, Apr 1993.

[11] Riitta Hari. On brain's magnetic responses to sensory stimuli. *J. Clin. Neurophysiol.*, 8(2):157–169, Apr 1991.

[12] L. Heller, D. Ranken, and E. Best. The magnetic field inside special conducting geometries due to internal current. *Biomedical Engineering, IEEE Transactions on*, 51(8):1310 –1318, aug. 2004.

[13] H. Ikeda, Y. Wang, and Y. C. Okada. Origins of the somatic N20 and high-frequency oscillations evoked by trigeminal stimulation in the piglets. *Clin Neurophysiol*, 116:827–841, Apr 2005.

[14] D. Konn, P. Gowland, and R. Bowtell. MRI detection of weak magnetic fields due to an extended current dipole in a conducting sphere: a model for direct detection of neuronal currents in the brain. *Magn Reson Med*, 50:40–49, Jul 2003.

[15] D. Konn, S. Leach, P. Gowland, and R. Bowtell. Initial attempts at directly detecting alpha wave activity in the brain using MRI. *Magn Reson Imaging*, 22:1413–1427, Dec 2004.

[16] R. H. Kraus. Low field SQUID MRI. Talk at Workshop on Multi-modal Functional Neuroimaging, Cortona, Italy, Jun 2006.

[17] R. H. Kraus, P. Volegov, A. Matlachov, and M. Espy. Toward direct neural current imaging by resonant mechanisms at ultra-low field. *Neuroimage*, 39:310–317, Jan 2008.

[18] F. H. Lin, T. Witzel, M. S. Hämäläinen, A. M. Dale, J. W. Belliveau, and S. M. Stufflebeam. Spectral spatiotemporal imaging of cortical oscillations and interactions in the human brain. *NeuroImage*, 23:582–595, Oct 2004.

[19] A. N. Matlachov, P. L. Volegov, M. A. Espy, J. S. George, and R. H. Kraus. SQUID detected NMR in microtesla magnetic fields. *J. Magn. Reson.*, 170:1–7, Sep 2004.

[20] P. R. Moran and C. A. Hamilton. Near-resonance spin-lock contrast. *Magn Reson Imaging*, 13:837–846, 1995.

[21] M. M. Müller, W. Teder, and S. A. Hillyard. Magnetoencephalographic recording of steady-state visual evoked cortical activity. *Brain Topogr*, 9:163–168, 1997.

[22] E. Niedermeyer and F.H. Lopes da Silva. *Electroencephalography: Basic Principles, Clinical Applications, and Related Fields.* Williams & Wilkins, Baltimore, 4th edition, 1999.

[23] Y. Okada, A. Lahteenmaki, and C. Xu. Comparison of MEG and EEG on the basis of somatic evoked responses elicited by stimulation of the snout in the juvenile swine. *Clin Neurophysiol*, 110:214–229, Feb 1999.

[24] T. S. Park and S. Y. Lee. Effects of neuronal magnetic fields on MRI: numerical analysis with axon and dendrite models. *NeuroImage*, 35:531–538, Apr 2007.

[25] L. M. Parkes, F. P. de Lange, P. Fries, I. Toni, and D. G. Norris. Inability to directly detect magnetic field changes associated with neuronal activity. *Magn Reson Med*, 57:411–416, Feb 2007.

[26] G. S. Pell, D. F. Abbott, S. W. Fleming, J. W. Prichard, and G. D. Jackson. Further steps toward direct magnetic resonance (MR) imaging detection of neural action currents: optimization of MR sensitivity to transient and weak currents in a conductor. *Magn Reson Med*, 55:1038–1046, May 2006.

[27] N. Petridou, D. Plenz, A. C. Silva, M. Loew, J. Bodurka, and P. A. Bandettini. Direct magnetic resonance detection of neuronal electrical activity. *Proc. Natl. Acad. Sci. U.S.A.*, 103:16015–16020, Oct 2006.

[28] T. S. Prevec and K. Ribarić-Jankes. Can somatosensory system generate frequency following response? *Pflugers Arch.*, 431:R301–302, 1996.

[29] Alfred G. Redfield. Nuclear magnetic resonance saturation and rotary saturation in solids. *Phys. Rev.*, 98(6):1787–1809, Jun 1955.

[30] M. Singh. Sensitivity of mr phase shift to detect evoked neuromagnetic fields inside the head. *Nuclear Science, IEEE Transactions on*, 41(1):349 –351, feb 1994.

[31] C. Tallon-Baudry, O. Bertrand, and C. Fischer. Oscillatory synchrony between human extrastriate areas during visual short-term memory maintenance. *J. Neurosci.*, 21:RC177, Oct 2001.

[32] C. Triantafyllou, R. D. Hoge, G. Krueger, C. J. Wiggins, A. Potthast, G. C. Wiggins, and L. L. Wald. Comparison of physiological noise at 1.5 T, 3 T and 7 T and optimization of fMRI acquisition parameters. *Neuroimage*, 26:243–250, May 2005.

[33] P. Volegov, A. N. Matlachov, M. A. Espy, J. S. George, and R. H. Kraus. Simultaneous magnetoencephalography and SQUID detected nuclear MR in microtesla magnetic fields. *Magn Reson Med*, 52:467–470, Sep 2004.

[34] A. J. Wheaton, A. Borthakur, S. R. Charagundla, and R. Reddy. Pulse sequence for multislice T1rho-weighted MRI. *Magn Reson Med*, 51:362–369, Feb 2004.

[35] J. Xiong, P. T. Fox, and J. H. Gao. Directly mapping magnetic field effects of neuronal activity by magnetic resonance imaging. *Hum Brain Mapp*, 20:41–49, Sep 2003.

Chapter 5

Summary

In this thesis we have demonstrated three techniques addressing some of the limitations of conventional fMRI. We have shown, for the first time, a single-shot whole-brain EVI method that can acquire whole-brain volumes at a rate of 8 frames per second with a voxel size of 3.25 mm isotropic. This method can be used to investigate the influence of cardio-respiratory noise on the BOLD signal and to remove the cardio-respiratory components from the BOLD response. We have also shown an acoustically quiet EPI pulse sequence that can acquire images at the same spatial and temporal resolution as previously used acoustically noisy techniques. This method may be used in future to study the function of the human central auditory system as well as improve fMRI studies of sensitive patient populations. Lastly, promising results were shown on an entirely new form of functional image contrast that enables the detection and localization of oscillating magnetic fields via resonant interaction between the water spins and the oscillating fields to be detected. The initial results show room for improvement and approach the sensitivity required to detect neuromagnetic fields *in-vivo*. In combination with the EVI method, the SIRS method may be able to overcome the influence of physiological noise sources that currently hinder the use of SIRS *in-vivo*. While more work remains to be done on all three techniques, progress and feasibility was shown on each of the three solutions proposed in this thesis to the existing limitations of conventional fMRI.